Université Mohamed Boudiaf - M'sila

FACULTE DE TECHNOLOGIE

DEPARTEMENT D'ELECTRONIQUE

Numéro de série : ……

Numéro d'inscription : …….

Thèse

Présentée pour l'obtention du diplôme de

DOCTORAT SCIENCES

Spécialité : Electronique
Option : Electronique

THEME

Contribution à l'étude des propriétés physiques des matériaux chalcostibites et emplectites : Applications Photovoltaïques

---

Contribution to the study of the physical properties of chalcostibites and emplectites materials: Photovoltaic applications

---

Présenté par

KETFI Mohammed Elamin

Soutenue le : 30/06/2022

Devant le jury composé de :

LADJAL Mohamed	Prof	Université de M'sila	Président
BENNACER Hamza	MCA	Université de M'sila	Rapporteur
SAAD ESSAOUD Saber	MCA	Université de M'sila	Co-Rapporteur
DJOUDI Lakhdar	Prof	Université de Tissemsilt	Examinateur
MESKINE Said	MCA	Université de Mostaganem	Examinateur
ABBASSA Hamza	MCA	Université de Mostaganem	Examinateur
BOUKORTT Abdelkader	Prof	Université de Mostaganem	Invité

Année universitaire : 2021/2022

Acknowledgements

First and above all, I praise Allah, the Almighty for providing me this opportunity and granting me the capability to proceed successfully.

I warmly thank Prof. LADJAL Mohamed Professor for agreeing to chair the jury for my thesis defense. Thanks to Mr. DJOUDI Lakhdar Professor at the Academic Center of Tissemsilt, Mr. MESKINE Said and ABBASSA Hamza Professors at the University of Mostaganem for agreeing to judge and examine this work.

I would like to thank my supervisor Dr. BENNACER Hamza for his help, inspiration and motivation during the course of the PhD. I am grateful to my second supervisor Dr. SAAD ESSAOUD Saber, for his kind support and precious advice. His help was always much appreciated, his supportive and enthusiastic attitude allowed me to conduct research in freedom and always comforted me whenever I needed guidance.

It would be unfair to ignore my colleagues in the *ECP3M* laboratory headed by Professor BOUKORTT Abdelkader, whom I would like to thank for accepting my integration into his laboratory, for introducing me to all members of his team, and for my participation in the highly successful workshop that was held in his laboratory and under his supervision. I also extend my thanks; I mean sincere prayers and mercy to the brother and colleague Dr. BENAISSA Youssef, who passed away last year during the pandemic. Without forgetting Dr. ZIANE Mohamed Issam for his help, even from afar.

Dear:

My parents

My wife

My children

My brothers and my sister

& All my family

TABLE OF CONTENTS

List of figures

List of tables

List of Abbreviations

AM0	Air mass at a solar zenith angle of 0 degrees
AM1.5	Air mass at a solar zenith angle of 48.19 degrees
BOA	Born-Oppenheimer approximation
BZ	Brillouin zone
CB	Conduction band
CBM	Conduction band minimum
CIGS	$CuIn1–xGaxSe_2$
CIS	$CuInSe_2$
CGS	$CuGaSe_2$
CTGS	$Cu_2Sn_{1–x}Ge_xS_3$
CTS	Cu_2SnS_3
CTSS	$Cu_2Sn_{1–x}Si_xS_3$
CZTS	Cu_2ZnSnS_4
CZTSe	$Cu_2ZnSnSe_4$
CZTSSe	$Cu_2ZnSn(S_{1–x}Se_x)_4$
DFT	Density functional theory
DOS	Density-of-states
EHPs	Electron-hole pairs
FP-LAPW	Full-potential linearized augmented plane wave
GGA	Generalized gradient approximation
HF	Hartree-Fock
HSE06	Heyd-Scuseria-Ernzerhof exchange-correlation functional with standard values
IBZ	Irreducible Brillouin zone
KS	Kohn-Sham
LDA	Local density approximation
PAW	Projector augmented wave
PBE	A simplified GGA
PES	Potential energy surface
PV	Photovoltaic

Abstract

Due to their useful physical properties, copper-based chalcogenides materials are recently promising for numerous emerging technological fields. In photovoltaics, discovering and designing suitable materials for solar cells is a primary technical challenge. The structural, electrical, optical, and thermoelectric properties for both $CuYSe_2$ and $CuYTe_2$ in the hexagonal phase, as well as $CuYS_2$ in the orthorhombic phase have been investigated using a numerical Full Potential-Linearized Augmented Plane Wave (FP-LAPW) technique based on Density Functional Theory (DFT).

To compute the structural properties, both, the local density approximation (LDA) and the generalized gradient approximation (PBE-GGA) were used as exchange-correlation potentials. On the other hand, the modified Becke-Johnson (mBJ) was used to compute the optoelectronic, properties with higher degree of precision. Our calculations revealed that these three compounds have indirect band gaps in the range of 0.6eV to 2.1eV. Moreover, numerous thermoelectric qualities of the investigated compounds estimated as a function of electric potential energy at different temperatures using the semi-local Boltzmann transport theory, whereby the findings exhibit a higher Seebeck coefficient for $CuYS_2$ compared to $CuYZ_2$(Z = Se and Te) up to 2.7mV/K for $CuYS_2$ at 300K, with acceptable values of thermal and electronic conductivity. The quasi-harmonic model is used to examine thermodynamic properties such as heat capacity at constant pressure and volume, entropy, Debye temperature, and thermal expansion coefficient under both pressure and temperature influences. As a result of this study, $CuYS_2$, $CuYSe_2$ and $CuYTe_2$ are promising materials for optoelectronic devices, especially as photovoltaic materials in solar cells. we performed the numerical simulation. We optimize the physical and electrical parameters such as the thicknesses for each layer of the cell in order to see their influences on the electrical characteristic of the $ZnO/CdS/CuSb(S/Se)_2$ structures. The efficiency of the solar cells have been observed by varying the thickness and doping concentrations of TCO layers, buffer layers, and absorber layers. Moreover, the obtained maximum efficiencies are approximately 18.84% and approximately 14.19%, for $CuSbS_2$ and $CuSbSe_2$ based solar cell, respectively.

Keywords: TB-mBJ, Seebeck Coefficient, Electrical and Thermal Conductivity Coefficients, Dielectric function, absorption coefficient, reflectivity, heat capacity, thermal expansion coefficient, wx-AMPS-1D.

General Introduction

With the new global trend towards renewable energies, scientific research in its experimental and theoretical forms has begun to accelerate towards exploiting one of the most important permanent energy resources, which is solar energy, where light energy is converted into electrical energy such as solar panels and photovoltaic systems [1,2].

The basic idea of the invention of solar panels dates back to the noticed the possibility of generating electrical energy by exposing certain materials to light rays. After this discovery, many studies followed, including the discovery of the element selenium, which greatly affected the progress of this technological aspect and its exploitation in several areas such as computers and satellites. The efficiency of these photovoltaic technologies depends on many factors, perhaps the most important of which is the nature of the materials of which they are made.

One of the main barriers to photovoltaics being implemented as a major energy generation technology is its relatively high cost. Thin film inorganic photovoltaics is a proven technology that offers significant reductions in cost compared with crystalline silicon which is the current dominant market PV technology. Of these, copper indium diselenide (CIS) based photovoltaics and in particular, it's variant, copper indium gallium diselenide ($CuInGaSe_2$ or CIGS), has yielded the highest laboratory efficiency of all the thin film technologies. Currently both cadmium telluride (CdTe) and CIGS based photovoltaics are now produced at the gigawatts peak (GWp) scale and their cost reductions and potential for thin film photovoltaics is starting to be achieved [3].

During the period of these developments, the threats of climate change and security of energy supply have become increasingly apparent and require finding alternative sources of energy ever more urgent. As the photovoltaic market develops, the current CdTe and CIGS technologies are making a significant contribution and this is expected to continue. However, the scale of energy supply needs makes it necessary to consider sustainability of any future energy source [4-6].

The application of crystalline silicon photovoltaics is not considered to be limited by the active absorber layer material, because silicon is one of the most abundant materials on Earth. Most studies consider silicon to be limited by the silver used in the contacts. The success of CIGS technologies, together with the concerns about the dependency on materials with low

availability and abundance, has stimulated interest in alternative materials in the same family of inorganic compounds. These include $Cu_2ZnSn(Se, S)_4$ Sn–S based materials, together with Cu–Sb and Cu–Bi based compounds. Of these materials the most promising to date are the $Cu_2ZnSn(S, Se)_4$ (CZTS) kesterite materials that have demonstrated laboratory conversion efficiencies of over 12% [3].

CZTS-based devices utilize materials with significantly lower cost and greater abundance than those based on CIGS. Copper pipes and electrical cables are found in most buildings, while zinc is used on as galvanic protection for steel streetlights, fencing and corrugated iron roofing. Tin is used in tinplate and is produced in volume for cans. Considering the materials that form CZTS in the context of PV and future TWp markets, however, it becomes clear that these materials have great potential for a sustainable stable thin film technology [7]. On the other hand Copper-based chalcogenides materials in chalcopyrite, chalcostibites, emplectites, kesterite, and stannite structures have recently been considered promising materials for a variety of emerging technological fields, including optoelectronic and photovoltaic devices, due to their semiconducting behavior and useful physical properties [8].

Due to the great importance that chalcogenides compounds have acquired, many theoretical and experimental research groups have undertaken research work on chalcogenides compounds of different structures, in order to explore their properties and then choose the most appropriate field for their use. Among the most important theoretical methods that have been widely used in the study of chalcogenides compounds are those that combine quantum theories and computational simulation. Moreover, simulation methods allow for updating concepts and computational relationships as they undergo improvements in an attempt to bring theoretical results as close as possible to experimental results [9].

Ternary compounds chalcogenides are some of the promising materials, which have been explored as potential candidates for the third generation of solar cells. They are a combination of some elements from group I, III, IV and VI. Their general formula is $A_xB_yX_z$ with A = (Cu, Ag, Au); B = (Al, Ga, In); X = (S, Se, Te) and x, y and z ∈ N. They crystallize in different structures and the most common ones are the ABX_2 in tetragonal, orthorhombic, hexagonal and rhombehodral structures [10].

Motivated by their potential applications in the solar cell industry, the goal of this research is to conduct a systematic theoretical and computational study of the structural, optoelectronic, thermodynamic, and thermoelectric properties of ternary compounds based on

Copper as a potential component of solar-energy harvests using first principles methods such as FP-LAPW, with a focus on the CuY(S, Se, and Te)$_2$ families. Then, we will try to invest these properties for the proposal and the design of the thin film solar cell based on these chalcogenides and make a comparison with other cells.

This thesis represents research and analysis done over the past four years. It is organized into three chapters, each with a specific goal. Chapter 1 outlines an introductory for giving information about chalcogenides, basic methodology used in these material synthesis and importance of iterative size reduction technique as a new nanotechnology tool for the fabrication of nano and microstructures. Chapter 2 contains a theoretical study in general for any crystalline system based on the laws and foundations of quantum mechanics, in the study of regular crystal lattices and abbreviated in the time-independent Schrödinger wave equation, which describes a system composed of a large number of electrons and nuclei in motion and interacting with each other, then we highlight the most important approximations that has been adopted to simplify the solution of the Schrödinger equation as the Born-Oppenheimer approximation, the Hartry approximation, the Harty-Fock approximation and the theory of the density function, In addition, we present the two most important approximations for estimating the exchange-bonding interaction between electrons, and then we explain the linearly increasing full potential plane wave method FP-LAPW and finally and the description of the different software used for the properties studied. Chapter 3 goes into more details calculation of the structural properties by LDA and GGA approximations and determined some structural properties of $CuYS_2$, $CuYSe_2$ and $CuYTe_2$ compounds as cell constants, compressibility modulus and cohesive energy. The Density Functional Theory (DFT) will be used as the main tools of the study. In the first stage, we will perform a structural phase stability of different potential phases of $CuYZ_2$. We studied the electronic behavior of the three compounds, where we determined the value of the energy gap for each of them, as well as the electronic orbitals contributing to each energy band by studying the density of state curves, in addition to determining the type of bonds between atoms based on the charge density distribution curves in the interfacial region. As for the optical properties, we studied both the absorption coefficient and the reflection coefficient, the coefficients of inertia and refraction and the energy loss coefficient for each compound, while comparing all the results obtained with what has been obtained in other scientific research. From the thermodynamically and thermoelectrically studies, the most stable phases of the three compounds will be identified, after that we proceed to the proposal and the design of thin film solar cell based on the studied chalcogenides and

make a comparison with other cells. Finally, we summarize the results of our work and give the direction for future works.

References

[1] L. Hong, H. Yao, Z. Wu, Y. Cui, T. Zhang, Y. Xu, R. Yu, Q. Liao, B. Gao, K. Xian, Eco-compatible solvent-processed organic photovoltaic cells with over 16% efficiency, Adv. Mater. 31 (2019) 1903441.

[2] J. Gong, C. Li, M.R. Wasielewski, Advances in solar energy conversion, Chem. Soc. Rev. 48 (2019) 1862–1864.

[3] D. W. LANE, K. J. HUTCHINGS, R. Mc Cracken, New Chalcogenide Materials for Thin Film Solar Cells, The Royal Society of Chemistry (2015) 160-167.

[4] K. Zweibel, in The Terawatt Challenge for Thin-Film PV, National Renewable Energy Laboratory, Golden, CO, 2005, pp. 1–44.

[5] A. Feltrin and A. Freundlich, Renewable Energy, 2008, 33, 180–185.

[6] J. E. Trancik and K. Zweibel, in Proceedings 2006 IEEE 4th World Conference on Photovoltaic Energy Conversion, 2006, pp. 2490–2493.

[7] K. Zweibel, in Thin Film Solar Cells: Fabrication, Characterization and Applications, ed. J. Poortmans and V. Arkhipov, John Wiley & Sons, Chichester, UK, 2006, pp. 427–462.

[8] I. Forbes and L. M. Peter, in Materials for a Sustainable Future, ed. T. M. Letcher and J. Scott, RSC Books, Cambridge, UK, 2012, p. 828.

[9] B. P. Rai, Sol. Cells, 1988, 25, 265–272.

[10] Rachel Woods-Robinson, Yanbing Han, Hanyu Zhang, Tursun Ablekim, Imran Khan, Kristin A. Persson, and Andriy Zakutayev, Wide Band Gap Chalcogenide Semiconductors, Chem. Rev. 2020, 120, 9, 4007–4055.

CHAPTER I

Theoretical background

Summary

We covered in this part the binary chalcogenides MCh (e.g., ZnCh), ternaries (represented by chalcopyrites, such as $CuAlCh_2$, chalcostibites, emplectites, such as $Cu(Sb/Bi)(S/Se)_2$, sulvanites, such as Cu_3TaCh_4, -$BaCu_2S_2$, and related structures), and layered mixed-anion oxychalcogenides (e.g., $Cu3MCh_4$) and we look at photovoltaic and photo-electrochemical solar cells, transistors, and light-emitting diodes as examples of applications where chalcogenides are used as an active or passive layer. This component of the study attempts to stimulate future research on chalcogenides by analyzing, categorizing, and discussing prospective prospects in this emerging class of semiconductors.

Chalcogenides based materials, chalcostibites and emplectites

1. Introduction

Intensive research on photovoltaic cells in the second half of the twentieth century resulted in technology up-scaling and continuous improvement of solar cell performance. Initially used primarily in spatial applications, solar cells and solar panels gradually expanded into other types of applications. Various solar programs funded by public subsidies in Europe, Japan, and the United States during the 1990s and 2000s associated with industrial development led to the widespread adoption of PV and the construction of numerous power plants based on solar panels around the world. The achievement of leveled electricity costs equivalent to or lower than conventional power plants in several recent PV projects represents an important step toward much greater penetration of solar energy in today's energy landscape [1].

Chalcogenide based compounds are a unique class of materials with many practical applications, especially in relation to their optical properties. However, the fundamental understanding of their electronic structure and physical properties is rather scattered and incomplete [2].

The figure (I.1), show a chalcogenide group VI (Ch) that have been studied and divide into many parts: (1) binary II-VI MCh semiconductors (e.g., ZnS, CdS) [3-5] and other binary M_xCh_y semiconductors (e.g., SnS_2, In_2S_3); (2) ternary chalcopyrite I-III-Ch_2 semiconductors (mostly Cu based), represented by $CuAlS_2$, and other ternaries (e.g., α-$BaCu_2S_2$ and Cu_3MCh_4) [6,8]; (3) Multinary layered mixed-anion compounds like LaCuOCh, BaCuSF, and CuSCN [9,10]; and (4) 2D chalcogenides like MoS_2, which include binary and ternary materials.

This figure (I.1) shows a network diagram schematic of various material classes, with chalcogenides highlighted in red. Various facets of this large topic of semiconductors are addressed in numerous review papers and book chapters. Others focus on applications such as transparent electronics, TFTs [10], and photovoltaic, while others look at oxide TCOs in terms of intrinsic material properties [11,12], Others include graphene, nitrides [13], halides [14], and carbides [15], among others [16]. A few publications cover chalcogenide semiconductors briefly, although they only look at oxides or a small group of chalcogenides [17]. As a result, we will concentrate on the chalcogenides in this section, referring to chalcogen anions as Ch (with Ch = S, Se, Te) and excluding O [18].

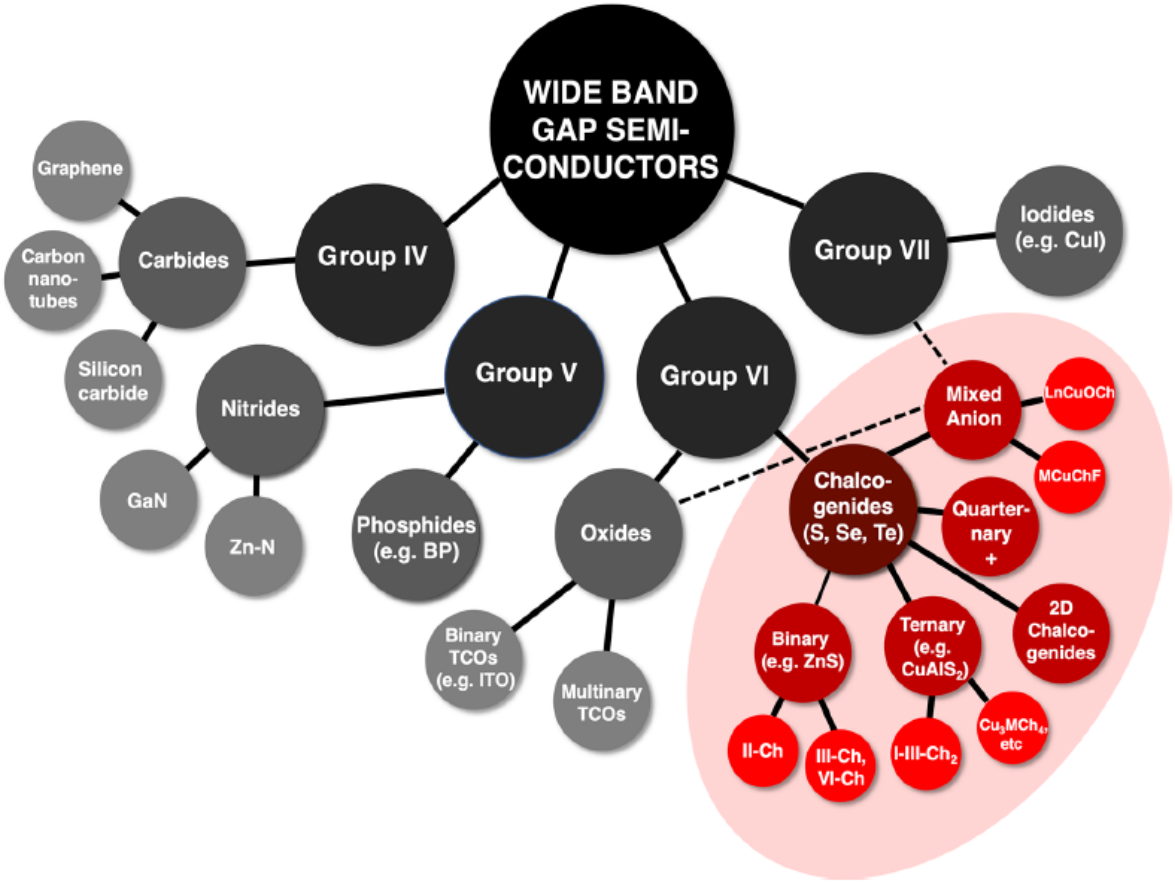

Figure.I.1. Schematic network diagram depicts various material classes of semiconductors. Anion group is used to order the classes [6].

2. Chalcogenides based materials

Chalcogenide is derived from the Greek words "chalcos" which means ore and "gen" which means formation, hence the term chalcogenide is sometimes used to mean or former. Chalcogens are the elements in Group VI of the periodic table. This group includes the elements oxygen, sulfur, selenium, tellurium, and polonium. Despite the fact that oxygen is not a chalcogenide and Po is a radioactive element, it is included in the chalcogenide group. These were first established in the 1950s by N.A.Goryunova and B.T.Kolomits for arsenic sulphide glasses that are optically clear over a broad IR range. Despite the fact that oxide materials are the earliest known glass-forming mechanism, chalcogenide compounds have historically been treated independently. Oxide glasses differ from chalcogenides in that they have a wide band gap, which contributes to significantly distinct optical and electrical properties [19].

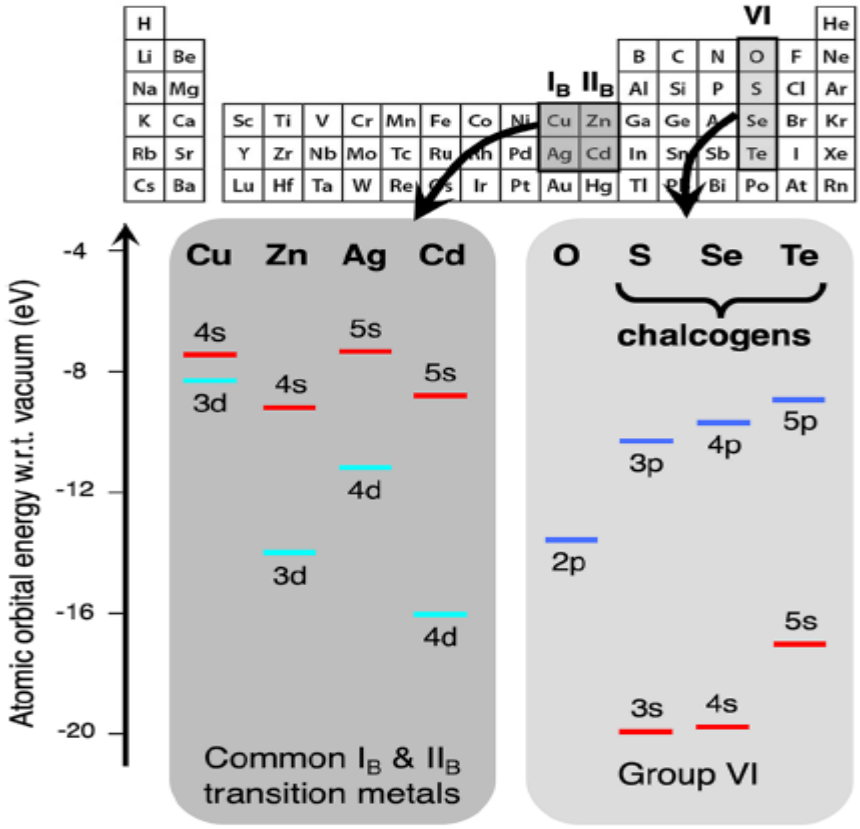

Figure.I.2. Atomic orbital (AO) energies of group VI elements (including chalcogens S, Se, and Te) and typical transition metal elements present as cations in compounds [19].

Some binary chalcogenides, ternary chalcogenides, and oxy-chalcogenides that have been predicted by computational researches are also highlighted. Many of these materials haven't been well investigated for optoelectronic applications; therefore they open up new avenues for further experimentation.

Table.I.1. The classification of amorphous chalcogenide systems [20].

N°	Category	Examples
01	Pure chalcogenide	S,Se, Te
02	Pnictogen-chalcogen	(V-VI) As_2S_3, P_2Se, Se-Te-Sb, Se-Te-Bi
03	Tetragen-chalcogen	(VI-VI) $SiSe_2$, GeS_2, (III-VI) B_2S_3, In_xSe_{1-x}, Se-Te-In
04	Metal-chalcogenide	MoS_3, WS_3, Ag_2S-GeS_2
05	Halogen-chalcogenide	As-Se-In, Ge-S-Br, Te-Cl

2.1 Binary II-Ch Chalcogenides

The simplest family chalcogenide semiconductors are binary, bivalent metal chalcogenides $M^{2+}Ch^{-2}$ (Ch = S, Se, Te). The most frequent binaries for electronic applications are the II-VI chalcogenide materials (notated II-Ch above), which typically comprise metal cations from groups II and II_B (Zn, Mg, Mn, or Cd, among others). As seen in figure (I.3), II-Ch binaries generally crystallize as wurtzite (WZ), zincblende (ZB, also spelled "zinc blende," that is, sphalerite), rocksalt (RS, i.e., halite), or nickeline (NC, i.e., nickel arsenide). The WZ, ZB, RS, and NC structures crystallize in the $P6_3mc$, $F\bar{4}3m$, $Fm\bar{3}m$, and $P6_3/mmc$ space groups, respectively [21].

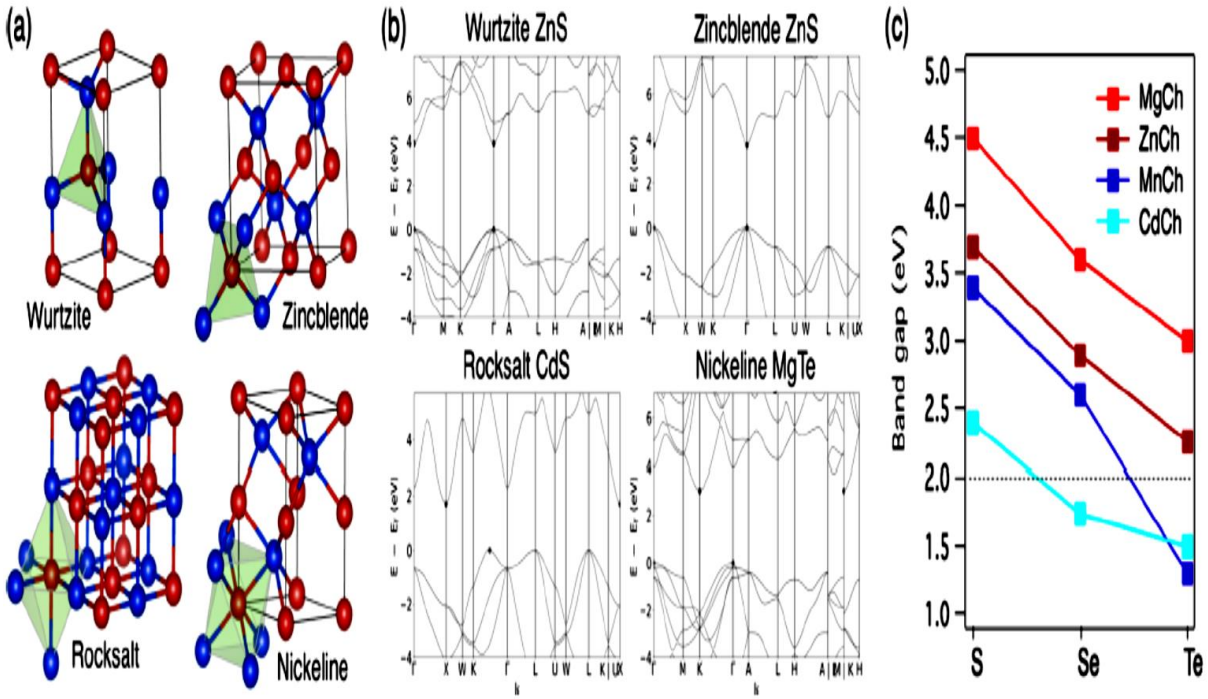

Figure.I.3. (a) The four most common structural forms of binary, bivalent II-Ch metal chalcogenides based on Zn, Mg, Mn, and Cd. (b) Band structures of typical binaries with these crystal structures, derived using a GGA functional and a scissor operation to adjust for experimental band gap from the Materials Project database. (c) As described in this section, experimental band gaps of the most stable structure of each material in this class (see Table I.2) [22].

We have listed in table (I.2), some physical parameters of the above-mentioned experimentally investigated binaries, as well as other binary chalcogenide semiconductors that demand future dopability research. As mentioned in the references above in the Semiconductors: Data Handbook, we list their structure type, gap, doping information, and electrical properties [23].

Table.I.2. Experimentally Investigated Binary Chalcogenides and Their Reported Optoelectronic Properties.

Compound	Structure type	Band gap (eV)	Carrier type	Dopant	Conductivity (S cm^{-1})	Ref
ZnS	ZB	3.7-3.8	N	Al_{Zn}	10^{-3}	24
				F_S	2×10^{-7}	26
ZnS	WZ	3.9	P	Cu_{Zn}	10^{-5}	25
ZnSe	ZB	2.7	n	Ga_{Zn}	20	27
				Cl_{Se}	333	28
			p	N_{Se}	0.02	29
ZnTe	ZB	2.3	P	N_{Te} Cu_{Zn}	25	30
				Sb_{Zn}	0.33	31
					30	32
MgS	ZB	4.5				33
MgS	WZ	4.87				33
MgSe	ZB	3.6-4.05				33
MgTe	ZB	3.5				34
	WZ	3.0				34
MnS	WZ	3.88	P	V_{Mh}	10^{-5}	35
	ZB	3.8				36
	RS	2.8-3.2				37
MnSe	RS	2.5				38
	ZB	3.4				39
	WZ	3.5-3.8				40
MnTe	NC	1.3	P		5-6	26
	ZB	3.2				41
	WZ	2.7				26
CdS	WZ	2.5	n	In_{Cd}	50	42
			p	Cu_{Cd}	2	43
	ZB	2.3-2.4				44
	RS	1.5-1.7				45
BeS	ZB	5.5				46
BeSe	ZB	4.0-5.6				47
BeTe	ZB	2.7-2.8	P	N_{Te}	86	48
SnS_2	Layered $P\bar{3}m1$	2.1-2.2	n	Vs	$1\text{-}10^{-7}$	49
		2.9	p	S-doped	10^{-7}	50
In_2S_3	Defect Spinel $I4_1/amd$	1.80-2.75	N	Intrinsic	2×10^{-4}	51
				Sn_{In}	30	52
TaS_2	Layred $P6_3/mmc$	2.3	N	100		33
HfS_3	Monoclinic $P2_1/m$	3.1	P	0.01		33
γ-Gd_2S_3	Orthorombic pnma	3.4	N	0.004		33

2.2 Chalcogenides-based ternary compounds I−III−Ch_2

Ternary chalcogenide semiconductors of the I–III–VI_2 type have received considerable attention over the last decades due to their physical, photoconductivity characteristics, and other beneficial intrinsic properties, which make them suitable candidates for photovoltaic cells [53]. Among different materials, $CuInSe_2$, $CuInS_2$ and Cu_2SnS_3 are effective light-absorbing materials, which can be used in thin-film solar cells or in printable and flexible

photovoltaic devices. These materials possess advantageous properties for solar applications, since their band gap energy is at the red edge of the visible solar spectrum (bulk $CuInSe_2$ and $CuInS_2$ have band gap energies of 1.05 and 1.5eV, respectively) [54]. Moreover, also chalcopyrite, $CuFeS_2$ represents earth-abundant thermoelectric material [55].

Below we will categorize some of the common sections of ternary chalcogenides.

2.2.1 Chalcopyrites

Now we'll take a look at ternary chalcogenide semiconductors. The group IB transition metal cation is Cu^{1+} or Ag^{1+}, the group III metal cation is Al^{3+}, Ga^{3+}, or In^{3+}, and the chalcogenide anion Ch_2 is S_2, Se_2, or Te_2 in the IB^{+}-III^{3+}-Ch_2 ternary chalcopyrite category (simplified as I-III-Ch_2 hereunder). For more than 50 years, wide-gap chalcopyrites have been studied in depth for their fascinating characteristics and uses [56-59]. Their structure is common for P and as anions, as well as Chalcogens, and their name comes from the chalcopyrite mineral $CuFeS_2$. Figure I.4.a depicts the crystal structure of $CuAlS_2$, a typical compound with a tetragonal $I\bar{4}2d$ space group and tetrahedral anions and cations.

With a unit cell twice as large and metal species I and III alternating between sites, the chalcopyrite structure is an isoelectronic ternary analog of the (II-IV) zincblende structure previously identified. It differs from zinc-blends because to its cation ordering and tetragonal distortion caused by (I-Ch) and link lengths, which may be measured using an anion displacement parameter [60].

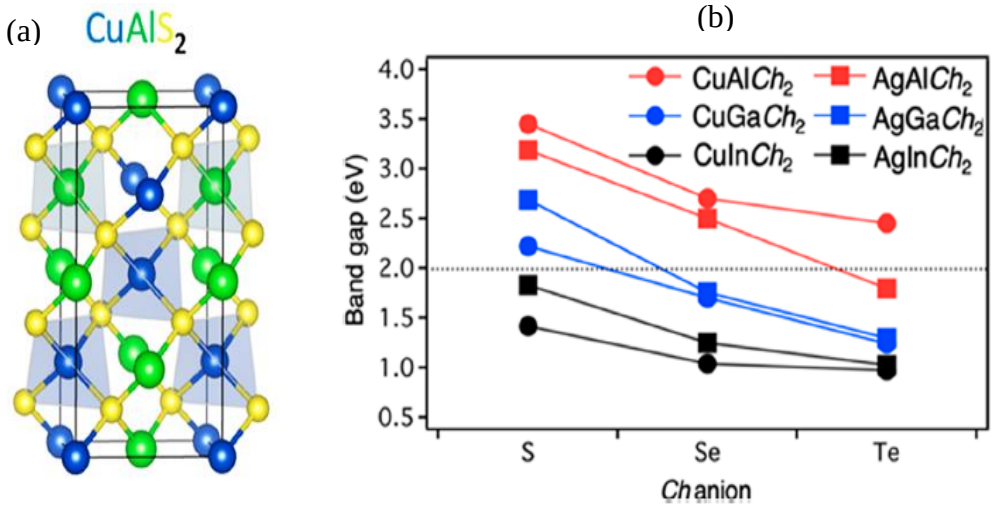

Figure.I.4. (a) Illustration of the chalcopyrite structure, represented by $CuAlS_2$, and (b) experimentally measured band gaps of I-III-Ch_2 semiconductors using the DFT+U+G_0W_0 density of states from Zhang et al [61].

The I-III-Ch system has 18 potential chemistries when all of the ion combinations are included. The experimentally determined optical band gap of these materials as a function of chalcogenide anion is shown in Figure I.4-b (representative reports listed in Table I.3). The electronegativity of the Ch anion, the electronegativity difference between the two cations, and the atomic number are all positively associated with the band gap magnitude (e.g., decreases along Al, Ga, In). The degree of intrinsic localization and covalent bonding tendencies of the Cu 3d (and Ag 4d) states are similarly influenced by the various cations combinations; for example, shorter CuS bonds lead to greater pd VB hybridization and decreased hole effective masses [61].

$CuAlS_2$, $CuAlSe_2$, $CuAlTe_2$, $CuGaS_2$, $AgAlS_2$, $AgAlSe_2$, $AgAlTe_2$, and $AgGaS_2$ are the eight stable semiconductors in this system with documented experimental band gaps exceeding 2eV [61].

2.2.2 I−III−Ch_2 Alloys

To stabilize polymorphs and adjust the band gap, conductivity, and band edges toward a specific application, I-III-Ch_2 semiconductors can produce diverse multinary alloys. Figure (I.5) depicts the band gap vs lattice constants for all of the I-III-Ch_2 chalcopyrite structures discussed above, as well as a few more with gaps less than 2eV, to help visualize this alloy space. The effects of band gap bowing in chalcopyrites are not displayed, but many of these band gap dependencies have been demonstrated to be close to linear computationally and empirically, with bowing values typically smaller than 0.5 eV. (See below) [62,63].

Also, despite nonisostructural and multicomponent alloying are commonly used in this region, such as zincblende (Be, Mg, Zn)Se used for UV lasers [64] and quinternary alloys $CuAl_xGa_{1-x}(S_{1-y}Se_y)$ [65], alloy band gaps are only drawn here between isostructural systems with one substitution. We go over three ways for alloying I, III, or Ch ions briefly, as well as some example chalcopyrite alloys.

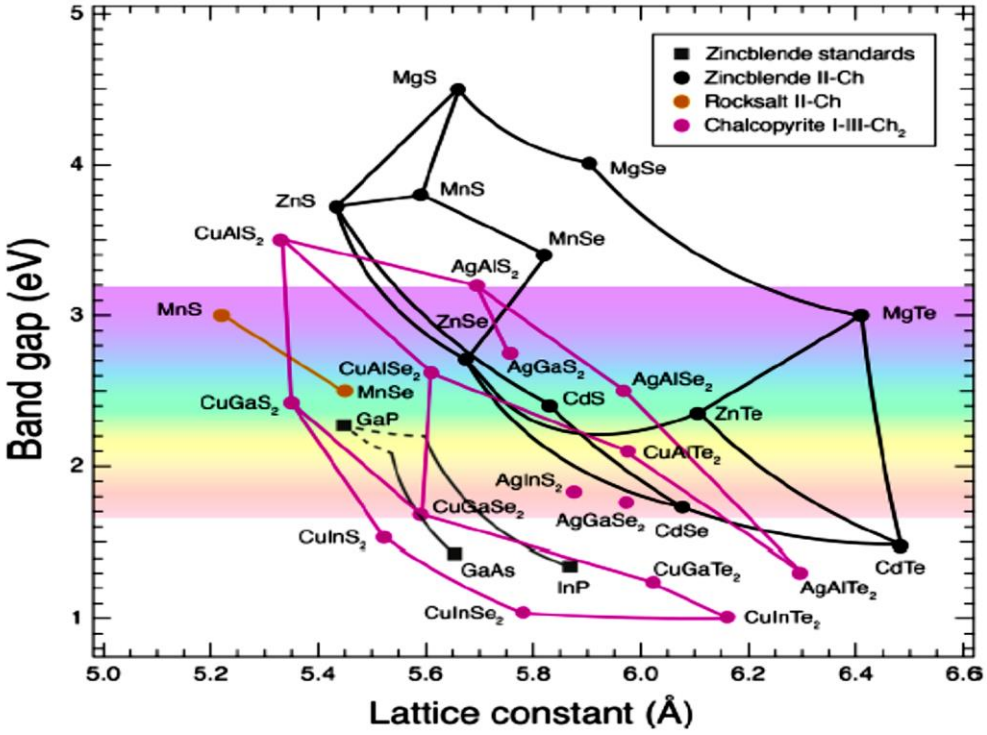

Figure.I.5. Band gap vs. lattice constant for zincblende II-VI chalcogenides, rocksalt II-VI chalcogenides, and ternary I-III-VI_2 chalcopyrite chalcogenides at room temperature [66].

- **(Cu, Ag)-III-Ch_2:** Cu_xAg_{1-x}III-Ch_2 can be made by alloying Cu-III-Ch_2 with Ag-III-Ch_2. $Cu_xAg_{1-x}AlS_2$ polycrystalline thin films made by chemical spray pyrolysis at 360 °C, for example, have been described, however they have a tendency to oxidize due to residual oxidant in the precursor. Although the bending parameter was not provided, it was discovered that the optical band gap changed nonlinearly with respect to x [67]. With a large bending parameter of 0.8 eV, the structural and optical characteristics of bulk $Cu_xAg_{1-x}GaS_2$ materials were examined [68].

- **I-(Ga, Al)-Ch_2:** $CuGa_{1-x}Al_xS_2$ alloys were shown to satisfy Vegard's rule experimentally, with a near-linear gap versus lattice constant relationship and a bowing parameter of 0.34 eV [69,70]. $CuGa_{1-x}Al_xSe_2$ has had its absorption studied more thoroughly, with a reported bowing parameter of 0.28 eV [71,72]. Co_{Cu} doping, in particular, has been investigated as a way to change absorption. This blend of qualities has also been deposited as a layered hetero-structure, which is another method of achieving a mix of traits [73,74].

- **I−III-(S, Se and Te)$_2$:** $CuAl(S_{1-x}Se_x)_2$ single crystals have a reported bending value of 0.34 eV, while $CuGa-(S_{1-x}Se_x)_2$ has a bowing parameter of almost zero [72]. As solar absorbers, both systems have been investigated. $CuAl-(S_{1-x}Se_x)_2$ transport

characteristics have been estimated for thermoelectric applications, yielding p-type conductivity and a low theoretical power factor [75].

2.2.3 Chalcostibites and emplectites compounds

$Cu(In,Ga)Se_2$ (CIGS) has been touted as one of the most promising thin-film solar cell materials. ZSW in Germany has claimed a 22.6% efficient CIGS thin-film solar cell [76]. However, the availability of the rare elements indium and gallium may limit their mass manufacture in the future [77]. As indium-free photovoltaic materials, $Cu_2ZnSn(S,Se)_4$ (CZTS) has gotten a lot of attention. IBM researchers developed a CZTS solar cell that has a 12.6% efficiency [78].

$CuSbS_2$, a novel type of In-free Cu chalcogenide, has also been investigated. Ikeda et al. created a $CuSbS_2$ solar cell with a 3.13% efficiency [79]. $CuSbS_2$ films were created by sulfurizing a Cu and Sb electrodeposited stacked metallic precursor film on a Mo-coated glass substrate. $CuSbSe_2$ solar cells with efficiency more than 3% were reported by NREL. They used a self-regulated sputtering technique to make $CuSbSe_2$ films [80]. The thermoelectric materials $CuSbSe_2$ and $CuM_{0.02}Sb_{0.98}Se_2$ [M=Ti,Pb] have also been investigated [81]. $CuSbS_2$ and $CuSbSe_2$ crystal structures were found to have orthorhombic chalcostibite-type structures with a *Pnma* space group (N^o. 62). We recently used first-principles calculations to determine the electronic structure of chalcostibite-type $CuSbS_2$ and $CuSbSe_2$ [82]. The valence band maxima of $CuSbS_2$ and $CuSbSe_2$ were placed at the Γ-point in their band structure computed with the HSE06 hybrid functional, whereas the conduction band minima were located at the R-point. The Γ-point, whose energy level was roughly identical to the R-point, was their second-lowest conduction band.

The solid solutions $CuSbS_2$, $CuSbSe_2$, and $CuSb(S,Se)_2$ have a chalcostibite structure with an orthorhombic space group system (Pnma). The diffuse reflectance spectra of ultraviolet/visible/near-infrared spectroscopy were used to calculate the indirect and direct band gap energies of $CuSb(S, Se)_2$ solid solutions [83].

The indirect and direct band gap energies of $CuSb(S, Se)_2$ (0.0x1.0) samples estimated by diffuse reflectance spectra are shown in Figure I.6. $CuSbS_2$ has indirect and direct band gap energies of 1.40 and 1.45 eV, respectively. The energy of the direct band gap is 1.45eV, which is slightly higher than the energy of the indirect band gap, which is 1.40 eV. $CuSbSe_2$ has indirect and direct band gap energies of 1.04 and 1.08 eV, respectively. The difference in band gaps between indirect and direct is negligible. The $CuSb(S, Se)_2$ solid

solution's indirect band gap decreases linearly from 1.40 eV of $CuSbS_2$ (x=0.0) to 1.04 eV of $CuSbSe_2$ (x=1.0). The direct band gap of the $CuSb(S, Se)_2$ solid solution decreases linearly from 1.45 eV for $CuSbS_2$ (x=0.0) to 1.08 eV for $CuSbSe_2$ (x=1.0) [83].

Because of their high absorption coefficient, non-toxic nature, low cost (abundant elements), and environmental friendliness, $CuSbS_2$ and $CuSbSe_2$ are currently being discussed as promising materials for solar cell applications [84, 85].

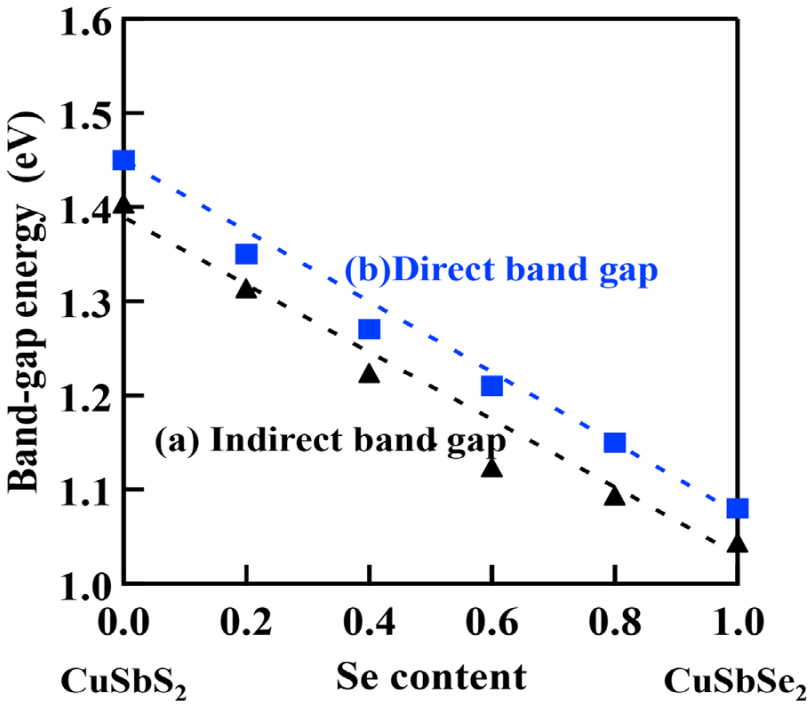

Figure.I.6. Diffuse reflectance spectra were used to estimate the indirect (a) and direct (b) band gap energies of the $CuSb(S_{1-x}Se_x)_2$ system [86].

$Cu(Sb/Bi)S_2$ containing heavy group-V elements Sb or Bi, i.e., $CuSbS_2$ (CSS) or $CuBiS_2$ (CBS) as ternary compound [87-94], can be used as a base compound for alloying to adjust the electronic band edges, such as $CuSb(Se_{1-x}Te_x)_2$ alloy (CSST) and $CuBi(S_{1-x}Se_x)_2$ alloy (CBSS) [95]. $Cu_3(Sb/Bi)S_3$ $(Sb/Bi)S_3$ $(Sb/Bi)S_3$ $(Sb/Bi)S_3$ $(Sb/Bi)S_3$ $(Sb/Bi)S_3$ $(Sb/Bi)S_3$ $(Sb/Bi)S_3$ (Both the VBM and the conduction band minimum (CBM) can be tuned for the overall band profile of the solar cell device, which includes the buffer layers, window layer, and electrodes, using the right cation and anion alloying combinations. One can, at the same time, to certain extend also minimize the lattice mismatching between the absorber and buffer layers. (This can also be done by choice of proper buffer layer material) [96-100].

2.2.4 Other Ternary Chalcogenides

- **Cu_3MCh_4 Sulvanite-like Materials**

Cu_3MCh_4 is a group of copper-based chalcogenide semiconductors, where M stands for group VB transition metal V, Nb, Ta, and Ch stands for S, Se, Te. They have the same cubic sulvanite structure (space group $P\bar{4}3m$), resulting in isotropic optical and electrical characteristics. The structure of the example compound Cu_3TaS_4 is shown in Figure I.7.a. M cations are centered in the unit cell's corner, whereas Cu cations are edge centered. Ch anions tetrahedrally coordinate all M and Cu cations [101].

This isotropic cubic structure eliminates the requirement for special crystal substrates for epitaxial development of anisotropic Cu-based large band gap p-type semiconductors, which also necessitate high growth temperatures and are difficult to achieve ohmic contact with. For this system, Kehoe et al. estimated indirect fundamental band gaps that drop down the Ch group and increase up the Mgroup. Figure I.7.c shows the band structure of Cu_3TaS_4, which corresponds to an average electron effective mass of 1.36 and a hole effective mass of 1.01, implying significant hole mobilities [102].

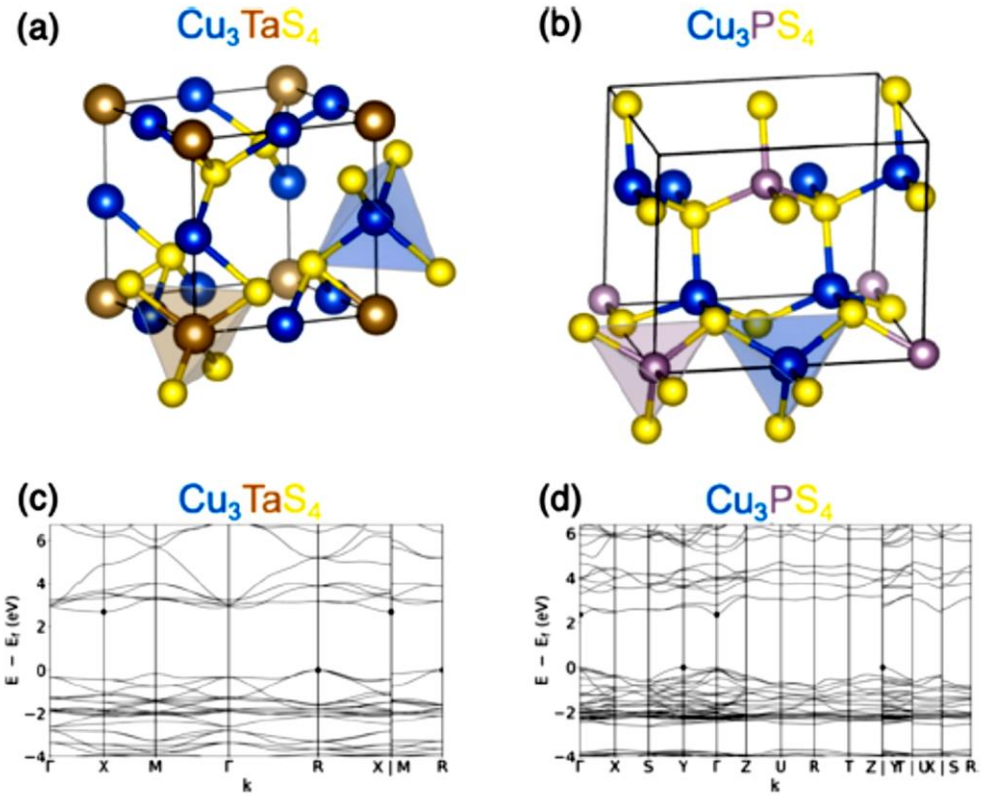

Figure. I.7. From the Materials Project database, (a) sulvanite Cu_3TaS_4 crystal structure, (b) sulvanite-like Cu_3PS_4 crystal structure, and (c, d) their corresponding GGA electronic band structures, with a scissor operation done to adjust for experimental band gap values [102].

- **$ABCh_2$ Delafossites**

$CuAlO_2$, which crystallizes in the delafossite structure (R3m space group) and was chosen based on chemical manipulation of the valence band, was the first predicted p-type widegap conducting oxide [103]. Other delafossite oxides, such as the highly conductive (although relatively absorbing) Mg-doped $CuCrO_2$ [104] and ambipolar $CuInO_2$ [105], were next produced as p-TCOs.

The computationally predicted wide-gap oxide and chalcogenide delafossite compounds $ABCh_2$ (Ch = O, S, Se, Te) for p-type dopability have recently been examined, indicating promise in this class of ternary chalcogenides, if they can be stabilized [106].

For comparison, the crystal structure of KYS_2, another promising chemical, is given in Figure I.8. For nearly all of these compounds, branch point energy calculations showed midgap Fermi stabilization energies, which is not definitive of doping type, and so defect calculations are still needed. Although the goal of this research is to create p-type transparent conductors, the predicted structures could also be useful in other applications, such as those that take use of their magnetic properties.

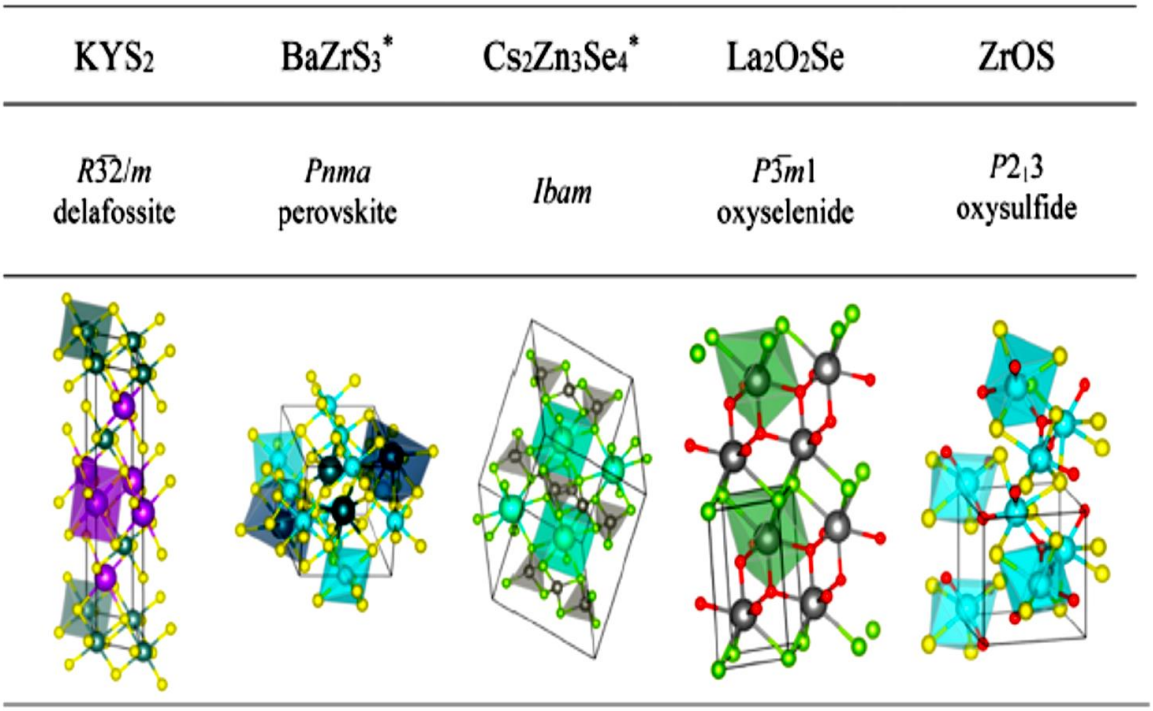

Figure.I.8. Chemical compositions and crystal structures of a representative set of computationally predicted wide-gap p-type dopable chalcogenides, with polyhedra to emphasize coordination. The symbol "*" denotes a new material that did not exist in the ICSD or Materials Project databases at the time the prediction research was conducted [105].

- **$ABCh_3$ Perovskites**

Perovskites are a form of ternary material that can be found as both n-type and p-type transparent conducting oxides, such as n-type $CdSnO_3$ (CTO) [107] and n-type $CdSnO_3$ (CTO). p-type La:$BaSnO_3$ [108], p-type $LaCrO_3$ [109]. and in:$SrTiO_3$ (ISTO) [110].

Several compounds with wide band gaps (EG>2 eV) and low hole effective masses (m*< 1) that could be investigated as p-type transparent conductors were discovered during a computational study looking for new sulfide perovskite materials as photoelectrochemical (PEC) absorbers, including $BaZrS_3$, $BiGaS_3$, $BiScS_3$, $CaZrS_3$, and $ZrCdS_3$ [111]. These structures were screened for defect tolerance to verify there were no defect states in the middle of the gap, however p-type dopability was not confirmed and is still being explored.

- **$A_2B_3Ch_4$ and Dimensional Reduction**

Many binary chalcogenides, except the materials listed in the previous section, have gaps less than 2 eV. By starting with tiny band gap binary constituents and growing their gaps, the dimensional reduction is a promising technique for expanding the space of large band gap ternary compounds [112]. For example, by admixing with Cs_2Ch, small gap binary chalcogenides MCh (Ch = S, Se, Te) can obtain a bigger gap, thus reducing dimensionality (i.e., introducing layers) and orbital overlap. However, lower dispersion due to weakened covalent bonding and therefore greater hole effective masses is a trade-off of this approach, which is the opposite trend as going from II-Ch to I-III-Ch_2 material systems.

The ternaries $Cs_2Zn_3Se_4$ and $Cs_2Zn_3Te_4$ (see Figure I.8) were presented as promising p-type TCs, with HSE06 gaps of 3.61 and 2.82 eV and hole effective masses of 1.23 and 1.25, respectively, based on this technique. $Cs_2Zn_3Se_4$ and $Cs_2Zn_3Te_4$ were discovered to be innately p-type materials when they were not doped. The free hole concentration, on the other hand, may be limited by the low energy of native donor defects, such as Zn interstitials Zni [113]. $Tl_2Hg_3S_4$ and $K_2Hg_3S_4$ with gaps of 2.22eV and 2.2-2.6eV, respectively, were proposed in another dimensional reduction investigation with HgCh [114]. Because the dimensional reduction technique has only been applied to a few classes of binary chalcogenides that have yet to be investigated experimentally, more research into this strategy is needed.

- **A_3BCh_3 and Other Ternaries**

The wittichenite structure ($P2_12_12_1$ space group) of Cu_3SbS_3 has a computed HSE gap of 2.02 (indirect) and 2.14 (direct), whereas nanowires with an experimental optical gap of 2.95 eV have been observed [115]. To widen the gap, this material has been doped with O_S. Li_3SbS_3, Na_3SbS_3, and $Ca_2Sb_2S_5$ were found to exhibit gaps of 2.96, 3.14, and 2.11 eV, respectively, and low hole effective masses (not stated) in a screening of antimony-based thermoelectric sulfides [116]. These materials have not yet been synthesized experimentally, to our knowledge. This shows that information gleaned from thermoelectric material screens could be used to develop new wide-gap chalcogenides**.**

Spinels and spinel-like AB_2Ch_4 compounds, such as Ba_2GeSe_4, Ba_2SiSe_4, (both anticipated p-type dopable), $SrAl_2Se_4$ Al_2ZnS_4 (unlikely p-type dopable), and Al_2CdS_4, as well as BaB_2Se_6 and IrSbS, are among the wide-gap ternary chalcogenides predicted computationally (see Table I.3).

Table I.3 lists the above-mentioned experimentally proven ternary chalcogenides. We include several other experimentally achieved ternary chalcogenides with broad band gaps at the end of the table.

2.3 Quaternary and mixed-anion chalcogenides

In the current research and application of quaternary chalcogenide solar materials, there is a general impasse. On the one hand, CIGS (copper indium gallium selenide) solar cells have gotten a lot of press because of their high power conversion efficiency and stability. These materials, on the other hand, provide a possible environmental risk due to Se toxicity and are economically unfavorable due to the restricted availability and high cost of In and Ga [140–143]. Individual ingredients in CIGS can be substituted as a solution. Stannite (Cu_2FeSnS_4) and kesterite (Cu_2ZnSnS_4), for example, are intriguing alternatives to traditional solar materials [142, 144, 145]. They have an optimal band gap, a high absorption coefficient, and good radiation stability. The elemental components are environmentally friendly (S is used instead of hazardous Se), inexpensive, and readily available (earthabundant Fe, Zn, and Sn are used instead of uncommon In and Ga).

Table.I.3. Experimentally Investigated Ternary Chalcogenides and Their Reported Optoelectronic Properties.

Compound	Structure Type	Band gap (eV)	Carrier type	Conductivity (S cm^{-1})	Refs
$CuAlS_2$	Chalcopyrite	~ 3.4-3.5	p	Bulk(0.9)	117
				Thin film(0.016)	118
				250	119
				4.6	120
				1	121
				63.5	122
				41.7	123
$CuAlSe_2$	Chalcopyrite	~ 2.6-2.7	p	3.3×10^{-3}	123
				123	123
			n	2.3×10^{-3}	123
				50	124
$CuAlTe_2$	Chalcopyrite	~ 2.1-2.5	p	10^{-3}	125
$CuGaS_2$	Chalcopyrite	2.22-2.55	p	Bulk(1.7)	126
				Thin film(0.7)	127
				Single crystal(0.83)	128
$AgAlS_2$	Chalcopyrite	~ 3.2			129
$AgAlSe_2$	Chalcopyrite	2.5-2.7			130
$AgAlTe_2$	Chalcopyrite	~ 2.3			131
$AgGaS_2$	Chalcopyrite	~ 2.7	p	$< 10^{-5}$	132
$BaCu_2S_2$	α-orthorombic	2.1-2.5	p	0.1-53	7
$BaAg_2S_2$	$CaAl_2Si_2$-type	2 (calculated)			133
Cu_3TaS_4	Sulvanite	3	p	1.6	134
Cu_3TaSe_4	Sulvanite	2.35	p	3×10^{-3}	135
Cu_3NbS_4	Sulvanite	2.6	p	0.1-0.2	136
Cu_3NbSe_4	Sulvanite	~ 2.2	p	1.9	137
Cu_3PS_4	Enargite (sulvanites-like)	2.38	p	0.2-1.0	138
$Cu_3P(S_3Se)$	Enargite (sulvanites-like)	2.06	p	0.2-1.0	138
Ag_3PS_4	Enargite (sulvanites-like)	2.88(calculated)			139
Ag_3PSe_4	Enargite (sulvanites-like)	2.09(calculated)			139

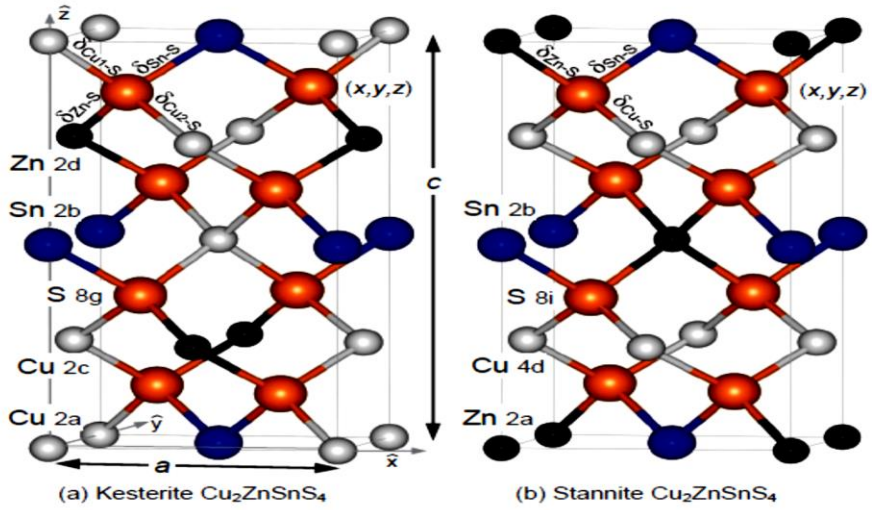

Figure I.9. Conventional cells for (a) kesterite and (b) stannite structures of CZTS [143].

2.3.1 Quaternary Single-Anion Compounds.

The kesterite structure I_2-II-IV-Ch_4, is the quaternary chalcopyrite's extension, which is the most frequent quaternary chalcogenide structure. Although the gap in the p-type kesterite Cu_2ZnSnS_4 (CZTS) is 1.4-1.5eV (perfect for solar absorption), wide-gap materials may exist within this ternary region or in adjacent structural families (e.g, wurtzite-derived stannite). For example, experimental gaps of 2.27 and 2.07eV have been reported for kesterite and stannite Cu_2ZnGeS_4, respectively, and hole conductivity in the stannite phase has been reported up to ~ 1 $S.cm^{-1}$ [144], α- and β-Cu_2ZnSiS_4 have higher band gaps of ~3.0 and ~3.2 eV, respectively [145], but are effectively insulating [146].

Quaternary Lnbased $ALn_xM_yCh_z$ chalcogenides, where A is an alkali or alkalimetal (K, Rb, Cs, Ba, Sr, Cd, Mg) and Ma transition metal (e.g., Cu, Ag, Zn), have been synthesized and solved for crystal structure. Band gaps tend to lie within a window of 2−2.6eV, but there are not many published investigations of optoelectronic properties [147−149]. One such investigation reported the (010) band gaps of $CsYZnSe_3$, $CsSmZnSe_3$, and $CsErZnSe_3$ (Cmcm space group) as 2.41, 2.63, and 2.63 eV, respectively.

$BaYCuS_3$, $BaNdCuS_3$, and $BaNdAgS_3$ have reported gaps of 2.61, 2.39, and 2.31, respectively [150]. In a table, a computationally predicted quaternary wide-gap p-type chalcogenide derived from the sulvanites structure, but one can imagine other such compounds derived from binary and ternary structures. To compare properties of quaternary and mixed-anion chalcogenide semiconductors, we summarize the materials above in Table I.4.

Table I.4. Experimentally Investigated Quaternary and Mixed-Anion Chalcogenide semiconductors and Their Reported Optoelectronic Properties.

Compound	Structure Type	Band gap (eV)	Carrier type	Conductivity ($S.cm^{-1}$)	Refs
Cu_2ZnGeS_4	Kesterite	2.27	P	1	153
LaCuOS	Tetragonal layered	3.1	P	0.26	151
LaCuOSe	Tetragonal layered	~ 2.8	P	140	152
LaCuOTe	Tetragonal layered	2.31	P	1.65	153
BaCuSF	Tetragonal layered	3.2	P	82	154
BaCuSeF	Tetragonal layered	3	P	43	154
BaCuTeF	Tetragonal layered	3	P	167	155
CuSCN	Layered	~ 3.6-3.9	P	2	156
AgSCN	Layered	3.4			157
$Sr_2Cu_2ZnO_2S_2$	Tetragonal	2.7	P	0.12	158
$Sr_2CuGaO_3S_2$	Tetragonal		P	2.4×10^{-2}	159
$Sr_3Cu_2Sc_2O_5S_2$	Tetragonal	3.1	P	2.8	160

3. Applications

We highlight the numerous functions that chalcogenide semiconductors play in various electronic devices in this section, concentrating on their particular advantages over other materials when appropriate.

Table I.5. Chalcogenides in materials science [161].

Chalcogenide	Application
$CuInS_2$, $CuInSe_2$, CuZnSnS4, $CuIn_xGa_{(1-x)}Se_2$	*Solar energy conversion*
ZnS, PbS, Ag_2S, CdSe	*Infrared windows and detectors*
PbS, CdS, BeZnSeTe, $CuInS_2$	*Light-emitting diodes*
FeS, Co_9S_8, MoS_2, WS_2, CoS_2	*Hydrogen evolution and storage*
$Cu_{12}Sb_4S_{13}$, CuS, CuSe, Cr_2S_3	*Thermoelectricity*
Tis_2, MoS_2, WS_2, NiS_2, GeS	*Lithium and sodium-ion batteries*
ZnS:Mn, SrS:Ce, $BaAl_2S_4Eu$	*Luminescence*
Ag_2S, PbS	*Ion-selective electrodes*
Cr_5S_6, $Fe_xMn(1-x)S$, $Co_xMn_{(1-x)}S$	*Giant magnetoresistors*
CdS, CdSe, CdTe, Ag_2S	*Diagnstics*
MoS_2, Sb_2S_3, SnS, WS_2, FeS	*Wear resistance*
MoS_2, FeS, ZnS, RuS_2, WS_2	*Catalysts*

Chalcogenides based thin films solar cells

1. PV materials choice criteria

When light strikes a photovoltaic (PV) cell, it can be reflected, absorbed, or pass directly through the cell. The PV cell is made of semiconductor material, which conducts electricity better than an insulator but not as well as a good conductor like metal. PV cells make use of a variety of semiconductor materials.

When exposed to light, the semiconductor absorbs the energy and transfers it to negatively charged particles in the material known as electrons. This extra energy enables electrons to flow as an electrical current through the material. This current is extracted via conductive metal contacts – the grid- like lines on solar cells – and used to power your home and the rest of the electric grid.

The efficiency of a PV cell is simply the amount of electrical power coming out of the cell in relation to the energy from the light shining on it, indicating how effective the cell is at converting energy from one form to another. The amount of electricity produced by PV cells is determined by the characteristics of the available light (such as intensity and wavelengths) as well as the cell's multiple performance attributes.

The bandgap of PV semiconductors is an important parameter because it indicates what wavelengths of light the material can absorb and convert to electrical energy. If the bandgap of the semiconductor matches the wavelengths of light shining on the PV cell, the cell can efficiently use all of the available energy [162].

2. PV materials and technologies

Year after year, conversion efficiencies in various types of solar cells improve [163]. Multijunction cells, single-junction gallium arsenide (GaAs) cells, crystalline silicon (c-Si) cells, thin film technologies, and new developing technologies are the five main types of semiconductors (see Figure I.10). Multijunction cells have a conversion efficiency of 40% (46% for the best [163]); single-junction gallium arsenide cells have a conversion efficiency of 27% - 29% in the lab (29.3 % for the best [162]); c-Si cells have a conversion efficiency of 25% - 30% (27.6% for the best [164]); conversion efficiency for thin film technologies is 20 percent 25% (23.3% for the best [165]); conversion efficiency for new e (the highest efficiency of perovskite rapidly becomes 22.1% [166], but it has a poor stability). These figures for solar cell efficiency are from December 2021. Solar cells are already a very

important technique to produce renewable energy, and their importance is projected to rise in the future, thanks to ever-improving efficiencies.

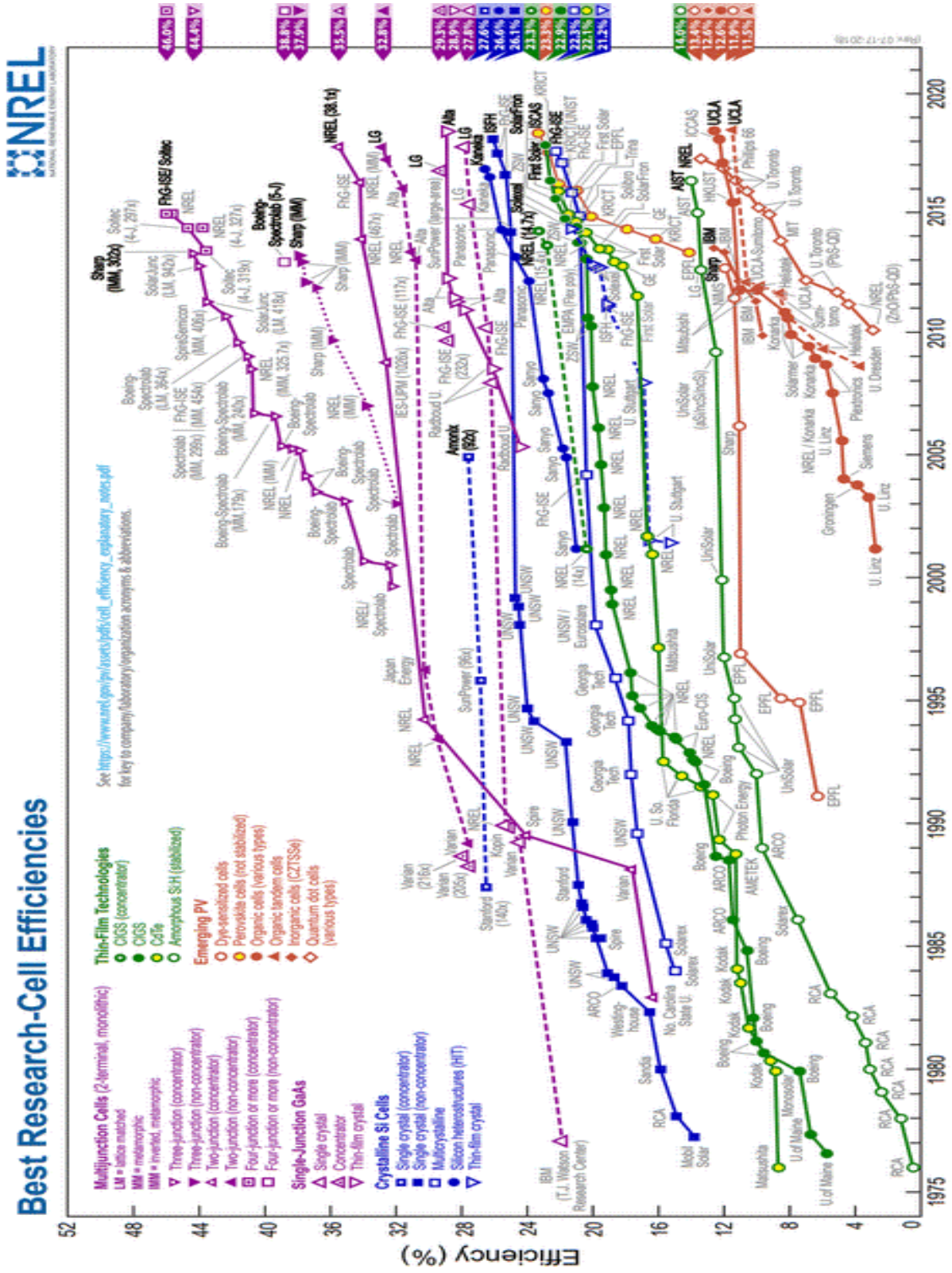

Figure I.10. Best research-cell efficiencies for several solar cell technologies around the world [162].

Thin film solar cells, with a thickness of 1–2 m, are solar cells created by depositing one or more thin layers. This permits cells to be rather thin, resulting in lighter, more cost-effective, and more systems that are flexible. Thin film solar cells have a lower record efficiency than c-Si, which is 23.3% using copper indium gallium selenide (CIGS $CuIn_{1-x}Ga_xSe_2$) with concentrator by the National Renewable Energy Laboratory (NREL) in Golden, Colorado [165] and 22.6% without concentrator by the Centre for Solar Energy and Hydrogen Research Baden-Württemberg (ZSW) [167]. Copper zinc tin sulfide selenide (CZTSSe, $Cu_2ZnSn(S_{1-x}Se_x)_4$), perovskite cells, quantum dot cells, dye-sensitized cells, and shortly CZTSSe cells have already achieved a record efficiency of 12.6% in IBM [168]. There are no hazardous elements in CZTSSe (though Se can be toxic in large amounts). The Korea Research Institute of Chemical Technology (KRICT) has set a new record for perovskite cell efficiency of 22.1% [165]. Perovskite cells have only been used in solar cells since 2009 [167-169], and their conversion efficiency has increased dramatically from 3.8 percent to 22.1% in just seven years.

2.1 Thin-Film Photovoltaics

A thin-film solar cell is created by depositing one or more thin layers of PV material on a supporting material like glass, plastic, or metal. On the market today, there are two main types of thin-film PV semiconductors: cadmium telluride (CdTe) and copper indium gallium diselenide (CIGS). Both materials can be deposited directly onto the module's front or back surface.

After silicon, CdTe is the most commonly used PV material, and CdTe cells can be produced using low-cost manufacturing processes. While this makes them a more cost-effective option, their efficiencies are still not as high as silicon's. In the lab, CIGS cells have optimal properties for a PV material and high efficiencies, but the complexity of combining four elements makes the transition from lab to manufacturing more difficult. To enable long-term outdoor operation, CdTe and CIGS both require more protection than silicon.

Copper indium gallium selenide ($Cu(In,Ga)Se_2$, CIGS) and cadmium telluride (CdTe)-based solar cells are the most promising thin film technologies that have already reached the commercial stage. At the research and development scale, solar submodules above 18% for these two technologies have been reported [167] while commercially available modules exhibit total area efficiencies in the range 14-16% depending on the manufacturer and the technology [166-168].

Concerns about the toxicity of Cd as well as the potential scarcity of Te and In have triggered intense research effort to find more earth-abundant and non-toxic thin film absorber materials for solar cells. $Cu_2ZnSn(S, Se)_4$ (CZTS) has been identified as a potential alternative that matches well the previously mentioned criteria. Record solar cell efficiency for this material is 12.6% at the research scale denoting a high improvement potential [169].

3. Chalcogenide thin films solar cells state of the art

Copper-based chalcogenide absorber materials such as CIGS, CZTSSe, and other possible copper-based chalcogenide absorber materials (see Table I.6). They all have strong absorption coefficients, and the gap energies can be tuned to be suited for PV applications by alloying them.

Table I.6. Abbreviation of main copper-based absorber materials, where the alloy composition x can vary from 0 to 1 [170].

Abbreviation	Description
CIS	$CuInSe_2$
CGS	$CuGaSe_2$
CIGS	$CuIn_{1-x}Ga_xSe2$
CZTS	Cu_2ZnSnS_4
CZTSe	$Cu_2ZnSnSe_4$
CZTSSe	$Cu_2ZnSn(S_{1-x}Se_x)_4$
$ZnSn(S/Se)_4$	CZTS and CZTSe
CTGS	$Cu_2Sn_{1-x}Ge_xS_3$
CTSS	$Cu_2Sn_{1-x}Si_xS_3$
$Cu(Sb/Bi)(S/Se)_2$	$CuSbS_2$, $CuSbSe_2$, $CuBiS_2$ and $CuBiSe_2$

Hahn synthesized CIS for the first time in 1953 [171]. In 1974, it was used for the first time as an absorber material in a single crystal solar cell, with a conversion efficiency of 5% [172]. Kazmerski constructed the first thin film solar cell based on a p-CIS and n-CdS heterojunction in 1976. Boeing Corporation conducted foundational research on thin film polycrystalline CIGS solar cells in the 1980s. The highest conversion efficiency in the laboratory to date (January 2014) is 23.3% [173]. In marketed solar cells, $CuIn_{0.7}Ga_{0.3}Se_2$ is

already a well-developed compound. Therefore, more experimental and theoretical studies are expected.

In a wide spectrum of energies, $Cu(Sb/Bi)(S/Se)_2$ has higher absorption coefficients than CIGS and CZTSSe. The localized feature of the Sb/Bi p-like conduction band states can be explained by a multi-valley band structure with flat energy dispersions. $Cu(Sb/Bi)(S/Se)_2$ has indirect band gap energies in the range of 1.0–1.6 eV, according to our calculations. The difference between direct and indirect band gap energies is only 0.2–0.3 eV because the lowest CB is flat [170].

3.1 Copper antimony and bismuth chalcogenides

The compounds in this study are indirect band gap semiconductors with predicted band gap energies ranging between 1.0 and 1.6 eV. The difference in band gap energy between direct and indirect band gaps is only 0.2–0.3 eV. $Cu(Sb/Bi)(S/Se)_2$ has a greater absorption coefficient than CIGS and CZTS, allowing solar cells made using these absorber materials to be thinner and hence less expensive. These findings are in line with those of other researchers [174–179].

Only a few investigations on solar cells based on $Cu(Sb/Bi)(S/Se)_2$ have been published to date. Despite the fact that the compounds are indirect gap materials, they are unique PV absorber materials that are particularly attractive for ultra-thin film solar cells due to their higher absorption coefficients. Solar devices are currently only made of $CuSbSe_2$ and $CuSbS_2$, and they are quite simple to manufacture [180]. To boost efficiency, however, device engineering is required. By alloying the anion with Te ($CuSb(Se_{1-x}Te_x)_2$), the band gap energy can be optimized. Our results also indicate that $CuSb(Se_{1-x}Te_x)_2$ may have slightly higher absorption coefficients than $Cu(Sb/Bi)(S/Se)_2$.

3.2 Potential copper-based chalcogenides

CIGS is already a commercialized absorber material and CZTSSe is under development. However, finding alternative absorber materials is an ongoing research. $Cu_2Sn_{1-x}GexS_3$ (CTGS) and $Cu_2Sn_{1-x}Si_xS_3$ (CTSS) are potential solar cell materials. Despite a few studies of Cu_2SnS_3, Cu_2GeS_3, and Cu_2SiS_3 [181–186], only few groups reported the investigations of the corresponding alloys [186,187]. The conversion efficiencies of 4.63% and 4.29%, using Cu_2SnS_3, were achieved by Nakashima et al. [188] and Kanai et al. [189], respectively. Cell efficiency of 6.0% was obtained for $Cu_2Sn_{0.83}Ge_{0.17}S_3$ by Umehara et al.

[190]. Another type of potential candidate materials are $Cu(Sb/Bi)(S/Se)_2$ due to higher absorption coefficients. Solar cells based on $CuSbS_2$ and $CuSbSe_2$ have been fabricated by Septina *et al*., [191] and Welch *et al*., [192] with conversion efficiency of ~3%.

4. Conclusion

In this chapter, we focused on distinctive physical bonding and properties of chalcogenides and then covered general classes of chalcogenide semiconductors that have been experimentally synthesized, including binary chalcogenides MCh (e.g., ZnCh), ternaries (represented by chalcopyrites, for example, $CuAlCh_2$, chalcostibites, emplectites, like $Cu(Sb/Bi)(S/Se)_2$, sulvanites, for example, Cu_3TaCh_4, α-$BaCu_2S_2$, and related structures), layered mixed-anion oxychalcogenides (e.g., LaCuOCh, Ba-CuChF, etc.), and touched on multinary compounds.

Finally, we look at applications in which chalcogenides are used as an active or passive layer, such as photovoltaic and photo-electrochemical solar cells, transistors, and light-emitting diodes. By evaluating, categorizing, and discussing potential prospects in chalcogenides, this section of the study aims to encourage further research on this growing class of semiconductors and thus enable future advancements in optoelectronic devices.

5. References

[1] M. Taylor, P. Ralon, and A. Ilasi, "The power to change: Solar and wind cost reduction potential to 2025," tech. rep., IRENA, 2016.

[2] Sahib Hasan, Puja Adhikari, Khagendra Baral, and Wai-Yim Chinga) Conspicuous interatomic bonding in chalcogenide crystals and implications on electronic, optical, and elastic properties : AIP Advances 10, 075216 (2020).

[3] Cheng, J.; Fan, D.; Wang, H.; Liu, B.; Zhang, Y.; Yan, H. Chemical Bath Deposition of Crystalline ZnS Thin Films. Semicond. Sci. Technol.2003, 18, 676−679.

[4] Choi, J. Y.; Kim, K.-J.; Yoo, J.-B.; Kim, D. Properties of Cadmium Sulfide Thin Films Deposited by Chemical Bath Deposition with Ultrasonication. Sol. Energy 1998, 64, 41−47.

[5] Rodriguez, J.A.; Gordillo, G. Study of Electricla Properties in ZnxCd1-XS Thin Films. Sol. Energy Mater. 1989, 19, 421−431.

[6] R. Woods-Robinson, Wide Band Gap Chalcogenide Semiconductors, *Chem. Rev.* 2020, 120, 9, 4007–4055.

[7] Newhouse, P. F.; Hersh, P. A.; Zakutayev, A.; Richard, A.; Platt, H. A. S.; Keszler, D. A.; Tate, J. Thin Film Preparation and Characterization of Wide Band Gap Cu_3TaQ_4 (Q = S or Se) p-Type Semiconductors. Thin Solid Films 2009, 517, 2473−2476.

[8] Hiramatsu, H.; Kamioka, H.; Ueda, K.; Ohta, H.; Kamiya, T.; Hirano, M.; Hosono, H. Opto-Electronic Properties and Light-Emitting Device Application of Widegap Layered Oxychalcogenides: LaCuOCh (Ch = Chalcogen) and La2CdO2Se2. Phys. Status Solidi A 2006, 203, 2800−2811.

[9] Hatch, S. M.; Briscoe, J.; Dunn, S. A Self-Powered ZnONanorod/CuSCN UV Photodetector Exhibiting Rapid Response. Adv. Mater. 2013, 25, 867−871.

[10] Wang, Z.; Nayak, P. K.; Caraveo-Frescas, J. A.; Alshareef, H. N. Recent Developments in P-Type Oxide Semiconductor Materials and Devices. Adv. Mater. 2016, 28, 3831−3892.

[11] Takahashi, K.; Yoshikawa, A.; Sandhu, A. Wide Band gap Semiconductors 2007.

[12] Zhang, K. H. L.; Xi, K.; Blamire, M. G.; Egdell, R. G. P –Type Transparent Conducting Oxides. J. Phys.: Condens. Matter 2016, 28, 383002.

[13] Morko, H. Handbook of Nitride Semiconductors and Devices; 2008.

[14] Grundmann, M.; Schein, F. L.; Lorenz, M.; Böntgen, T.; Lenzner, J.; von Wenckstern, H. Cuprous Iodide - A p-Type Transparent Semiconductor: History and Novel Applications. Phys. Status Solidi A. 2013, 210, 1671−1703.

[15] Pierson, H. O. Handbook of Refractory Carbides and Nitrides: Properties, Characteristics, Processing, and Applications; 1996.

[16] Delahoy, A. E.; Guo, S. Transparent Conducting Oxides for Photovoltaics. In Handbook of Photovoltaic Science and Engineering; Luque, A., Hegedus, S., Eds.; John Wiley & Sons, Ltd., 2011; pp 716−796.

[17] Allen, M. J.; Tung, V. C.; Kaner, R. B. Honeycomb Carbon: A Review of Graphene. Chem. Rev. 2010, 110, 132−145.

[18] Ruda, H. E. Wide Gap II−VI Compounds for Opto-Electronic Applications; Ruda, H. E., Ed.; Springer Science & Business Media,2013.

[19] S.R.Elliot, J. Non-Crystalline Solids 81, 71-98(1986).

[20] Pravin Kumar Singh and D. K. Dwivedi. Chalcogenide glass: Fabrication techniques, properties and applications ; 2017, VOL. 520, 256–27.

[21] Vaughan, D. J.; Craig, J. R. Mineral Chemistry of Metal Sulfides.Earth-Science Rev. 1978, 15, 494.

[22] Kotochigova, S.; Shirley, E. L.; Levine, Z. Atomic Reference Data for Electronic Structure Calculations; 2002.

[23] Madelung, O. Ix−VIy Compounds. In Semiconductors: Data Handbook, 3rd ed.; Berlin, 2004.

[24] Nagamani, K.; Revathi, N.; Prathap, P.; Lingappa, Y.; Reddy, K.T. R. Al-Doped ZnS Layers Synthesized by Solution Growth Method. Curr. Appl. Phys. 2012, 12, 380−384.

[25] Mohamed, S. H. Photocatalytic, Optical and Electrical Properties of Copper-Doped Zinc Sulfide Thin Films. J. Phys. D: Appl. Phys. 2010, 43, 035406.

[26] Kucukomeroglu, T.; Bacaksiz, E.; Terzioglu, C.; Varilci, A. Influence of Fluorine Doping on Structural, Electrical and Optical Properties of Spray Pyrolysis ZnS Films. Thin Solid Films 2008, 516,2913−2916.

[27] Niina, T.; Minato, T.; Yoneda, K. Ga-Doped ZnSe Grown by Molecular Beam Epitaxy for Blue Light Emitting Diodes. Jpn. J. Appl.Phys. 1982, 21, L387.

[28] Ohkawa, K.; Mitsuyu, T.; Yamazaki, O. Characteristics of Cldoped ZnSe Layers Grown by Molecular-beam Epitaxy. J. Appl. Phys.1987, 62, 3216−3221.

[29] Ohkawa, K.; Karasawa, T.; Mitsuyu, T. Characteristics of PType ZnSe Layers Grown by Molecular Beam Epitaxy with Radical Doping. Jpn. J. Appl. Phys. 1991, 30, L152.

[30] Späth, B.; Fritsche, J.; Klein, A.; Jaegermann, W. Nitrogen Doping of ZnTe and Its Influence on CdTe/ZnTe Interfaces. Appl.Phys. Lett. 2007, 90, 062112.

[31] Gessert, T. A.; Mason, A. R.; Reedy, R. C.; Matson, R.; Coutts, T. J.; Sheldon, P. Development of Rf Sputtered, Cu-Doped ZnTe for Use as a Contact Interface Layer to p-CdTe. J. Electron. Mater. 1995, 24,1443−1449.

[32] Barati, A.; Klein, A.; Jaegermann, W. Deposition and Characterization of Highly P-Type Antimony Doped ZnTe Thin Films. Thin Solid Films 2009, 517, 2149−2152.

[33] Madelung, O. Ix−VIy Compounds. In Semiconductors: Data Handbook, 3rd ed.; Berlin, 2004.

[34] Waag, A.; Heinke, H.; Scholl, S.; Becker, C. R.; Landwehr, G.Growth of MgTe and $Cd_{1-x}Mg_xTe$ Thin Films by Molecular Beam Epitaxy. J. Cryst. Growth 1993, 131, 607−611.

[35] Pramanik, P.; Akhter, M. A.; Basu, P. K. A Solution Growth Technique for the Deposition of Manganese Sulphide Thin Film. Thin Solid Films 1988, 158, 271−275.

[36] Wang, L.; Sivananthan, S.; Sporken, R.; Caudano, R. Interface Properties and Valence-Band Discontinuity of MnS/ZnSe Heterostructures. Phys. Rev. B: Condens. Matter Mater. Phys. 1996, 54, 2718−2722.

[37] Madelung, O. Ix−VIy Compounds. In Semiconductors: Data Handbook, 3rd ed.; Berlin, 2004.

[38] Murray, R. M.; Forbes, B. C.; Heyding, R. D. The Preparation and Paramagnetic Susceptibility of β-MnSe. Can. J. Chem. 1972, 50,4059−4061.

[39] Ishibe, I.; Nabetani, Y.; Kato, T.; Matsumoto, T. MBE Growth and RHEED Characterization of MnSe/ZnSe Superlattices on GaAs (100) Substrates. J. Cryst. Growth 2000, 214, 172−177.

[40] Sines, I. T.; Misra, R.; Schiffer, P.; Schaak, R. E. Colloidal Synthesis of Non-Equilibrium Wurtzite-Type MnSe. Angew. Chem., Int.Ed. 2010, 49, 4638−4640.

[41] Durbin, S. M.; Han, J.; O, S.; Kobayashi, M.; Menke, D. R.;Gunshor, R. L.; Fu, Q.; Pelekanos, N.; Nurmikko, A. V.; Li, D.; et al.Zinc Blende MnTe: Epilayers and Quantum Well Structures. Appl.Phys. Lett. 1989, 55, 2087−2089.

[42] Böer, K. W. Cadmium Sulfide Enhances Solar Cell Efficiency. In Energy Conversion and Management; 2011; Vol. 52, pp 426−430.

[43] Sebastian, P. J. P-Type CdS Thin Films Formed by in Situ Cu Doping in the Chemical Bath. Appl. Phys. Lett. 1993, 62, 2956−2958.

[44] Cortes, A.; Gómez, H.; Marotti, R. E.; Riveros, G.; Dalchiele, E.A. Grain Size Dependence of the Bandgap in Chemical Bath Deposited CdS Thin Films. Sol. Energy Mater. Sol. Cells 2004, 82, 21−34.

[45] Batlogg, B.; Jayaraman, A.; Van Cleve, J. E.; Maines, R. G.Optical Absorption, Resistivity, and Phase Transformation in CdS atHigh Pressure. Phys. Rev. B: Condens. Matter Mater. Phys. 1983, 27,3920−3923.

[46] Yim, W. M.; Dismukes, J. P.; Stofko, E. J.; Paff, R. J. Synthesis and Some Properties of BeTe, BeSe and BeS. J. Phys. Chem. Solids 1972,33, 501−505.

[47] Wilmers, K.; Wethkamp, T.; Esser, N.; Cobet, C.; Richter, W.;Wagner, V.; Waag, A.; Lugauer, H.; Fischer, F.; Gerhard, T.; et al. VUV Ellipsometry on Beryllium Chalcogenides. Phys. Status Solidi B 1999,215, 15−20.

[48] Lugauer, H. J.; Fischer, F.; Litz, T.; Waag, A.; Zehnder, U.;Ossau, W.; Gerhard, T.; Landwehr, G.; Becker, C.; Kruse, R.; et al. PTypeDoping of Beryllium Chalcogenides. Mater. Sci. Eng., B 1997, 43,88−91.

[49] Thangaraju, B.; Kaliannan, P. Spray Pyrolytic Deposition and Characterization of SnS and SnS2 Thin Films. J. Phys. D: Appl. Phys.2000, 33, 1054.

[50] Wold, A.; Dwight, K. Binary Sulfides. In Solid State Chemistry; 1993; pp 171−197.

[51] Barreau, N.; Marsillac, S.; Albertini, D.; Bernede, J. C.Structural, Optical and Electrical Properties of β-$In_2S_{3-3x}O_{3x}$ Thin Films Obtained by PVD. Thin Solid Films 2002, 403−404, 331−334.

[52] Mathew, M.; Gopinath, M.; Kartha, C. S.; P. Vijayakumar, K.;Kashiwaba, Y.; Abe, T. Tin Doping in Spray Pyrolysed Indium Sulfide Thin Films for Solar Cell Applications. Sol. Energy 2010, 84, 888−897.

[53] C. Persson, R. Chen, H. Zhao, M. Kumar, and D. Huang, "Electronic structure and optical properties from first-principles modeling," in Copper Zinc Tin Sulphide-based Thin Film Solar Cells (K. Ito, ed.), John Wiley & Sons, 2015.

[54] Adachi, S.; Ito, K. Physical Properties: Compiled Experimental Data. In Copper Zinc Tin Sulfide-Based Thin-Film Solar Cells; Wiley Online Library, 2015; pp 149−179.

[55] Rosmus, K. A.; Brant, J. A.; Wisneski, S. D.; Clark, D. J.; Kim, Y. S.; Jang, J. I.; Brunetta, C. D.; Zhang, J.-H.; Srnec, M. N.; Aitken, J. A. Optical Nonlinearity in Cu_2CdSnS_4 and α/β-Cu_2ZnSiS_4: Diamondlike Semiconductors with High Laser-Damage Thresholds. Inorg. Chem. 2014, 53, 7809−7811.

[56] Siebentritt, S. Wide Gap Chalcopyrites: Material Properties and Solar Cells. Thin Solid Films 2002, 403−404, 1−8.

[57] Siebentritt, S.; Rau, U. Wide-Gap Chalcopyrites; Berlin, 2006.

[58] Shay, J. L.; Wernick, J. H. Ternary Chalcopyrite Semiconductors: Growth, Electronic Properties, and Applications: International Series of Monographs in the Science of the Solid State, Vol. 7.; Elsevier, 2017.

[59] Pamplin, B. R.; Kiyosawa, T.; Masumoto, K. Ternary Chalcopyrite Compounds. Prog. Cryst. Growth Charact. 1979, 1, 331−387.

[60] Jaffe, J. E.; Zunger, A. Theory of the Band-Gap Anomaly in ABC_2 Chalcopyrite Semiconductors. Phys. Rev. B: Condens. Matter Mater. Phys. 1984, 29, 1882−1906.

[61] Zhang, Y.; Xi, L.; Wang, Y.; Zhang, J.; Zhang, P.; Zhang, W. Electronic Properties of Energy Harvesting Cu-Chalcogenides: P-d Hybridization and d-Electron Localization. Comput. Mater. Sci. 2015, 108, 239−249.

[62] Korzun, B. V.; Fadzeyeva, A. A.; Bente, K.; Schmitz, W.; Kommichau, G. Phase Correlations in the $CuAlSe_2$-$CuAlTe_2$ System. Phys. Status Solidi B 2005, 242, 1581−1587.

[63] Wei, S. H.; Zunger, A. Band Offsets and Optical Bowings of Chalcopyrites and Zn-Based II-VI Alloys. J. Appl. Phys. 1995, 78, 3846−3856.

[64] Niiyama, Y.; Watanabe, M. BeMgZnSe-Based Ultraviolet Lasers. Semicond. Sci. Technol. 2005, 20, 1187−1197.

[65] Ogawa, A.; Sudo, R.; Gupta, A.; Shirakata, S.; Chichibu, S.; Matsumoto, S.; Isomura, S. Preparation and Characterization of Cu(Al, Ga)(s, $Se)_2$ Penternary Alloys. Jpn. J. Appl. Phys. 1993, 32, 588−589.

[66] Ning, C.-Z.; Dou, L.; Yang, P. Bandgap Engineering in Semiconductor Alloy Nanomaterials with Widely Tunable Compositions. Nat. Rev. Mater. 2017, 2, 17070.

[67] Ahmad, S. M. Study of Structural and Optical Properties of. Optik 2016, 127, 10004−10013.

[68] Choi, I.-H.; Eom, S.-H.; Yu, P. Y. The Optical and Vibrational Properties of the Quaternary Chalcopyrite Semiconductor Alloy $Ag_xCu_{1-x}GaS_2$. J. Appl. Phys. 2000, 87, 3815.

[69] Brik, M. G.; Ma, C. G. Tailoring the Electronic and Elastic Properties by Varying the Composition of the $CuGa_{1-x}Al_xS_2$ Chalcopyrite Semiconductor. J. Phys. D: Appl. Phys. 2013, 46, 285304.

[70] Tsuboi, N.; Kobayashi, S.; Kaneko, F.; Maruyama, T. Dependence of Energy Gap on x in $CuAl_xGa_{1-x}S_2$ Mixed Crystal System. Jpn. J. Appl. Phys. 1988, 27, 972.

[71] Shirakata, S.; Aksenov, I.; Sato, K.; Isomura, S. Photoluminescence Studies in $CuAlS_2$ Crystals. Jpn. J. Appl. Phys. 1992, 31, L1071−L1074.

[72] Wei, S. H.; Zunger, A. Band Offsets and Optical Bowings of Chalcopyrites and Zn-Based II-VI Alloys. J. Appl. Phys. 1995, 78, 3846−3856.

[73] Wen-Chen, Z.; Shao-Yi, W.; Bei-Jun, Z.; Shi-Fu, Z. Substitutional Sites of Co_2^+ ions in $CuGa_{1-x}Al_xSe_2$:Co_2^+ Crystals. J. Phys. Chem.Solids 2002, 63, 895−897.

[74] Jin, M. S.; Kim, W. T.; Yoon, C. S. Optical Properties of Undoped and Co-Doped $CuGa_{1-x}Al_xSe_2$ Single Crystals. J. Phys. Chem.Solids 1993, 54, 1509−1513.

[75] Reshak, A. H. Transport Properties of Mixed $CuAl(S_{1-x}Se_x)_2$ as Promising Thermoelectric Crystalline Materials. J. Phys. Chem. Solids 2015, 78, 46−52.

[76] P. Jackson, R. Wuerz, D. Hariskos, E. Lotter, W. Witte, and M. Powalla, Effects of heavy alkali elements in $Cu(In,Ga)Se_2$ solar cells with efficiencies up to 22.6%, Phys. Status Solidi RRL 10, 583 (2016).

[77] C. Wadia, A. P. Alivisatos, and D. M. Kammen, Materials availability expands the opportunity for large-scale photovoltaics deployment, Environ. Sci. Technol. 43, 2072 (2009).

[78] W. Wang, M. T. Winkler, O. Gunawan, T. Gokmen, T. K. Todorov, Y. Zhu, and D. B. Mitzi, Device characteristics of CZTSSe thin-film solar cells with 12.6% efficiency, Adv. Energy Mater. 4, 1301465 (2014).

[79] W. Septina, S. Ikeda, Y. Iga, T. Harada, and M. Matsumura, Thin film solar cell based on $CuSbS_2$ absorber fabricated from an electrochemically deposited metal stack, Thin Solid Films 550, 700 (2014).

[80] A. W. Welch, L. L. Baranowski, P. Zawadzki, S. Lany, C. A. Wolden, and A. Zakutayev, $CuSbSe_2$ photovoltaic devices with 3% efficiency, Appl. Phys. Express 8, 082301 (2015).

[81] D. Li and X. Y. Qina, Thermoelectric properties of $CuSbSe_2$ and its doped compounds by Ti and Pb at low temperatures from 5 to 310 K, J. Appl. Phys. 100, 023713 (2006).

[82] T. Maeda and T. Wada, First-principles study of electronic structure of $CuSbS_2$ and $CuSbSe_2$ photovoltaic semiconductors, Thin Solid Films 582, 401 (2015).

[83] T. Wada and T. Maeda: Optical properties and structures of $CuSbS_2$, $CuSbSe_2$, and $CuSb(S_{1-x}Se_x)_2$, Phys. Status Solidi C, 1600196 (2017).

[84] B. Yang, L. Wang, J. Han, Y. Zhou, H. Song, S. Chen, J. Zhong, L. Lv, D. Niu, and J. Tang, $CuSbS_2$ as a Promising Earth-Abundant Photovoltaic Absorber Material: A Combined Theoretical and Experimental Study, Chem. Mater. 26, 3135-3143 (2014).

[85] D.-J. Xue, B. Yang, Z. -K. Yuan, G. Wang, X. Liu, Y. Zhou, L. Hu, D. Pan, S. Chen, and J. Tang, $CuSbSe_2$ as a Potential Photovoltaic Absorber Material: Studies from Theory to Experiment, Adv. Energy Mater. 5, 1501203 (2015).

[86] K. Takei, T. Maeda, and T. Wada, Crystallographic and optical properties of $CuSbS_2$ and $CuSb(S_{1-x}Se_x)_2$ solid solution, Thin Solid Films 582, 263 (2015).

[87] S.H. Pawar, A.J. Pawar and P.N. Bhosale, Bull. Mater. Sci., 1986, 8, 423.

[88] Y. Rodriguez-lazcano, M.T.S. Nair and P.K. Nair, J. Cryst. Growth, 2001, 223, 399.

[89] P.S. Sonawane, P.A. Wani, L.A. Patil and T. Seth, Mater. Chem. Phys., 2004, 84, 221.

[90] J. Zhou, G.Q. Bian, Q.Y. Zhu, Y. Zhang, C.Y. Li and J. Dai, J. Solid State Chem., 2009, 182, 259.

[91] A. Rabhi, M. Kanzari and B. Rezig, Thin Solid Films 2009, 517, 2477.

[92] D. Colombara, L.M. Peter, K.D. Rogers, J.D. Painter and S. Roncallo, Thin Solid Films 2011, 519, 7438.

[93] M. Kumar and C. Persson. J. Renewable Sustainable Energy 2013, 5, 031616.

[94] M. Kumar and C. Persson, Energy Procedia, 2014, 44, 176.

[95] R. Chen and C. Persson, EPJ Photovoltaics, 2017, 8, 85504.

[96] V. Estrella, M.T.S. Nair and P.K. Nair, Semicond. Sci. Technol., 2003, 18, 190.

[97] N.J. Gerein and J.A. Haber, Chem. Mater., 2006, 18, 6297.

[98] F. Mesa, A. Dussan and G. Gordillo, Phys. Status Solidi C, 2010, 7, 917.

[99] D. Colombara, L.M. Peter, K. Hutchings, K.D. Rogers, S. Schäfer, J.T.R. Dufton and M.S. Islam, Thin Solid Films, 2012, 520, 5165.

[100] M. Kumar and C. Persson, Appl. Phys. Lett., 2013, 102, 062109.

[101] Van De Walle, C. G. Universal Alignment of Hydrogen Levels in Semiconductors and Insulators. Phys. B 2006, 376−377, 1−6.

[102] Kehoe, A. B.; Scanlon, O.; Watson, G. W. The Electronic Structure of Sulvanite Structured Cu_3MCh_4 (M = V, Nb, Ta; Ch = S, Se, Te): Prospects for Optoelectronic Applications. J. Mater. Chem. C2015, 3, 12236−12244.

[103] Kawazoe, H.; Yasukawa, M.; Hyodo, H.; et al. P-Type Electrical Conduction in Transparent Thin Films of $CuAlO_2$. Nature 1997, 389,939−942.

[104] Nagarajan, R.; Draeseke, A. D.; Sleight, A. W.; Tate, J. P-Type Conductivity in $CuCr_{1-x}Mg_xO_2$ Films and Powders. J. Appl. Phys.2001, 89, 8022−8025.

[105] Yanagi, H.; Hase, T.; Ibuki, S.; Ueda, K.; Hosono, H. Bipolarity in Electrical Conduction of Transparent Oxide Semiconductor $CuInO_2$ with Delafossite Structure. Appl. Phys. Lett. 2001, 78, 1583−1585.

[106] Shi, J.; Cerqueira, T. F. T.; Cui, W.; Nogueira, F.; Botti, S.;Marques, M. A. L. High-Throughput Search of Ternary Chalcogenides for p-Type Transparent Electrodes. Sci. Rep. 2017, 7, 43179.

[107] Shannon, R. D.; Gillson, J. L.; Bouchard, R. J. Single Crystal Synthesis and Electrical Properties of $CdSnO_3$, Cd2SnO_4, In_2TeO_6 and $Cdln_2O_4$. J. Phys. Chem. Solids 1977, 38, 877−881.

[108] Kim, H. J.; Kim, U.; Kim, H. M.; Kim, T. H.; Mun, H. S.; Jeon, B.-G.; Hong, K. T.; Lee, W.-J.; Ju, C.; Kimy, K. H.; et al. High Mobility in a Stable Transparent Perovskite Oxide. Appl. Phys. Express 2012, 5,061102.

[109] Zhang, K. H. L.; Du, Y.; Papadogianni, A.; Bierwagen, O.; Sallis, S.; Piper, L. F. J.; Bowden, M. E.; Shutthanandan, V.; Sushko, P. V.; Chambers, S. a. Perovskite Sr-Doped $LaCrO_3$ as a New p-Type Transparent Conducting Oxide. Adv. Mater. 2015, 27, 5191−5195.

[110] Huang, W.; Nechache, R.; Li, S.; Chaker, M.; Rosei, F. Electrical and Optical Properties of Transparent Conducting p -Type $SrTiO_3$ Thin Films. J. Am. Ceram. Soc. 2016, 99, 226−233.

[111] Kuhar, K.; Crovetto, A.; Pandey, M.; Thygesen, K. S.; Seger, B.; Vesborg, P. C. K.; Hansen, O.; Chorkendorff, I.; Jacobsen, K. W. Sulfide Perovskites for Solar Energy Conversion Applications: Computational Screening and Synthesis of the Selected Compound $LaYS_3$. Energy Environ. Sci. 2017, 10, 2579−2593.

[112] Androulakis, J.; Peter, S. C.; Li, H.; Malliakas, C. D.; Peters, J. A.; Liu, Z.; Wessels, B. W.; Song, J.; Jin, H.; Freeman, A. J.; et al. Dimensional Reduction : A Design Tool for New Radiation Detection Materials; 2011; pp 4163−4167.

[113] Shi, H.; Saparov, B.; Singh, D. J.; Sefat, A. S.; Du, M.-H. Ternary Chalcogenides $Cs_2Zn_3Se_4$ and $Cs_2Zn_3Te_4$: Potential p-Type Transparent Conducting Materials. Phys. Rev. B: Condens. Matter Mater. Phys. 2014, 90, 184104.

[114] Johnsen, S.; Peter, S. C.; Nguyen, S. L.; Song, J.; Jin, H.; Freeman, A. J.; Kanatzidis, M. G. $Tl_2Hg_3Q_4$ (Q = S, Se, and Te): High-Density Wide-Band-Gap Semiconductors. Chem. Mater. 2011, 23, 4375−4383.

[115] Kehoe, A. B.; Temple, D. J.; Watson, G. W.; Scanlon, D. O. Cu_3MCh_3 (M = Sb, Bi; Ch = S, Se) as Candidate Solar Cell Absorbers: Insights from Theory. Phys. Chem. Chem. Phys. 2013, 15, 15477.

[116] Wang, M. X.; Yue, G. H.; Fan, X. Y.; Yan, P. X. Properties and Characterization of Cu_3SbS_3 Nanowires Synthesized by Solvothermal Route. J. Cryst. Growth 2008, 310, 3062−3066.

[117] Liu, M. L.; Huang, F. Q.; Chen, L. D. P-Type Transparent Conductivity of Cu1-XAlS2 (x = 0∼0.08). Key Eng. Mater. 2008, 368−372, 666−668.

[118] Banguero, E.; Gordillo, G. Related Content $CuAlS_2$ Thin-Films Prepared by Sulfurization of Metallic Precursors and Their Properties. Jpn. J. Appl. Phys. 2004, 31, L1396.

[119] Huang, F.; Liu, M.; Yang, C. Highly Enhanced P-Type Electrical Conduction in Wide Band Gap. Sol. Energy Mater. Sol. Cells 2011, 95, 2924−2927.

[120] Liu, M.; Wang, Y.; Huang, F. Optical and Electrical Properties Study on P-Type Conducting $CuAlS_{2+x}$ with Wide Band Gap. Scr. Mater. 2007, 57, 1133−1136.

[121] Liu, M.-L.; Huang, F.-Q.; Chen, L.-D.; Wang, Y.-M.; Wang, Y.-H.; Li, G.-F.; Zhang, Q. P -Type Transparent Conductor : Zn-Doped $CuAlS_2$. Appl. Phys. Lett. 2007, 90, 072109.

[122] Liu, M.-L.; Huang, F.-Q.; Chen, L.-D. P-Type Electrical Conduction and Wide Optical Band Gap in Mg Doped $CuAlS_2$. Scr. Mater. 2008, 58, 1002−1005.

[123] Reddy, Y. B. K.; Raja, V. S. Effect of Cu/Al Ratio on the Properties of $CuAlSe_2$ Thin Films Prepared by Co-Evaporation. Mater. Chem. Phys. 2006, 100, 152−157.

[124] Jin, M.; Min, S.; Mei-zhen, G.; Yue-gang, C.; Yan-hua, W.;Ramanujam, J.; Singh, U. P.; Rubel, O.; Darbandi, A. Related Content Preparation and Properties of Single Crystal $CuAlSe_2$ Film. Jpn. J. Appl. Phys. 1991, 30, L1238.

[125] Gombia, E.; Leccabue, F.; Pelosi, C. The CVD Growth of $CuAlTe_2$ Single Crystals. Mater. Lett. 1984, 2, 429−431.

[126] Yu, P. W.; Downing, D. L.; Park, Y. S. Electrical Properties of $CuGaS_2$ Single Crystals. J. Appl. Phys. 1974, 45, 5283−5288.

[127] Jeong, W.; Park, G. Structural and Electrical Properties of $CuGaS_2$ Thin Films by Electron Beam Evaporation. Sol. Energy Mater. Sol. Cells 2003, 75, 93−100.

[128] Prabukanthan, P.; Dhanasekaran, R. Growth of CuGaS2 Single Crystals by Chemical Vapor Transport and Characterization. Cryst. Growth Des. 2007, 7, 618−623.

[129] Ho, C.; Pan, C. Optical Behavior and Structural Property of $CuAlS_2$ and $AgAlS_2$ Wide-Bandgap Chalcopyrites. Appl. Opt. 2014, 53, E7−13.

[130] Hussien, B. H. Study of Some Structural and Optical Properties of $AgAlSe_2$ Thin Films. Ibn AL- Haitham Journal For Pure and Applied Science 2016, 29, 41−51.

[131] Uruno, A.; Usui, A.; Kobayashi, M. Structural and Optical Properties of $AgAlTe_2$ Layers Grown on Sapphire Substrates by Closed Space Sublimation Method. J. Appl. Phys. 2014, 116, 183504.

[132] Karaagac, H.; Parlak, M. The Investigation of Structural, Electrical, and Optical Properties of Thermal Evaporated AgGaS2 Thin Films. Thin Solid Films 2011, 519, 2055−2061.

[133] Krishnapriyan, A.; Barton, P. T.; Miao, M.; Seshadri, R. First-Principles Study of Band Alignments in the p-Type Hosts $BaM_2 \times 2$ (M = Cu, Ag; X = S, Se). J. Phys.: Condens. Matter 2014, 26, 155802.

[134] Tate, J.; Newhouse, P. F.; Kykyneshi, R.; Hersh, P. A.; Kinney, J.; McIntyre, D. H.; Keszler, D. A. Chalcogen-Based Transparent Conductors. Thin Solid Films 2008, 516, 5795−5799.

[135] Hersh, P. A. Wide Band Gap Semiconductors and Insulators: Synthesis, Processing and Characterization; 2007.

[136] Chen, E. M.; Stoyko, S. S.; Aitken, J. A.; Poudeu, P. F. P. Tuning the Optical, Electronic and Thermal Properties of Cu_3NbS_4-XSe_x through Chemical Substitution. Inorg. Chem. Front. 2017, 4, 1493−1500. Oliviera.

[137] Lu, Y.-J.; Ibers, J. A. Synthesis and Characterization of Cu_3NbSe_4 and KCu_2TaSe_4. J. Solid State Chem. 1993, 107, 58−62.

[138] Marzik, J. V.; Hsieh, A. K.; Dwight, K.; Wold, A. Photoelectronic Properties of Cu_3PS_4 and Cu_3PS_3Se Single Crystals. J. Solid State Chem. 1983, 49, 43−50.

[139] Ma, Z.; Yi, Z.; Sun, J.; Wu, K. Electronic and Photo-catalytic Properties of Ag_3PC_4 (C= O, S, Se): A Systemic Hybrid DFT Study. J. Phys. Chem. C 2012, 116, 25074−25080.

[140] Hsu W, Sutter-Fella CM, Hettick M et al (2015) Electron selective TiO_2 contact for Cu(In,Ga)Se_2 solar cells. Sci Rep 5.

[141] Guo Q, Ford GM, Yang WC et al (2010) Fabrication of 7.2% efficient CZTSSe solar cells using CZTS nanocrystals. JACS 132:17384–17386.

[142] Delbos S (2012) Kesterite thin films for photovoltaics: a review. EPJ Photovolt 3:art. no. 35004.

[143] Song XB, Ji X, Li M, Lin WD, Luo X, Zhang H (2014) A review on development prospect of CZTS based thin film solar cells. Int J Photoenergy:art. no. 613173.

[145] Siebentritt S, Schorr S (2012) Kesterites a challenging material for solar cells. Prog Photovolt 20:512–519.

[146] C. Persson, R. Chen, H. Zhao, M. Kumar, and D. Huang, "Electronic structure and optical properties from first-principles modeling," in Copper Zinc Tin Sulphide-based Thin Film Solar Cells (K. Ito, ed.), John Wiley & Sons, 2015.

[147] Wu, P.; Christuk, A. E.; Ibers, J. A. New Quaternary Chalcogenides $BaLnMQ_3$ (Ln = Rare Earth or Sc; M = Cu, Ag; Q=S, Se): II. Structure and Property Variation vs Rare-Earth Element. J. Solid State Chem. 1994, 110, 337−344.

[148] Sikerina, N. V.; Andreev, O. V. Crystal Structures of $SrLnCuS_3$ (Ln= Gd, Lu). Russ. J. Inorg. Chem. 2007, 52, 581−584.

[149] Schevciw, O.; White, W. B. The Optical Absorption Edge of Rare Earth Sesquisulfides and Alkaline Earth - Rare Earth Sulfides. Mater. Res. Bull. 1983, 18, 1059−1068.

[150] Mitchell, K.; Haynes, C. L.; McFarland, A. D.; Van Duyne, R. P.; Ibers, J. A. Tuning of Optical Band Gaps: Syntheses, Structures, Magnetic Properties, and Optical Properties of $CsLnZnSe_3$ (Ln= Sm, Tb, Dy, Ho, Er, Tm, Yb, and Y). Inorg. Chem. 2002, 41, 1199−1204.

[151] Ueda, K.; Inoue, S.; Hirose, S.; Kawazoe, H.; Hosono, H. Transparent P-Type Semiconductor: LaCuOS Layered Oxysulfide. Appl. Phys. Lett. 2000, 77, 2701−2703.

[152] Ueda, K.; Hosono, H. Band Gap Engineering, Band Edge Emission, and p-Type Conductivity in Wide-Gap $LaCuOS_{1-x}Se_x$ Oxychalcogenides. J. Appl. Phys. 2002, 91, 4768−4770.

[153] Liu, M. L.; Wu, L. B.; Huang, F. Q.; Chen, L. D.; Ibers, J. A. Syntheses, Crystal and Electronic Structure, and Some Optical and Transport Properties of LnCuOTe (Ln= La, Ce, Nd). J. Solid State Chem. 2007, 180, 62−69.

[154] Yanagi, H.; Tate, J.; Park, S.; Park, C.-H.; Keszler, D. A. P-Type Conductivity in Wide-Band-Gap BaCuQF (Q= S, Se). Appl. Phys. Lett. 2003, 82, 2814−2816.

[155] Kykyneshi, R.; McIntyre, D. H.; Tate, J.; Park, C.-H.; Keszler, D. A. Electrical and Optical Properties of Epitaxial Transparent Conductive BaCuTeF Thin Films Deposited by Pulsed Laser Deposition. Solid State Sci. 2008, 10, 921−927.

[156] Hiramatsu, H.; Kamiya, T.; Tohei, T.; Ikenaga, E.; Mizoguchi, T.; Ikuhara, Y.; Kobayashi, K.; Hosono, H. Origins of Hole Doping and Relevant Optoelectronic Properties of Wide Gap P-Type Semiconductor, LaCuOSe. J. Am. Chem. Soc. 2010, 132, 15060−15067.

[157] Tennakone, K.; Wijayanayake, R. H. Semiconducting Properties of Silver Thiocyanate. J. Phys. D: Appl. Phys. 1983, 16, L79.

[158] Hirose, H.; Ueda, K.; Kawazoe, H.; Hosono, H. Electronic Structure of $Sr_2Cu_2ZnO_2S_2$ Layered Oxysulfide with CuS Layers. Chem. Mater. 2002, 14, 1037−1041.

[159] Ueda, K.; Hirose, S.; Kawazoe, H.; Hosono, H. Electrical and Optical Properties of Layered Oxysulfides with CuS Layers: Sr− Cu− M− O− S System (M= Zn, Ga, In). Chem. Mater. 2001, 13, 1880−1883.

[160] Liu, M.-L.; Wu, L.-B.; Huang, F.-Q.; Chen, L.-D.; Chen, I.-W. A Promising P-Type Transparent Condcting Material: Layered Oxysulfide $[Cu_2S_2][Sr_3Sc_2O_5]$. J. Appl. Phys. 2007, 102, 116108.

[161] Pravin Kumar Singh and D. K. Dwivedi. Chalcogenide glass: Fabrication techniques, properties and applications ; 2017, VOL. 520, 256–27.

[162] National Renewable Energy Laboratory, Best Research-Cell Efficiencies. United States of America: National Renewable Energy Laboratory, 2021.

[163] F. I. Soitec, CEA-Leti, NewWorld Record for Solar Cell Efficiency at 46%. France: Soitec, CEA-Leti; Germany: Fraunhofer Institute for Solar Energy Systems, 2014.

[164] A. Slade and V. Garboushian in Technical Digest, 15th International Photovoltaic Science and Engineering Conference, Beijing, 2005.

[165] J. S.Ward, B. Egaas, R. Noufi,M. Contreras, K. Ramanathan, C. Osterwald, and K. Emery in Photovoltaic Specialist Conference (PVSC), 2014 40th IEEE, p. 2934, IEEE, 2014.

[166] M. A. Green, K. Emery, Y. Hishikawa, W. Warta, and E. D. Dunlop Progress in Photovoltaics: Research and Applications, vol. 24, p. 905, 2016.

[167] W.Wang, M. T.Winkler, O. Gunawan, T. Gokmen, T. K. Todorov, Y. Zhu, and D. B. Mitzi Advanced Energy Materials, vol. 4, p. 1301465, 2014.

[168] A. Kojima, K. Teshima, Y. Shirai, and T. Miyasaka Journal of the American Chemical Society, vol. 131, p. 6050, 2009.

[169] M. A. Green, A. Ho-Baillie, and H. J. Snaith Nature Photonics, vol. 8, p. 506, 2014.

[170] M. D. McGehee Nature Materials, vol. 13, p. 845, 2014.

[171] H. Hahn, G. Frank,W. Klingler, A.-D. Meyer, and G. Störger Zeitschrift für Anorganische und Allgemeine Chemie, vol. 271, p. 153, 1953.

[172] S. Wagner, J. L. Shay, P. Migliorato, and H. M. Kasper Applied Physics Letters, vol. 25, p. 434, 1974.

[173] Fujifilm Corp, High-durability Dye Improves E_ciency of Dye-sensitized Solar Cells. Japan: Fujifilm Corp, 2013.

[174] L. Kazmerski, F. White, and G. Morgan Applied Physics Letters, vol. 29, p. 268, 1976.

[175] J. S.Ward, B. Egaas, R. Noufi,M. Contreras, K. Ramanathan, C. Osterwald, and K. Emery in Photovoltaic Specialist Conference (PVSC), 2014 40th IEEE, p. 2934, IEEE, 2014.

[176] Y. Rodrıguez-Lazcano, M. Nair, and P. Nair Journal of Crystal Growth, vol. 223, p. 399,2001.

[177] M. Kumar and C. Persson Applied Physics Letters, vol. 102, p. 062109, 2013.

[178] A. B. Kehoe, D. J. Temple, G. W. Watson, and D. O. Scanlon Physical Chemistry Chemical Physics, vol. 15, p. 15477, 2013.

[179] V. Estrella, M. Nair, and P. Nair Semiconductor Science and Technology, vol. 18, p. 190,2003.

[180] J. T. Dufton, A. Walsh, P. M. Panchmatia, L. M. Peter, D. Colombara, and M. S. Islam Physical Chemistry Chemical Physics, vol. 14, p. 7229, 2012.

[181] A. W. Welch, L. L. Baranowski, P. Zawadzki, S. Lany, C. A. Wolden, and A. Zakutayev Applied Physics Express, vol. 8, p. 082301, 2015.

[182] P. Fernandes, P. Salomé, and A. Da Cunha Journal of Physics D: Applied Physics, vol. 43, p. 215403, 2010.

[183] D. M. Berg, R. Djemour, L. Gütay, S. Siebentritt, P. J. Dale, X. Fontane, V. Izquierdo-Roca, and A. Pérez-Rodriguez Applied Physics Letters, vol. 100, p. 192103, 2012.

[184] Y.-T. Zhai, S. Chen, J.-H. Yang, H.-J. Xiang, X.-G. Gong, A. Walsh, J. Kang, and S.-H.Wei Physical Review B, vol. 84, p. 075213, 2011.

[185] A. Shigemi, T. Maeda, and T. Wada Physica Status Solidi (B), vol. 252, p. 1230, 2015.

[186] A. Aruga and Y. Okamoto Japanese Journal of Applied Physics, vol. 45, p. 4616, 2006.

[187] K. Toyonaga and H. Araki Physica Status Solidi (C), vol. 12, p. 753, 2015.

[188] M. Umehara, Y. Takeda, T. Motohiro, T. Sakai, H. Awano, and R. Maekawa Applied Physics Express, vol. 6, p. 045501, 2013.

[189] M. Nakashima, J. Fujimoto, T. Yamaguchi, and M. Izaki Applied Physics Express, vol. 8, p. 042303, 2015.

[190] A. Kanai, K. Toyonaga, K. Chino, H. Katagiri, and H. Araki Japanese Journal of Applied Physics, vol. 54, p. 08KC06, 2015.

[191] W. Septina, S. Ikeda, Y. Iga, T. Harada, and M. Matsumura Thin Solid Films, vol. 550, p. 700, 2014.

[192] A. W. Welch, L. L. Baranowski, P. Zawadzki, S. Lany, C. A. Wolden, and A. Zakutayev Applied Physics Express, vol. 8, p. 082301, 2015.

CHAPTER II

Theoretical methods and outline of the computations

Summary

In this part, we will briefly mention the most important concepts, theories, and methods used in calculating structural, optoelectronic, thermoelectric and thermodynamic properties. We will describe the main ideas of the Born-Oppenheimer, Hartree and Hartree-Fock molecular dynamics methods. In addition a detailed presentation of Density Functional Theory (DFT), seen as a method to obtain accurate properties, the Kohn-Sham equations and the approximations making it possible to estimate an exchange-correlation potential, namely those of the local density. (LDA) and those of the generalized gradient (GGA), the modified Becke and Johnson approximation (mBJ) and the Engel-Vosko approximation (EV-GGA). Thus, we present the augmented plane wave method (APW) and the linearized augmented plane wave method (FP-LAPW) and describe the Wien2k simulation code used for the study of our compounds.

1. Introduction

The techniques used in the study of the electronic structure of materials and the understanding of many characteristics constitute a basic tool, and each time these techniques have constant updates and improvements, especially with technological development, which depend mainly simulations using fast computing means, such as clusters and sophisticated computers. The advantage of these techniques is to save time and compensate for some costly experiments. In addition, some tests are very serious, such as experiments in the field of nuclear radiation and experiments on certain dangerous chemicals. Moreover, it gives the property to control theoretically and to fix certain factors when using simulators, which can be difficult experimentally. These techniques, and among them the ab-initio method, are based on the simplification of the study of a very complex system made up of a large number of atoms and electrons, interacting with each other (quantum interactions), difficult to solved by conventional methods.

2. The Schrödinger equation

The beginning of the study of systems that contain a large number of microscopic particles was in the year 1926 when the physicist Erwin Schrodinger [1], in the framework of quantum theory - proposed a partial differential equation known at the time as the Schrödinger equation. The solution to this equation allows describing the instantaneous quantum state of the system through its wave function, which includes all the information about the studied system [2,3]. The expression for the Schrödinger equation is given by the following mathematical relationship:

$$H\Psi\left(\vec{R}_{\mathrm{I}},\vec{r}_{\mathrm{i}}\right)=E\Psi\left(\vec{R}_{\mathrm{I}},\vec{r}_{\mathrm{i}}\right) \qquad \text{(II.1)}$$

Where:

$\boldsymbol{H}$: Nonrelativistic Hamiltonian operator associated with the sum of kinetic energy and the potential energy of the system.

$\boldsymbol{\Psi}$: The wave function relates to all particle coordinates.

$\boldsymbol{E}$ **:** Steady state energy.

The Hamiltonian system made up of nuclei and electrons includes the kinetic energy of electrons, nuclei and nuclei, as well as interaction energies (electron-electron, electron-nucleus and nucleus-nucleus), where the expression of the total Hamiltonian effect of the system is given by the following expression:

$$H = T_e + T_N + V_{ee} + V_{eN} + V_{NN} \qquad \text{(II.2)}$$

Where:

$T_e = \sum_i \frac{p_i^2}{2m_i} = \sum -\frac{\hbar^2}{2m}\left(\nabla^2{}_i\right)$ Electron kinetic energy term (mi the mass of the electron i).

$T_N = \sum_\alpha \frac{p_\alpha^2}{2M_\alpha} = \sum -\frac{\hbar^2}{2M}\left(\nabla^2{}_\alpha\right)$ Kinetic energy term of the nucleus (m_I the mass of the nucleus I).

$V_{ee} = \sum_{i,j\neq i} \frac{1}{4\pi\varepsilon_0}.\frac{1}{2}\left(\frac{e^2}{\left|\vec{r_\alpha} - \vec{r_j}\right|}\right)$ Term of the electron-electron interaction potential.

$V_{eN} = \frac{1}{4\pi\varepsilon_0}\sum_{i,\alpha} -\frac{e^2 Ze}{\left|\vec{r_i} - \overrightarrow{R_\alpha}\right|}$ Term of the electron-nucleus interaction potential.

$V_{NN} = \frac{1}{4\pi\varepsilon_0}.\frac{1}{2}\sum_{\alpha,\beta} -\frac{e^2 Z_\alpha Z_\beta}{\left|\overrightarrow{R_\alpha} - \overrightarrow{R_\beta}\right|}$ Term of the nucleus - nucleus interaction potential.

The two symbols *i, j* are coefficients for electrons, while the symbols α, β and coefficients for nuclei *mj*, *mi* represent electron masses and M_α are nuclei masses.

$\left|R_\alpha - R_\beta\right|$ The distance between the two nuclei α and β.

$\left|r_i - R_\alpha\right|$ The distance between the nucleus α and the electron *i*.

$\left|r_i - r_j\right|$ The distance between the two electrons *i* and *j*.

Solving the Schrödinger equation for a system composed of a large number of electrons and nuclei is not easy in practice, since it is not possible to obtain an exact solution but approximate solutions after introducing simplifications and approximations in order to obtain an approximate solution that is closer to the real solution.

3. Born-Oppenheimer approximation (Adiabatic)

The Born-Oppenheimer approximation [4], developed by scientists Max Born and Robert Oppenheimer in 1927, allowed the movement of nuclei and electrons to be separated. Because the nucleus, despite its movement, remains very close to equilibrium when compared to electrons, which move very quickly, it is possible to ignore the kinetic energy of nuclei in comparison to the kinetic energy of electrons and treat the nucleus-nucleus interaction energy as a constant quantity (Vnn = Constant) [8,9].

The application of the Born-Oppenheimer approximation to the Schrödinger equation enabled a significant progress to be made in solving the Schrödinger equation, where the most prominent results were as follows:

The total wave function of the system $\Psi\left(\vec{R}_{\mathrm{I}}{}^{0},\vec{r}_{\mathrm{i}}\right)$ is now written as a product between the electronic wave function $\Psi_e\left(\vec{R}_{\mathrm{I}}{}^{0},\vec{r}_{\mathrm{i}}\right)$ and the nuclear wave function $\Psi_n\left(\vec{R}_{\mathrm{I}}{}^{0}\right)$

$$\Psi\left(\vec{R}_{\mathrm{I}}{}^{0},\vec{r}_{\mathrm{i}}\right) = \Psi_n\left(\vec{R}_{\mathrm{I}}{}^{0}\right)\Psi_e\left(\vec{R}_{\mathrm{I}}{}^{0},\vec{r}_{\mathrm{i}}\right) \tag{II.3}$$

The motion of electrons can be separated from the motion of the nuclei, and thus write the Schrödinger equation after applying the Born-Oppenheimer simplification to the form:

$$\begin{cases}[T_e + V_{ee} + V_{en}]\Psi_e\left(\vec{R}_{\mathrm{I}}{}^{0},\vec{r}_{\mathrm{i}}\right) = E_e\left(\vec{R}_{\mathrm{I}}{}^{0}\right)\Psi_e\left(\vec{R}_{\mathrm{I}}{}^{0},\vec{r}_{\mathrm{i}}\right)\\ \left[T_n + V_{nn} + E_e\left(\vec{R}_{\mathrm{I}}{}^{0}\right)\right]\Psi_n\left(\vec{R}_{\mathrm{I}}{}^{0}\right) = E\Psi_n\left(\vec{R}_{\mathrm{I}}{}^{0}\right)\end{cases} \tag{II.4}$$

4. Hartree-Fock approximation

The Hartree-Fock approximation was proposed to modify and correct the defects of the Hartree approximation. The idea presented by Hartree in 1928 [5-8] is based on the principle of independent particles, considering that all electrons are the same and each electron moves independently of others and without interaction with other particles within an average field resulting from the influence of the rest Other particles and this is based on the approximation of independent particles [8,9]. During this approximation, the interactions between electrons were treated based on symmetric charges without

spinning any Columbian repulsion interactions with ignoring both the correlation and exchange terms, in addition to the fact that the wave function did not take into account the Pauli exception principle and is therefore not 'antisymmetric'.

One of the disadvantages of the Hartree approximation is that it did not take into account the electron spin and the Pauli Exception Principle. But the positive thing about this approximation is its simplification of the Schrödinger equation, where he moved from studying a large number of electrons to studying one electron, so that the total Hamiltonian *H* of the electrons is the sum of the hamiltonians of each hi electron, while the total wave function of the electronic system is represented by the product of the individual wave functions of each electron and in the latter is the total energy of the electronic system as the sum of the individual energies of the electrons [3,10]. The Hamiltonian equation for one electron, according to the Hartree approximation is given as follows:

$$H = \sum_i h_i \tag{II.5}$$

$$h_i = -\frac{\hbar^2}{2m_i}\Delta_i - \sum_I \frac{Z_I e^2}{\left|\vec{r_i} - \vec{R_I}^0\right|} + \frac{1}{2}\sum_j \frac{e^2}{|\vec{r_i} - \vec{r_j}|} \tag{II.6}$$

While the wave function of the electronic system, as well as the total energy of the system, are given by the following expressions:

$$\Psi_e = \prod_i \Psi_i \tag{II.7}$$

$$E_e = \sum_i \varepsilon_i \tag{II.8}$$

The most important modification introduced by the scientist Fock [3,8,10,11] in 1930 on the Hartree method was to replace the wave functions of the electron with a Slater determinant [12], which enabled him to take into account the limit of the exchange that had previously been neglected by Hartree, where the interaction between electrons takes taking into account the limit of the Columbic interaction between the negative charge of electrons [3,10] as well as the exchange, thus replacing the previous functions with anti-symmetric functions, and thus Fock worked to introduce the spin factor in his treatment of interactions between electrons and replace the wave function of the electronic system with a Slater determinant [12] expressed by the relationship:

$$\Psi_{HF}(\vec{r}_1, \vec{r}_2, \dots, \vec{r}_N) = \frac{1}{\sqrt{N_e!}} \begin{bmatrix} \psi_1(\vec{r}_1) & \psi_1(\vec{r}_2) & \cdots & \psi_1(\vec{r}_N) \\ \psi_2(\vec{r}_1) & \psi_2(\vec{r}_2) & \cdots & \psi_2(\vec{r}_N) \\ \vdots & \vdots & \ddots & \vdots \\ \psi_N(\vec{r}_1) & \psi_N(\vec{r}_2) & \cdots & \psi_N(\vec{r}_N) \end{bmatrix} \tag{II.9}$$

Where $\frac{1}{\sqrt{N_e!}}$ represents the regularization coefficient of the wave function.

Despite the good development that resulted from the use of the Hartree-Fock approximation in terms of results, this approximation remained unable to solve the problem of the correlation between electrons, which is a quantum verb in addition, but the Schrödinger equation remained difficult to solve, which made the studies that followed the work of Hartree-Fock search About a simpler and more accurate method in terms of results, which is the density function theory (DFT).

5. Density functional theory (DFT)

Density functional theory (DFT) is based on the idea of rewriting the Hamiltonian of the electron as a function of the electron density instead of using wave functions. This theory has undergone a great development by researchers with their theoretical work, including Dirac [13], Slater [14], Rothenburg and Kohn [15].

The first discovery of the DFT theory took place in 1927 in the work of Thomas and Fermi [16,17] where they created the main idea of expressing the total energy of an electronic system as a function of the electron density by considering the electronic system as a homogeneous and regular electron gas. The idea made by the two scientists, Thomas and Fermi, was realized by the continuous partition of the Brillouin region (without taking into account the correlations between the electrons) in order to reach parts where the electron density is constant in each partition.

The expressions of the density of a homogeneous electron gas and of its kinetic energy are given, respectively, by the two formulas:

$$\rho = \frac{1}{3\,\pi^2} E_f^{\frac{3}{2}} \left(\frac{2m_e}{h^2}\right)^{\frac{3}{2}} \tag{II.10}$$

$$E_c = \frac{3}{5}\left(\frac{h^2}{2m_e}\right)(3\,\pi^2)^{\frac{2}{3}}\,\rho^{\frac{5}{2}} \tag{II.11}$$

5.1. Formalism of Density Functionality Theory (DFT)

The basis of the density functional theory (DFT) is to write the total energy of a system containing several interacting electrons as a function of the electron density, i.e. the calculation of the energy of the system based on electron density instead of its wave function, where the electron density expression is given by the formula:

$$\rho(\vec{r}) = \sum_{i=1}^{N} |\psi_i(\vec{r}_2)|^2 \quad \text{(II.12)}$$

Density Functional Theory (DFT) is based on two main axes:

5.2 The Hohenberg-Kohn theorem

The first and second theories presented by Hohenberg and Kohn are considered the basis of the density functional theory [18-20], where he considered in the first theory the total energy of an electronic system present within an external potential $V(\overrightarrow{r})$ as a function of the electronic density so that it is possible to know all the properties of the system when determining Electron density.

$$E[\rho(\vec{r})] = F[\rho(\vec{r})] + \int V(\vec{r})\rho(\vec{r})dr^3 \quad \text{(II.13)}$$

Where $F[\rho(\vec{r})]$ is a comprehensive function of the electronic density of the system where it represents the contributions of kinetic energy and interactions between electrons [10,21] where it is given by the relationship:

$$F[\rho] = T[\rho] + U[\rho] \quad \text{(II.14)}$$

For the external universe generated by the effect of drugs, it is given by the relationship:

$$V_{ext}(\vec{r_i}) = -\sum_A \frac{Z_A}{r_{iA}} \quad \text{(II.15)}$$

Where Z_A is the charge of the nucleus, r_{iA} is the distance between nucleus A and electron i.

While in the **second theory**, he explained the condition of obtaining the total energy of the basic state of the electronic system by finding the corresponding electronic density that makes the density function at its minimum value.

$$E(\rho_0(\vec{r})) \leq E[\rho(\vec{r})] \quad \text{(II.16)}$$

$$E(\rho_0) = MinE(\rho) \lim_{\rho \to N} \langle \Psi | \hat{T} + \sum_i V_{ext} + V_{ee} | \Psi \rangle \quad \text{(II.17)}$$

To obtain the electronic density corresponding to the basic case, we apply the principle of covariance [22], which expresses the differential of the total energy in terms of the electronic

density, which is given by the mathematical relationship in terms of both the universal function $F[\rho(\vec{r})]$ and the external potential V(r) [10]:

$$\frac{dF\,[\rho(r)]}{d\rho(r)} + V(r) = 0 \qquad \text{(II.18)}$$

5.3 Kohn-Sham equations

Treating an electronic system of electrons in motion and interacting with each other is difficult to solve mathematically because describing both kinetic energy and electron-electron interactions in terms of electron density is not an easy task.

The beginning of solving this problem in 1965 was based on ideas presented by the two scientists Kohen and Sham [13], which was to replace the real electronic system with an imaginary one in which the behavior of an electron is independent, unconnected and not interacting with other electrons, but is affected only by an effective potential (the Kohn-Sham potential). Which includes the external potential resulting from the effect of the nuclei in addition to the potential resulting from the effect of the rest of the electrons on this electron [10]:

$$T_R = T_f + T_c \qquad \text{(II.19)}$$

$$T_c = \langle \Psi | T | \Psi \rangle - \langle \varphi | T_s | \varphi \rangle \qquad \text{(II.20)}$$

As for the interaction V_{ee} between electrons in the real system, it was written in the following relationship [10]:

$$\langle \Psi | V_{ee} | \Psi \rangle = U_H + U_x + U_c \qquad \text{(II.21)}$$

Where the terms represent:

U_H : The Columbic repulsion energy between negatively charged electrons, or the so-called (Hartree potential).

U_x : Exchange energy between electrons having the same spin.

U_C : The binding energy between electrons.

The Kohn-Sham equation for the electronic system is given in terms of the kinetic energy of the electron: external potential energy, Hartree interaction and exchange-correlation energy, where the terms represent:

$T_s[\rho]$: The kinetic energy of an electron in an imaginary system.

$$T_s[\rho] = \left\langle \varphi_i \middle| -\frac{\hbar^2}{2\mathrm{m}} \Delta \middle| \varphi_i \right\rangle = -\frac{\hbar^2}{2\mathrm{m}} \sum_{\mathrm{i}} \int \varphi_i \nabla^2 \varphi_i{}^* dr_i \quad \text{(II.22)}$$

$V_{NE}[\rho]$: External potential generated by the nucleation effect (nuclear-electron interaction).

$$V_{NE}[\rho] = -\int \sum_{I,i} \frac{Z_I \rho(\vec{r})}{\left|\vec{R}_{\mathrm{I}}^{\,0} - \vec{r}\right|} dr \quad \text{(II.23)}$$

$U_H[\rho]$: Hartree reaction (Columbian reaction between electrons).

$$\mathrm{U}[\rho] = \frac{1}{2} \int \frac{\rho(\vec{r}) \rho\left(\vec{r'}\right)}{\left|\vec{r} - \vec{r'}\right|} dr dr' \quad \text{(II.24)}$$

$\mathrm{E_{xc}}[\rho]$: Exchange-correlation energy, which is the sum of the terms of correlation and exchange, and this energy is not an accurate mathematical statement, but is estimated by approximations.

$$\mathrm{E_{xc}}[\rho] = \mathrm{E_x}[\rho] + \mathrm{E_c}[\rho] \quad \text{(II.25)}$$

Thus, the Kohn-Sham equation is written as [21–23]:

$$H_{KS} \varphi_i(\vec{r}) = [T_s[\rho] + V_{KS}(\vec{r})] \varphi_i(\vec{r}) = \varepsilon^{KS} \varphi_i(\vec{r}) \quad \text{(II.26)}$$

$$V_{KS}(\vec{r}) = V_{ext}(\vec{r}) + V_H(\vec{r}) + + V_{XC}(\vec{r}) \quad \text{(II.27)}$$

$$E[\rho] = T_s[\rho] + V_{NE}[\rho] + U_H[\rho] + \mathrm{E_{xc}}[\rho] \quad \text{(II.28)}$$

5.4 Solving the Kohn-Sham equation

The solution to the Kuhn-Sham equation requires finding the analytic or estimation expressions for all the terms of the Kuhn-Sham effective potential $V_{KS}(\vec{r})$ especially the correlation exchange potential $E_{xc}[\rho]$ since this term has no mathematical formula but is estimated by known approximations, in addition to finding the functions The waveform that represents solutions to the Kohn-Sham equation, which is given by the relationship [10]:

$$\varphi_{KS}(\vec{r}) = \sum_j C_{ij} \varphi_j(\vec{r}) \quad \text{(II.29)}$$

Where C_{ij} is the diffusion coefficients of the wave function and φ_j is the wave functions.

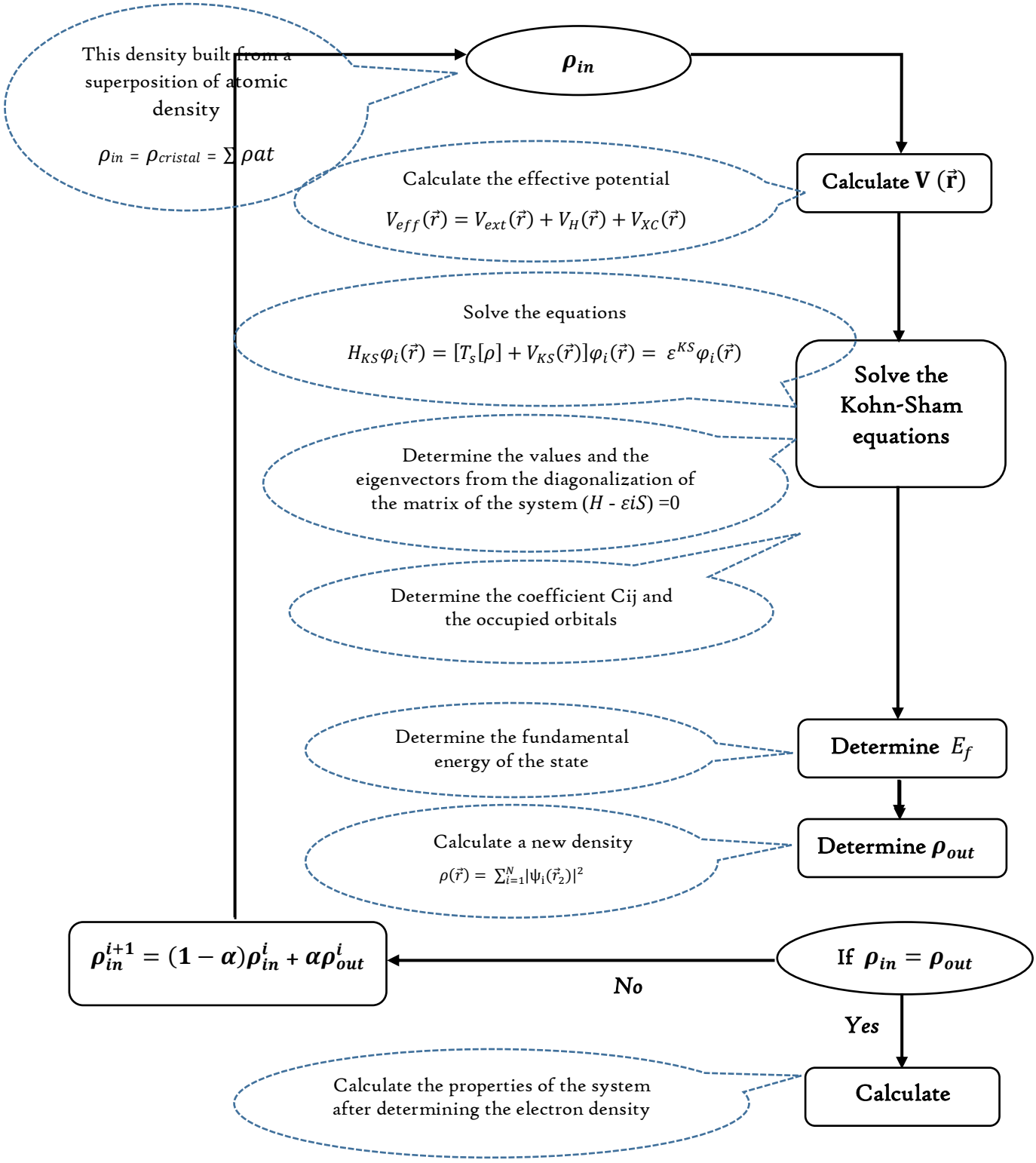

Figure II.1. Histogram for solving the Kohn-Sham equation in the framework of the density functional theory.

After simplifying these two relations and substituting into the Kohn-Sham equation, we get:

$$\sum_j C_{ij} H_{KS}|\varphi_j\rangle = \sum_j C_{ij}\varepsilon_{KS}|\varphi_j\rangle \quad \text{(II.30)}$$

$$\langle\varphi_k|\sum_j C_{ij} H_{KS}|\varphi_j\rangle = \langle\varphi_k|\sum_j C_{ij}\varepsilon_{KS}|\varphi_j\rangle \quad \text{(II.31)}$$

$$\sum_j \left(\langle\varphi_k|H_{KS}|\varphi_j\rangle - \varepsilon_{KS}\langle\varphi_k|\varphi_j\rangle\right)C_{ij} = 0 \quad \text{(II.32)}$$

Thus, the Kohn-Sham equation is solved by finding the coefficients C_{ij}.

The Kohn-Sham equation is solved according to iterative loops subject to the conditions of convergence shown in Figure (1.I), where the iterative loop starts from an initial density ρ_{in} and then the computer completes the first iterative loop by implementing it for algorithms and this is to solve the Kohn-Sham equation and then the new density ρ_{out} is calculated. After that, a test is conducted for the convergence condition, if the condition is met, the calculation stops, but if the convergence condition is not met, we will repeat the loop again after mixing the two electronic densities for two successive phases ρ_{in} and ρ_{out}.

6. Exchange-Correlation Functional

Because the exact form of the exchange-correlation potential is unknown today, it is the most difficult part of solving the Kohn-Sham equation. As a result, there approximate it, such as the local density approximation (LDA) [23-27], generalized gradient approximation (GGA) [28–31], and hybrid functional approach, such as HSE06 [32, 33].

6.1 The local density approximation (LDA)

The local density approximation is based on the theory of homogeneous electron gas, which forms a system of N electrons subjected to a positive external potential. As a result, the ground state electron density is homogeneous and constant.

In 1965, Kohn and Sham used the exchange-correlation energy of homogeneous electron gas ε_{XC}^{homo} to express the energy-correlation exchange functionality for a non-homogeneous system. The exchange-correlation functionality is of the form [34]:

$$E_{XC}^{LDA}[\rho] = \int \rho(\vec{r})\varepsilon_{XC}^{LDA}[\rho]d\,\vec{r} \quad \text{(II.33)}$$

We derive this functional with respect to ρ us find:

$$V_{xc} = \frac{dE_{XC}^{LDA}[\rho]}{\mathrm{d}\rho} = \varepsilon_{XC}^{LDA} + \rho(\vec{r})\frac{d\,\varepsilon_{XC}^{LDA}}{\mathrm{d}\rho} \quad \text{(II.34)}$$

Where ($\varepsilon_{XC}^{LDA}[\rho]$ is the exchange-correlation energy density per electron in a homogeneous electron gas).

We can separate the function $\varepsilon_{XC}^{LDA}[\rho]$ into two terms (exchange term and correlation term) as follows:

$$\varepsilon_{XC}^{LDA}[\rho] = \varepsilon_{X}^{LDA}[\rho] + \varepsilon_{C}^{LDA}[\rho] \tag{II.35}$$

The exchange term is known and given by the expression of Dirac [16] in the form:

$$\varepsilon_{X}[\rho] = -\frac{3}{4}\left(\frac{3}{\pi}\rho(\vec{r})\right)^{\frac{1}{3}} \tag{II.36}$$

Determining the correlation energy $\varepsilon_{X}[\rho]$ is not easy.

6.2 The local spin density approximation (LSDA)

This approximation was introduced to compensate for our lack of knowledge of the analytical mathematical expression of the cross-correlation energy between electrons. The widely used approximation is the positional spin density approximation (LSDA), which was proposed by two scientists, Kohn-Sham in 1964 [35], for the expression cross-correlation energy as well as the corresponding potential in terms of electronic density as follows:

$$E_{XC}^{LSDA} = \int \rho(\vec{r})\, E_{xc}\,[\rho(\vec{r})] d\vec{r} \tag{II.37}$$

$$V_{xc} = \frac{dE_{XC}^{LDA}[\rho]}{\mathrm{d}\rho} = \varepsilon_{XC}^{LDA} + \rho(\vec{r})\frac{d\,\varepsilon_{XC}^{LDA}}{\mathrm{d}\rho} \tag{II.38}$$

When taking into account the case of spin, whether up or down, the total electronic density is equal to the sum of the two electron densities $\rho(\vec{r}) = \rho_{\uparrow}(\vec{r}) + \rho_{\downarrow}(\vec{r})$ and we have two equations to solve the Cohn-Sham equation according to each spin state [10]:

$$\text{(II.39)} \begin{cases} \left(-\frac{\hbar^2}{2\mathrm{m}}\nabla^2 + \mathrm{V}_{\mathrm{eff}}^{\uparrow}(\vec{r})\right)\varphi_i(\vec{r}) = \varepsilon_{\mathrm{KS}}^{\uparrow}\varphi_i(\vec{r}) \\ \left(-\frac{\hbar^2}{2\mathrm{m}}\nabla^2 + \mathrm{V}_{\mathrm{eff}}^{\downarrow}(\vec{r})\right)\varphi_i(\vec{r}) = \varepsilon_{\mathrm{KS}}^{\downarrow}\varphi_i(\vec{r}) \end{cases}$$

While the effective latency is given, its expression is given as follows [10]:

$$(\text{II.40})\begin{cases} V_{eff}^{\uparrow}(\vec{r}) = V_{ext} + V_{xc}^{\uparrow} = V_{ext} + \frac{d\varepsilon_{XC}^{LSDA}[\rho_{\uparrow}(\vec{r}),\rho_{\downarrow}(\vec{r})]}{d\rho_{\uparrow}(\vec{r})} \\ V_{eff}^{\downarrow}(\vec{r}) = V_{ext} + V_{xc}^{\downarrow} = V_{ext} + \frac{d\varepsilon_{XC}^{LSDA}[\rho_{\uparrow}(\vec{r}),\rho_{\downarrow}(\vec{r})]}{d\rho_{\downarrow}(\vec{r})} \end{cases}$$

6.3 Generalized gradient approximation (GGA)

One disadvantage of the previous approximation is that it assumes the electron density is uniformly distributed, which is incorrect, especially in magnetic materials, because electron interactions take both the charge and the spin state into account. The new approximation differed from the first method in that the local electronic density was considered heterogeneous, and the total energy function of the electronic system was considered to be related to the electronic density and gradient as well, and thus the functional GGA energy depends only on the density and its gradient at a given point and is written as: [36]

$$E_{xc}^{GGA} = \int dr^3\, e_{xc}^{GGA}\,[\rho(r), \nabla, \rho(r)] \qquad (\text{II.41})$$

6.4 Engel & Vosko generalized gradient approximation (EV-GGA)

Although the LDA and GGA approximations give good results for structural properties, both approximations failed in the computation of the energy gaps in solids and the deviations obtained from the band structure calculations in the density approximation. Local (LDA) are about 40% compared to experimental results [37]. This deficiency is due to the fact that GGA and LDA used a simple function in the processing of correlation exchange potential. In this case, it is necessary to think of other formulas for the exchange-correlation energy by adding a new correction to the level of the GGA and LDA approximations that can produce good results, at least for the electronic properties.

Engel and Vosko [38] showed that the GGA does not significantly improve the given exchange potential because in the GGA approximation, we used the lowest order of correction in the gradient, using the potential of optimized model one can calculate the exact exchange potential of atoms and they also show that the precision for the exchange energies is mainly due to its excellent reproduction of the atomic exchange energies, which is mainly due to the elimination of errors local. To correct this shortcoming, Engel and Vosko modify the correction made to the correlation term, by mixing the second order of the generalized gradient with the exact Hartree-Fock correlation term; finally, they obtain a new form of correlation exchange potential treatment. EV-GGA that makes it possible to predict energy gaps close to experimental results.

6.5 Modified Becke and Johnson approximation (mBJ)

Since the LDA and the GGA cannot estimate the energy gap of comparable value to that obtained experimentally, Becke and Johnson (BJ) have developed a new form of exchange potential [39], which improves the energy gap with respect to the LDA functions and GGA, It can be formulated as follows:

$$V_{x,\sigma}^{BJ}(r) = V_{x,\sigma}^{BR}(r) + \frac{1}{\pi}\sqrt{\frac{5}{6}}\sqrt{\frac{t_\sigma(r)}{\rho_\sigma(r)}} \quad \text{(II.42)}$$

Where $\rho_\sigma(r)$ denotes the electron density and $t_\sigma(r)$ represents the kinetic energy density, the index σ is the spin notation.

Blaha et al [40] modified the exchange and correlation potential of the Becke and Johnson (BJ) approach and developed the mBJ potential capable of better reproducing the experimental deviation of semiconductors from LDA or GGA. The mBJ potential is given by:

$$V_{x,\sigma}^{mBJ}(r) = cV_{x,\sigma}^{BR}(r) + (3c-2)\frac{1}{\pi}\sqrt{\frac{5}{12}}\sqrt{\frac{2t_\sigma(r)}{\rho_\sigma(r)}} \quad \text{(II.43)}$$

Where:

$\rho_\sigma(r) = \sum_{i=1}^{n_e}\left|\psi_{i,\sigma}(r)\right|^2$ Is the electron density.

$t_\sigma(r) = \frac{1}{2}\sum_{i=1}^{n_e}\nabla\psi_{i,\sigma}^*(r)\nabla\psi_{i,\sigma}(r)$ Is the density of kinetic energy.

$V_{x,\sigma}^{BR}(r)$ Is the Becke-Roussel potential (BR) [41], which has been proposed to model the Coulomb potential:

$$V_{x,\sigma}^{BR}(r) = \left(-\frac{1}{b_\sigma(r)}(1 - e^{-x_\sigma(r)} - \frac{1}{2}x_\sigma(r)e^{-x_\sigma(r)}\right) \quad \text{(II.44)}$$

Where x_σ is determined from ρ_σ(r), $\nabla\rho_\sigma(r)$, $\nabla^2\rho_\sigma(r)$ and t_σ (r), $b_\sigma(r)$ is calculated using the following relation:

$$b_\sigma(r) = \left[\frac{X_\sigma^3\ (r)e^{-x_\sigma(r)}}{8\pi\rho_\sigma(r)}\right]^{\frac{1}{3}} \quad \text{(II.45)}$$

In the TB-mBJ, the value of c is calculated as follows:

$$c = \alpha + \beta\left[\left[\frac{1}{V_{cell}}\int_{cell}\frac{|\nabla\rho(r')|}{\rho(r')}d^3r'\right]\right] \quad \text{(II.46)}$$

Where V_{cell} is the unit cell volume, α and β are free parameters with values of -0.012 and 1.023 Bohr, respectively.

6.6 Hybrid functional approach (HSE06)

Another approximation method $E_{xc}[\rho]$ is to solve the exchange energy exactly within the Hartree-Fock approximation and then use an approximation for the correlation energy. The band gap energies produced by this exchange-energy method are typically too large. A combination of the exchange-energy method and the LDA or GGA may be preferred in some cases. This is the so-called hybrid functional approach [32, 33, 42, 43], in which the exchange energy is mixed to obtain better total energies and band gap energies empirically. The mixing can be done in a variety of ways. The following equation is defined in the HSE06 method.

$$E_{xc}^{HSE} = \alpha E_x^{SR}(\mu) + (1-\alpha)E_x^{PBE,SR}(\mu) + E_x^{PBE,LR}(\mu) + E_c^{PBE} \quad \text{(II.47)}$$

Perdew, Burke, and Ernzerhof (PBE) [31,32] merged the short-range (SR) element of the exact exchange E_x^{SR} with a short-range part of the GGA exchange $E_x^{PBE,SR}$. The usual Hartree-Fock mixing is 25% Hartree-Fock, or 0.25. Additionally, a PBE counterpart replaces the exchange energy's decaying long-ranged portion (LR) $E_x^{PBE,LR}(\mu)$. The range-separation parameters μ specify this, with 0.2 being the preferred value. The PBE approximation E_c^{PBE} provides the correlation component of the electron-electron interaction.

HSE06 and other hybrid functional are meant to produce superior overall energies (e.g., the error in lattice constants is often less than 12%) and band gap energies (the error bar is approximately 10%).

There are numerous exchange-correlation potentials available today [44–47]. It is still under construction. The Kohn-Sham equation has the advantage of being simple to implement additional potentials. However, because of the ease of implementation, various potentials exist, which can be viewed as inconsistency.

6.7 Other approximations

In 1951, Slater [48] proposed a formula to determine the exchange energy as a functional of the electron density ρ in the following form:

$$E_{X\alpha}[\rho] = -\frac{9}{4}\alpha\left(\frac{3}{4\pi}\right)\int \rho^{3/4}(\vec{r})\, d\,\vec{r} \quad \text{(II.48)}$$

Where α is an adjustable parameter which takes values between 0.7-0.8 [49] for most atoms but for a homogeneous gas it takes the exact value 1.5.

Another approximation of **Ceperley** and **Alder** [50] is that the exchange energy is considered the energy of Dirac:

$$\varepsilon_X[\rho] = -C_x\rho(\vec{r})^{\frac{1}{3}} \text{ tel que } C_x = -\frac{3}{4}\left(\frac{3}{\pi}\right)^{\frac{1}{3}} \tag{II.49}$$

We find the exchange potential:

$$V_X = -\frac{C_x}{3}\rho^{\frac{-2}{3}} \tag{II.50}$$

Perdew and Zunger parameterized the correlation energy $\varepsilon_c[\rho]$ by a Monte Carlo calculation. Thus by posing [51]:

$$r_s = \left(\frac{3}{4\pi\rho(\vec{r})}\right)^{\frac{1}{3}} \tag{II.51}$$

r_s: The inter-electronic separation parameter.

We can define according to the value of r_s, the relation of V_C as follows:

$$V_C = \begin{cases} 0.03\,ln(r_s) - 0.0583 + 0.0012\,r_s\,ln(r_s) - 0.084\,r_s & r_s < 1 \\ -0.01423\,\frac{1+1.2284\sqrt{r_s}+0.444r_s}{(1+1.0529\sqrt{r_s}+0.3334)^2} & r_s \geq 1 \end{cases} \tag{II.52}$$

In addition, **Hedin** and **Lundqvist** [52] formulate a more used approximation, to determine each term (exchange and correlation) separately. The exchange term is given by:

$$\varepsilon_X = \frac{-3\,e^2}{4\pi}(3\pi^2\rho)^{\frac{1}{3}} = \frac{-3\,e^2}{4\pi\alpha r_s} \tag{II.53}$$

Where: r_s: is the parameter of an electron gas verifying the condition.

$$\frac{3\pi}{4}(r_s a_B)^3 = \frac{1}{\rho} \tag{II.54}$$

Therefore, the term of the exchange potential is written in the form::

$$V_X(r_s) = \varepsilon_X(r_s) - \frac{r_s}{3}.\frac{d\varepsilon_X(r_s)}{dr_s} = \frac{3}{4}\varepsilon_X(r_s) \tag{II.55}$$

The correlation energy term expressed by **Hedin-Lundqvist** is given by:

$$\varepsilon_C(r_s) = -\frac{Ce^2}{2}\left[(1+x^2)\,log\left(1+\frac{1}{x}\right)+\frac{x}{2}-\mathrm{x}^2-\frac{1}{3}\right] \quad \text{(II.56)}$$

Where C=0.045 and $x = \frac{r_s}{21}$.

The term of the correlation potential is written as:

$$\mathrm{V_C(r_s)} = \varepsilon_C(\mathrm{r_s}) - \frac{\mathrm{r_s}}{3}.\frac{\mathrm{d}\varepsilon_C(\mathrm{r_s})}{\mathrm{dr_s}} = \frac{\mathrm{C\,e^2}}{2}\log\left(1+\frac{1}{\mathrm{x}}\right) \quad \text{(II.57)}$$

7. Flat wave method (APW)

The scientist Slater [12] relied on the Muffin-Tin approximation [54], where he divided the crystal space into two parts as shown in Figure I.2. In this approximation, the atoms were represented by non-overlapping spheres with radii *Ri*, in which the core electrons reside, in which the electrons are bound to the nucleus. Its atom is strong, and between these balls is an interfacial region that contains free electrons far from the nuclei of its atoms.

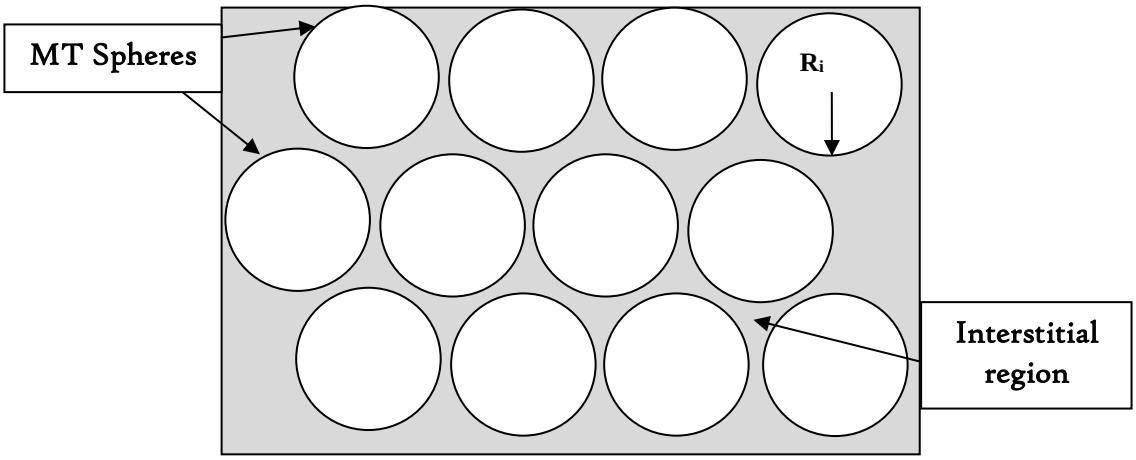

Figure II.2. Diagram of the distribution of the elementary cell in atomic spheres and interstitial region.

The latency to which the electrons inside the balls are subject is different from the latency to which the electrons in the space between the atoms are subject. According to Slater's approximation, the potential inside the spheres is symmetric, while the potential in the space region is constant, as according to the following two statements:

$$\mathrm{V}(\vec{\mathrm{r}}) = \begin{cases} \mathrm{V(r)} & \mathrm{r} \le \mathrm{R_0} \\ 0 & \mathrm{r} > \mathrm{R_0} \end{cases} \quad \text{(II.58)}$$

In addition, the waves that describe the behavior of electrons in the region inside the spheres differ from those in the steric region, where the wave functions in the two regions are different as the equation follows:

$$\varphi(\vec{r}) = \begin{cases} \sum_{l=0}^{\infty} \sum_{-m}^{m} A_{lm} U_l(r) Y_{lm}(r) & r \leq R_0 \\ \frac{1}{\sqrt{\Omega}} \sum_G C_G \, e^{i(\vec{K}+\vec{G})\vec{r}} & r > R_0 \end{cases} \quad \text{(II.59)}$$

Where radial functions $U_l(r)$ are regular solutions of the Schrödinger equation [55].

$$\left(-\frac{d^2}{dr^2} + \frac{l(l+1)}{r^2} V(\vec{r})\right) \mathrm{r} U_l = E_l U_l \quad \text{(II.60)}$$

Where: E_l: An energy parameter.

The radial functions defined by equation (III.4) are orthogonal to any proper state of the heart, but this orthogonally disappears in the boundaries of the spheres. As the following equation shows:

$$(E_1 - E_2) U_1 U_2 = U_2 \frac{d^2 r U_1}{d^2 r} - U_1 \frac{d^2 r U_2}{d^2 r} \quad \text{(II.61)}$$

U_1 , U_2: are the radial solutions for these energies E_1 et E_2respectively.

The coefficients A_{lm} are determined using the application of the wave function continuity condition in the vicinity of the point $r = R_0$, for this we develop the plane wave as a function of Bessel, then we do l 'equality between the external wave function of the MT sphere and that of the interior. Finally, we find:

$$A_{lm} = \frac{4\pi i^L}{\sqrt{\Omega} U(R_0)} \sum_G C_{k+G} J_l \left(\left|\vec{K} + \vec{G}\right| R_0\right) Y^*{}_{lm}(K+G) \quad \text{(II.62)}$$

Where: J_l: The Bessel function and $C_{k+G}$are the coefficients of the plane waves existing in the interstitial region.

Once the coefficients are calculated, we can define the base function given by the equation (II.59).

Unfortunately, the use of the APW method has its weak points because it is very slow and time consuming because the calculations are very complicated in the diagonalization of the Hamiltonian matrix of the secular equation. Because of the radial function U_l which is common, it is difficult to define the radial function for each energy value E_l, besides that, the basic function which is called the augmented plane wave is not a solution of the Schrödinger equation for the whole crystal because it is not linear. It is necessary to determine the wave function that satisfies the

Schrödinger equation, to overcome the problem we need to use a linear combination of the augmented plane waves.

8. The Linearized Augmented Plane Wave Method (LAPW)

To avoid the drawbacks of the first method, *Anderson* [56] introduced modifications on the APW method and deduced a new method called LAPW (Linearised Augmented Plane Wave). In the latter, Anderson writes the radial function U_l in Taylor expansion series in the neighborhood of the energy E_l as follows:

$$U_l(r,E) = U_l(r,E_l) + (E_l - E)\frac{dU_l(r,E)}{dE}\Big|_{E=E_l} + \mathcal{O}(E_l - E)^2 \quad \text{(II.63)}$$

$\mathcal{O}(E - E_l)^2$: Represents the squared error.

The potential inside "MT" atomic spheres is spherically symmetrical, but outside it is assumed constant, and can be expressed as:

$$V(r) = \begin{cases} \sum_{lm}^{m} V_{lm}(r) Y_{lm} & r \leq R_0 \\ \\ \sum_{lm}^{m} V_k(r) e^{ikr} & r > R_0 \end{cases} \quad \text{(II.64)}$$

In the LAPW method, the basic functions inside the muffin-tin sphere are a linear combination of the radial functions $U_l(\mathrm{r})Y_{lm}(r)$ and their derivatives $\dot{U}_l(r)Y_{lm}(r)$ with respect to l 'energy. As we have seen in the APW method, the wave functions in the two regions are given by:

$$\Phi_{\vec{K}+\vec{G}}(\vec{r}) = \begin{cases} \sum_{lm} \left(A_{lm} U_l(r) + B_{lm} \dot{U}_l(r)\right) Y_{lm}(r) & r \leq R_0 \\ \\ \frac{1}{\sqrt{\Omega}} \sum_G C_G \, e^{i(\vec{K}+\vec{G})\vec{r}} & r > R_0 \end{cases} \quad \text{(II.65)}$$

Such as:

$\vec{K}$: Represents the wave vector.

$\vec{G}$: The vector of the reciprocal network.

A_{lm}: Coefficients corresponding to the function U_l.

B_{lm}: Coefficients corresponding to the function $\dot{U}_l$.

Radial functions U_l and their derivatives $\dot{U}_l$ in MT spheres fulfill the normalization condition, which is written as follows:

$$\langle U_l|U_l\rangle = \int_0^{R_0} U_l^2\, r^2\, dr = 1 \tag{II.66}$$

$$\int_0^{r_0} r^2\, \dot{U}^2{}_l(r)dr = N \tag{II.67}$$

In addition, the radial functions U_l and their derivatives $\dot{U}_l$ are orthogonal, and we can write them in the form of orthogonality:

$$\int_0^{r_0} r^2\, U_l(r)\dot{U}_l(r)dr = 0 \tag{II.68}$$

In general, if U_l is equal to zero at the surface of the sphere, its derivative $\dot{U}_l$ will be different from zero. The radial functions U_l are defined as in the APW method and the functions $\dot{U}_l$ are the solutions of the following equation:

$$(-\frac{d^2}{dr^2} + \frac{l(l+1)}{r^2} V(\vec{r}) - E_l) r\dot{U}_l(r) = rU_l(r) \tag{II.69}$$

This equation results from the derivation of equation (II.60) with respect to energy.

Finally, it remains to determine the coefficients A_{lm} and B_{lm}, for each wave vector, and for each atom, for this, we apply the conditions of continuity of the basic functions in the vicinity of the limit of the spheres as we did in the APW method. After certain operations, we can define the coefficient formula A_{lm} and B_{lm} in the following forms:

$$A_{lm} = \frac{4\pi {r_0}^2 i^L}{\sqrt{\Omega}} Y^*{}_{lm}(K+G) a_l(K+G) \tag{II.70}$$

$$B_{lm} = \frac{4\pi {r_0}^2 i^L}{\sqrt{\Omega}} Y^*{}_{lm}(K+G) b_l(K+G) \tag{II.71}$$

$$a_l(K+G) = \left[\dot{U}_l\, \dot{j}'_l(K+G) - \dot{U}'_l\, j_l(K+G)\right] \tag{II.72}$$

$$b_l(K+G) = \left[\dot{U}'_l\, j_l(K+G) - \dot{U}_l\, \dot{j}'_l(K+G)\right] \tag{II.73}$$

Where $\dot{U}'$ and $\dot{j}'$ are the derivatives of $\dot{U}_l$ and j_l with respect to r.

Unlike the formalism of the standard APW method, in which the energy E_l is constant for this, the LAPW method is faster, since it makes it possible to choose different values of the parameter E_l depending on the value l of the angular momentum.

The LAPW functions form a good basis that allows, with a single E_l, to obtain all the valence bands in a large energy region. When this is not possible, the energy window can generally be divided into two parts, which is a great simplification compared to the APW method.

9. The Full-Potential Linearized Augmented Plane Wave Method (FP-LAPW)

The disadvantage that resulted from the application of the previous method lies in the slowness of the calculations, which made Anderson [57] make improvement changes to the APW method [58], so he used Taylor's publication to write the radial functions $U_l(r)$ as follows:

$$U_l(r,E) = U_l(r,E_l) + (E_l - E)\frac{dU_l(r,E)}{dE}\Big|_{E=E_l} + \mathcal{O}(E_l - E)^2 \qquad \text{(II.74)}$$

Then he got the phrase cumin in and out of Muffin-Tin balls as follows:

$$V(r) = \begin{cases} \sum_{lm}^{m} V_{lm}(r) Y_{lm} & r \leq R_0 \\ \\ \sum_{lm}^{m} V_k(r) e^{ikr} & r > R_0 \end{cases} \qquad \text{(II.75)}$$

As well as the wave functions inside the balls in terms of radial functions and their derivatives. Where the wave functions are written as [38, 39]:

$$\Phi_{\vec{K}+\vec{G}}(\vec{r}) = \begin{cases} \sum_{lm} \left(A_{lm} U_l(r) + B_{lm} \dot{U}_l(r) \right) Y_{lm}(r) & r \leq R_0 \\ \\ \frac{1}{\sqrt{\Omega}} \sum_G C_G \, e^{i(\vec{K}+\vec{G})\vec{r}} & r > R_0 \end{cases} \qquad \text{(II.76)}$$

Where $\vec{K}$ the wave ray, $\vec{G}$ the inverse lattice ray and the coefficients A_{lm} and B_{lm} are:

A_{lm} Coefficient related to radial functions

$$A_{lm} = \frac{4\pi {r_0}^2 i^L}{\sqrt{\Omega}} {Y^*}_{lm}(K+G) a_l(K+G) \qquad \text{(II.77)}$$

B_{lm} Coefficient related to the derivative of radial functions

$$B_{lm} = \frac{4\pi {r_0}^2 i^L}{\sqrt{\Omega}} {Y^*}_{lm}(K+G) b_l(K+G) \qquad \text{(II.78)}$$

The method of linearly incremented flat waves gave impressive results and later became one of the best methods adopted in the study of compounds, especially as it uses the full potential.

10. Choice of E_l and R_0

To avoid the risk of confusing semi-core states with valence states because of the no-orthogonally of some core states, the FP-LAPW method requires a good choice of E_l and therefore we are obliged to change the value E_l to every time.

Unfortunately, this solution is not available in all cases, so we take an appropriate radius of the sphere (when we take a small radius of the MT sphere, this choice is impracticable because it is not possible to describe an atom very close to the nucleus. Similarly, if we take a radius of the MT sphere large the wave function is not adequate to describe the region further to the nucleus). So to obtain precise calculations and good results from the electronic structure one is obliged to adjust the value R_0*G_{max} which is practically between 7 and 9 ($7 < R_0*G_{max} < 9$).

11. Constructions of radial functions

In the method (FP-LAPW), the base functions are radial functions inside the spheres, and in the interstitial region, they are plane waves. Thus, the construction of the basic functions consists in determining:

1- The radial functions $U_l(r)$ and their derivatives $\dot{U}_l(r)$.

2- The coefficients A_{lm} and B_{lm} which satisfy the boundary conditions.

The boundary conditions provide a simple means for the determination of the cut-off of the angular momentum l_{max} also for the representation of the cut-off G_{max} of plane waves in the MT sphere for a radius R_0. A reasonable strategy consists in choosing these cut-offs, such as $R_0*G_{max} = l_{max}$, which is achieved in practice since the convergence of the FP-LAPW calculations is ensured for R_0*G_{max} between 7 and 9.

12. Solving the Poisson equation

The potential used in the Kohn and Sham equation contains the correlation exchange potential and the Coulomb potential ($V_c = V_{Hartree} + V_N$). Solving the Poisson equation allows us to determine the Coulomb potential.

$$\nabla^2 V_C(\vec{r}) = 4\pi\rho(\vec{r}) \qquad \text{(II.79)}$$

The "pseudo-charge" method proposed by **Hamann** [59] and **Weinert** [60] solves the Poisson equation; it is essentially based on the following two observations:

1- The charge density is continuous and varies slowly in the interstitial regions; on the other hand, it varies rapidly in the core region.

2- The Coulomb potential in the interstitial region does not depend only on the charges in this region, but also on the charges in the core region.

The charge density is described by a Fourier series in the interstitial region as follows:

$$\rho(\vec{r}) = \sum_G \rho(\vec{G})\, e^{i\vec{G}\vec{r}} \tag{II.80}$$

The development of the **Bessel** function j_l allows calculating the plane waves $e^{i\vec{G}\vec{r}}$.

$$\int_0^R r^{l+2} J_l(\vec{G}\vec{r}) d\vec{r} = \begin{cases} R^{l+3} \frac{J_l(\vec{G}\vec{r})}{Gr} & G \neq 0 \\ \frac{R^3}{3}\sigma_{l,0} & G = 0 \end{cases} \tag{II.81}$$

Then:

$$e^{i\vec{G}\vec{r}} = 4\pi e^{i\vec{G}\vec{r}_\alpha} \sum_{lm} i^l J_l\left(|\vec{G}||\vec{r} - \vec{r}_\alpha| Y_{lm}^*(\vec{G}) Y_{lm}(\vec{r} - \vec{r}_\alpha)\right) \tag{II.82}$$

Where: r: Is the radial coordinate and r_α: Is the position of the sphere α.

The Coulomb potential becomes:

$$V_C(\vec{G}) = \frac{4\pi\rho(\vec{G})}{G^2} \tag{II.83}$$

By integrating equation (II.79) we find:

$$V_{PW} = \sum_{lm} V_{lm}^{PW}(r) Y_{lm}(r) = \sum_V V_V^{PW}(r) K_v(r) \tag{II.84}$$

Where: V_{PW}: The interstitial potential.

Let: $K_v(r) = \sum_m C_{lm} Y_{lm}(r)$, we can determine the potential inside the sphere (MT) by using **Green's** function.

$$V_V(r) = V_{lm}^{PW}(r)\left[\frac{r}{R}\right] + \frac{4\pi}{2l+1}\begin{Bmatrix} \frac{1}{r^{l+1}}\int_0^x d\,r' r'^{l+2}\rho_v(r') + r^l \int_x^R dr'\, r'^{l-1}\rho_v(r') \\ -\frac{r^l}{R^{2l+1}}\int_0^{R_x} dr' r'^{l+2}\,\rho_v(r') \end{Bmatrix} \tag{II.85}$$

Where: $\rho_v(r')$ are the radial parts of the charge density.

13. The LAPW + LO method

To overcome the disadvantage of processing semi-core electrons (low energy valence electrons) in the LAPW method, two windows are used energy and the resulting secular equations are solved separately. **Singh** [61] proposes the LAPW+LO method, it uses a third category of basic functions. These functions are denoted local orbitals (LO). These functions result from the linear combination of two radial functions corresponding to two different energies and the derivative with respect to the energy of one of these functions.

The proper function has the following form:

$$\phi(\vec{r}) = \sum_{lm}\left[A_{lm} U_l(r, E_{1,l}) + B_{lm}\dot{U}_l(r, E_{1,l}) + C_{lm} U_l(r, E_{2,l})\right] Y_{lm}(r) \quad r < R_0 \tag{II.86}$$

Where the coefficients C_{lm} are of the same nature as the coefficients A_{lm} and B_{lm} defined previously.

14. The APW + lo method

The problem with APW was related to its energy dependence. In LAPW+LO, this problem was solved by using an energy independent base at the cost of a larger base size. It is only natural to consider another, more efficient and unbiased method that includes the exciting features of APW and LAPW.

Sjostedt et al. [62] proposed an approach called APW+lo. In this method, the set of basic functions is independent and has the same size as the original APW system. This means that each radial wave function is evaluated at a fixed linearization energy to solve the nonlinear eigenvalue problem and using local (lo) orbitals for the physically important quantum numbers.

The following is the set of basic APW+lo functions made up of APW functions taken at a fixed energy E_l:

$$\phi(\vec{r}) = \begin{cases} \sum_{lm} A_{lm} U_l(r)\, Y_{lm}(r) & r < R_0 \\ \frac{1}{\sqrt{\Omega}} \sum_G C_G\, e^{i(\vec{K}+\vec{G})\vec{r}} & r > R_0 \end{cases} \quad \text{(II.87)}$$

With supplement, the functions are local orbitals (lo) different from those of the LAPW+LO method, defined by:

$$\phi(\vec{r}) = \begin{cases} \sum_{lm} \left[A_{lm} U_l(r, E_l) + B_{lm} \dot{U}_l(r, E_l)\right] Y_{lm}(r) & r < R_0 \\ 0 & r > R_0 \end{cases} \quad \text{(II.88)}$$

15. Account Program Explanation "Wien2k"

With technological development, especially programming languages, researchers at the Institute of Materials Chemistry in Vienna [63] were able to design the Wien2k program, which is considered one of the most important programs used in studying the properties of solid materials. This program consists of several embedded and arranged software written in FORTRAN, which are algorithms for equations of the crystal system processed according to density functional theory (DFT) that adopts the method of linearly increasing full-latency plane waves FP-LAPW as a method to calculate to algorithms in order to study the properties of compounds [10].

Originally, WIEN2k was developed at the Institute of Materials Chemistry at the Technical University of Vienna and published by Blaha P., Schwarz K., Sorintin P. and Trickey S. B [10] and

it is subject to several modifications and improvements such as WIEN93, WIEN95, WIEN97 and WIEN2K.

The most important software and its function in the various Wien2k programs are shown in the diagram in Figure 3. I, which is as follows [10]:

NN: This program calculates the distances between adjacent atoms, which helps to determine the appropriate atomic radius value, as it verifies that there is no interference between atoms.

SGROUP: The task of this program is to determine the group of the space group to which the compound belongs.

SUMMUTRY: This program calculates the number of symmetry operations for the space group of the compound.

LSTART: This program calculates the electronic density of free atoms and determines how to handle the different orbitals in the band structure calculations.

KGEN: Generates a network of K points in the irreducible part of the first Brillouin region.

DSTART: It calculates the initial density of the SCF cycle by fitting the atomic densities.

After the last subroutine; we enter a loop of SFC calculations and therefore we will go to the five steps:

LAPW0 (POTENTIEL): Uses the total electron density to calculate the Coulomb and exchange potential (Hartree-Fock potential). In addition to that, it divides the space into an MT sphere (muffin-tin) and an interstitial region.

LAPW1 (BANDES): Calculate the eigenvalues and wave functions for valence electrons from the solution of equation (I.1).

LAPW2 (RHO): Calculate the valence electron densities they get in step lapw0.

LCORE: Calculate the eigenvalues and wave functions to obtain the core electron densities.

MIXER: Calculate the new density by mixing.

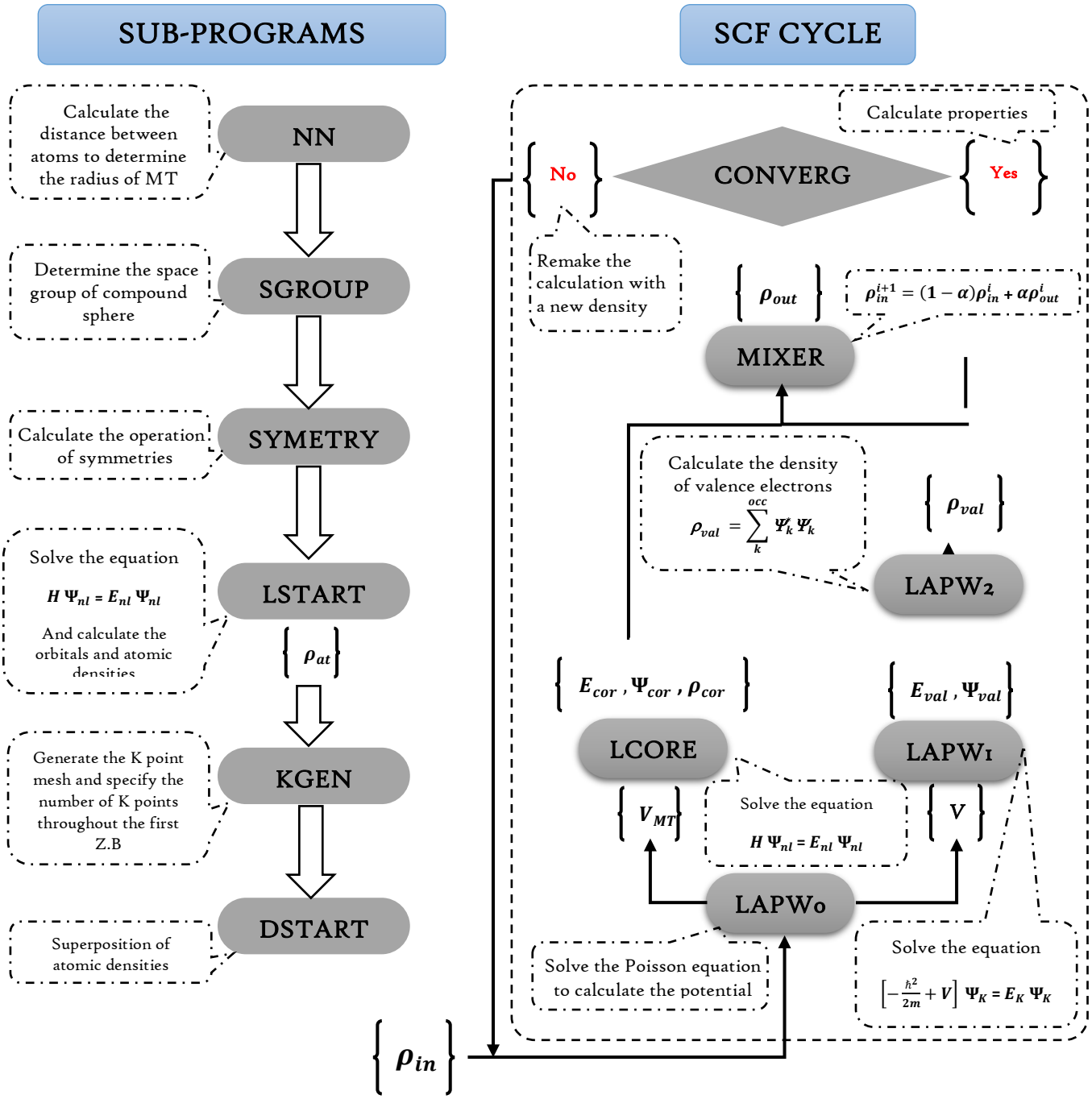

Figure II.3. The Wien2k code program flowchart.

In addition to other programs, this program accepts the integration of other programs on it, such as BoltzTraP [41] and xcrysden [64] and other programs.

16. The semi-classical model "Boltzman"

Boltzmann's theory [65] was used to calculate the conductivity properties of materials under the influence of an electric field E, magnetic B, or a thermal gradient ΔT to which the material is subjected. The electric current j can be written in terms of the conductivity effects according to the relationship:

$$J_i = \sigma_{ij} E_j + \sigma_{ijk} E_j B_k + v_{ij} \nabla_j T + \cdots \quad \text{(II.89)}$$

Through this Boltzmann model, it is possible to obtain expressions of the thermoelectric properties such as the electrical conductivity σ and the electronic thermal conductivity with the two relations:

$$(T,u) = \frac{1}{\Omega} \int \sigma_{\alpha\beta}(\varepsilon) \left[-\frac{\partial f_u(T,u)}{\partial \varepsilon} \right] d\varepsilon \quad \text{(II.90)}$$

$$k(T,u) = \frac{1}{e^2 T \Omega} \int \sigma_{\alpha\beta}(\varepsilon)(\varepsilon - u)^2 \left[-\frac{\partial f_u(T,u)}{\partial \varepsilon} \right] d\varepsilon \quad \text{(II.91)}$$

Where **f** is a Boltzmann distribution function, **u** is the chemical potential.

17. Calculation Program Boltztrap2

The program BOLTZTRAP2 [65] was designed using the Python programming language to calculate the transport coefficients for a free electron based on the semi-classical Boltzmann semi-classical model like abinit, Wien2k and others. This program has contributed to the development of research, especially with regard to the study of materials that have applications in the field of thermoelectricity.

This program enables the calculation of many properties and their changes in terms of both temperature and chemical potential. Among the properties that this program can calculate, we mention Seebeck coefficient, electronic conductivity, electronic thermal conductivity, electronic heat capacity and magnetic permittivity.

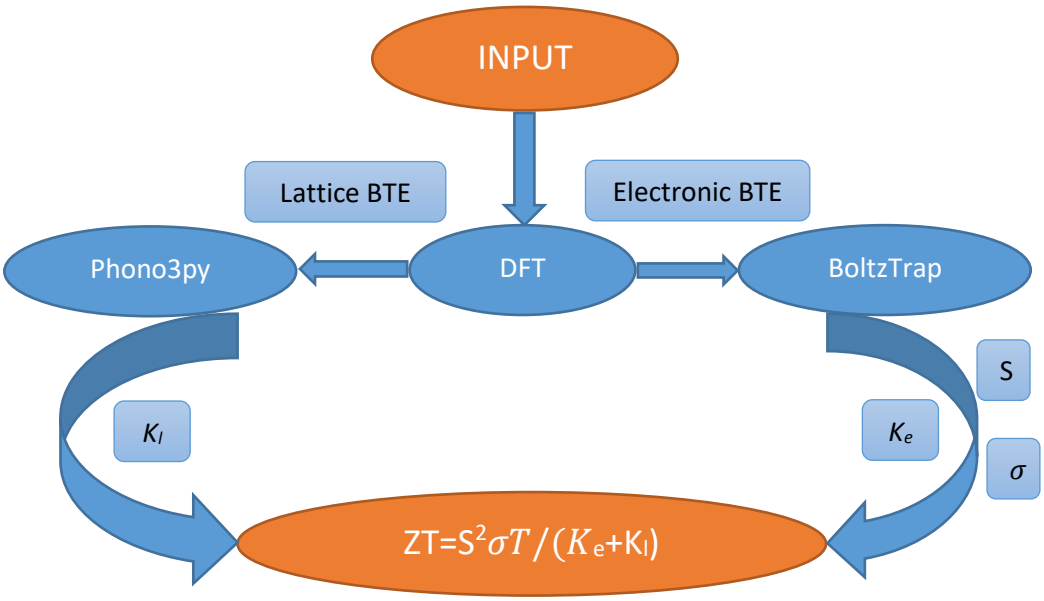

Figure II.4. The BoltzTrap code program flowchart.

18. Debye's quasi-harmonic model

The program used in calculating thermodynamic properties is GIBBS2 [66]. This program is based on the theoretical basis of Debye's model, its proposed by Peter Debye in 1912 in order to find an explanation and explanation for many phenomena thermal of solid materials such as heat capacity of solids and thermal expansion, where he considered that the movement of the atom by movement is affected by the vibration of other atoms and compensated for the vibration pulse previously introduced by Einstein through a spectrum of pulses:

$$g_{Debye}(\omega) = \begin{cases} \frac{9n\omega^2}{\omega_D^3} & si\ \omega < \omega_D \\ 0 & si\ \omega \geq \omega_D \end{cases} \qquad (II.92)$$

Therefore, the Gibbs function can be used to study a group of atoms vibrating under the influence of temperature so that this system is in a stable state when the derivative of the Gibbs function with respect to volume is at its minimum value.

$$\left(\frac{\partial G^*(V,P,T)}{\partial V}\right)_{P,T} = 0 \qquad (II.93)$$

Where the expression of the Gibbs function of an unstable oscillating system is given by the formula:

$$G^*(x,V;P,T) = E_{sta}(x,V) + PV + A^*_{vib}(x,V;T) + F^*_{el}(x,V;T) \qquad (II.94)$$

Where the functions $A^*_{vib}(x,V;T)$ and $F^*_{el}(x,V;T)$ are given by the two expressions:

$$A^*_{vib} = \int_0^{\infty} \left[\frac{\omega}{2} + k_B T \, Ln\,(1 - e^{-\frac{\omega}{k_B T}})\right] g(\omega) d\omega \quad \text{(II.95)}$$

$$F^*(x, V; T) = E_{sta}(x, V) + A^*_{vib}(x, V; T) \quad \text{(II.96)}$$

The use of the semi-hormonal model made it possible to explain several phenomena, and it also enabled the estimation of some heat parameters, such as:

- Entropy

$$S = -3nk_B \ln\left(1 - e^{-\Theta_D/T}\right) + 4nk_B D(\Theta_D/T) \quad \text{(II.97)}$$

- Heat capacity

$$C_v = 12nk_B D(\Theta_D/T) - \frac{9nk_B \Theta_D/T}{e^{\Theta_D/T} - 1} \quad \text{(II.98)}$$

- Coefficient of thermal expansion

$$\alpha = -\frac{1}{V}\left(\frac{\partial V}{\partial T}\right)_P = \frac{\gamma C_v}{V B_T} \quad \text{(II.99)}$$

19. wxAMPS-1D software

Numerical simulation has become essential for research on photovoltaic cells. Simulation software gives us the possibility of studying and interpreting the results obtained, in order to optimize the structure and the various components of the cells to improve their performance. Among the available software, our choice is focused on the wxAMPS-1D (Analysis for Microelectronic and Photonic Structures – One Dimension), mainly used for inorganic thin film solar cells. It was created and developed by Professor Stephen Fonash and his team of students John Arch, Joe Cuiffi, Jingya Hou, William Howland, Peter, and visiting researchers McElheny, Anthony Moquin, Michael Rogosky, Francisco Rubinelli, Thi Tran and Hong Zhu at Pennsylvania State University as part of support from the Electric Power Research Institute (EPRI) [67].

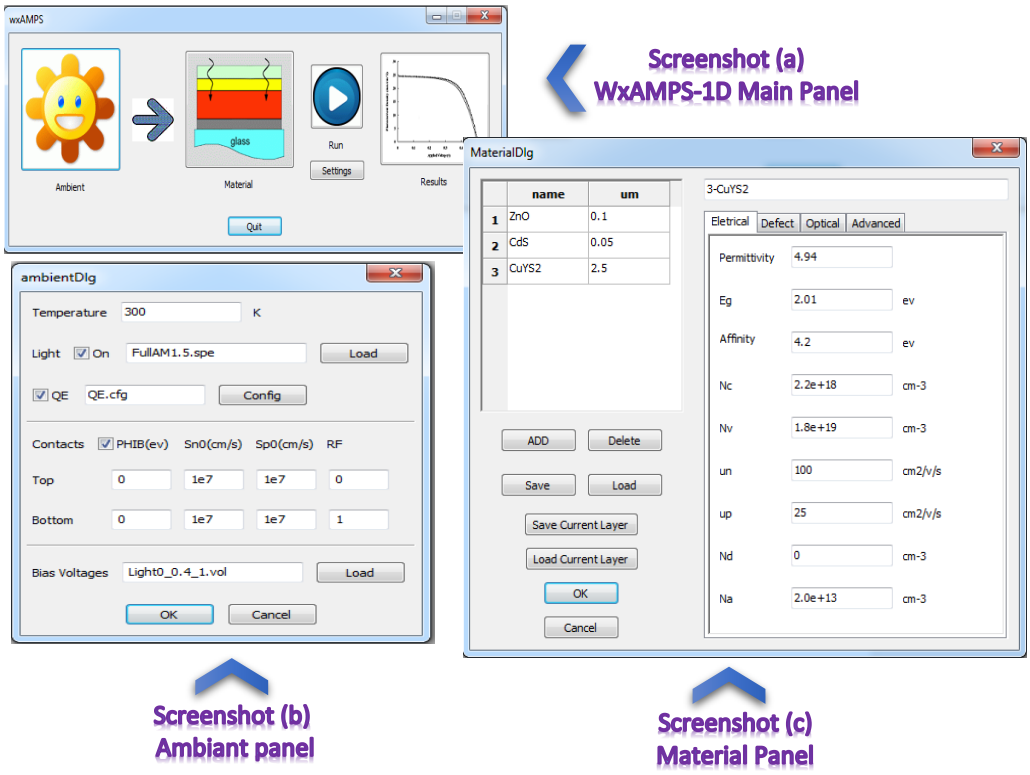

Figure II.5. wxAMPS-1D software main window.

The wxAMPS-1D interface (Figure II.5) consists of three dialog boxes. Each gives the necessary parameters before launching the simulation by the wxAMPS-1D. The three dialog boxes give:

- Environmental conditions.
- The material properties of each layer.
- Modeling parameters: model type, grid spacing for numerical calculations, bias voltages for which output (J-V) and (QE) should be generated [68]. The interface of the environmental conditions in the software of wxAMPS-1D (Represented in the Screenshot (b)). Therefore, to study the effect of temperature and/or lighting on the performance of the solar cell, they can be varied from the high right interface.

In the screenshot (c) we have represented the interface of the material properties of each layer such as the electrical properties (gap energy, mobility, affinity, doping, etc.), optical properties and defects. Therefore, after choosing the model of the solar cell that we want to simulate it, we can study the effect of the thickness and the doping of each layer on the parameters of the solar cell to obtain maximum efficiency from varying them in this interface.

The key element of the wxAMPS-1D software is the numerical resolution of the Poisson equation and the continuity equations taking into account the boundary conditions [69].

$$\frac{d}{dx}\left(-\varepsilon(x)\frac{d\Psi}{dx}\right) = q^*[p(x) - n(x) + N_D^+(x) - N_A^-(x) + p_t(x) - n_t(x)] \quad \text{(II.100)}$$

The equation (IV-1) is the one-dimensional form of the Poisson equation used by the wxAMPS-1D software.

Where Ψ is the electrostatic potential, *n* the concentration of free electrons, *p* the concentration of free holes, n_t the trapped electrons, p_t the trapped holes, N_D^+ concentrations of ionized donors, N_A^- concentration of ionized acceptors, ε represents the permittivity and q the elementary charge of the electron.

$$n = N_C F_{1/2} \exp\left(\frac{E_F - E_c}{kT}\right) \quad \text{(II.101)}$$

$$p = N_V F_{1/2} \exp\left(\frac{E_V - E_F}{kT}\right) \quad \text{(II.102)}$$

Equations II.101 and II.102 are the expressions for the concentration of free electrons and the concentration of free holes respectively at thermodynamic equilibrium, under voltage, under illumination or both. In these N_C and N_V are the effective densities of states of the conduction band and the valence band respectively and are described by the following equations:

$$N_C = 2\left(\frac{2\pi m_n^* kT}{h^2}\right)^{3/2} \quad \text{(II.103)}$$

$$N_V = 2\left(\frac{2\pi m_p^* kT}{h^2}\right)^{3/2} \quad \text{(II.104)}$$

Where the effective mass of electrons is m_n^*, m_p^* is the effective mass of holes and K is Boltzmann's constant and h is Planck's constant.

$$J_n(x) = q\mu_n n\left(\frac{dEf_n}{dx}\right) \quad \text{(II.105)}$$

$$J_p(x) = q\mu_p p\left(\frac{dEf_p}{dx}\right) \quad \text{(II.106)}$$

Equations II.105 and II.106 are respectively, the electron current density equation and the hole current density equation, where μ_n represents the mobility of electrons and μ_p represents the mobility of holes.

20. Conclusion

This chapter was devoted to the presentation of the density functional theory (DFT) and the linearized augmented plane wave method (FP-LAPW). Thus we have seen the basic approximations (the Born Oppenheimer and Hartree-Fock approximation) come to alleviate the Schrödinger equation. As already mentioned, the two important approximations, namely the local density approximation (LDA) and the generalized gradient approximation (GGA) are used by the DFT. The chapter ends with an illustration of the Wien2k, BoltzTrap and GIBBS2 codes that are installed in the Linux operating system, where the method (FP-LAPW) is implemented and finally a description of the wAMPS-1D software that is implemented for photovoltaic applications.

21. References

[1] E. SCHROEDINGER, Quantization as a Problem of Proper Values (Part I), Ann. Phys. (1926).

[2] S.S. Essaoud, M. Imadalou, D.E. Medjadi, Microscopic Study of Correlations in Finite Fermionic Systems by Breaking the Axial Symmetry, Int J Mod. Theo Phys. 5 (2016) 8–21.

[3] S. Saad Essaoud, Etude microscopique des corrélations dans les systèmes fermioniques finis en brisant la symétrie axiale, 2013.

[4] M. Born, R. Oppenheimer, Zur Quantentheorie der Molekeln, Ann. Phys. 389 (1927) 457–484.

[5] D.R. Hartree, The wave mechanics of an atom with a non-Coulomb central field. Part I. Theory and method, (1928).

[6] J.-M. Combes, P. Duclos, R. Seiler, The born-oppenheimer approximation, in: Rigorous Atomic and Molecular Physics, Springer, 1981: pp. 185–213.

[7] D.R. Hartree, The wave mechanics of an atom with a non-coulomb central field. Part II. Some results and discussion, in: Math. Proc. Camb. Philos. Soc., Cambridge University Press, 1928: pp. 111–132.

[8] R.G. Woolley, B.T. Sutcliffe, Molecular structure and the born-Oppenheimer approximation, Chemical Physics Letters. 45 (1977) 393–398.

[9] D.R. Hartree, The wave mechanics of an atom with a non-coulomb central field. Part iii. Term values and intensities in series in optical spectra, in: Math. Proc. Camb. Philos. Soc., Cambridge University Press, 1928: pp. 426–437.

[10] G. Shadmon, I. Kelson, Multi-determinantal hartree-fock theory, Nucl. Phys. A. 241 (1975) 407–428.

[11] J.F. Berger, Approches de champ moyen et au-delà, (1991).

[10] S. Saad Essaoud, Les composés à base de manganèse: investigation théorique des propriétés structurales électroniques et magnétiques, 2020.

[11] V. Fock, Selfconsistent field “mit Austausch für Natrium, Z. Für Phys. 62 (1930) 795–805.

[12] J.C. Slater, Damped Electron Waves in Crystals, Phys. Rev. 51 (1937) 840–846.

[13] W. Kohn, L.J. Sham, Self-consistent equations including exchange and correlation effects, Phys. Rev. 140 (1965) A1133.

[14] C. Fiolhais, F. Nogueira, M.A. Marques, A primer in density functional theory, Springer Science & Business Media, 2003.

[15] F.M. Bickelhaupt, E.J. Baerends, Kohn-Sham density functional theory: predicting and understanding chemistry, Rev. Comput. Chem. 15 (2000) 1–86.

[16] J.A. Pople, P.M. Gill, B.G. Johnson, Kohn—Sham density-functional theory within a finite basis set, Chem. Phys. Lett. 199 (1992) 557–560.

[17] W. Kohn, L.J. Sham, Self-Consistent Equations Including Exchange and Correlation Effects, Phys. Rev. 140 (1965) A1133–A1138.

[18] A. Görling, Density-functional theory beyond the Hohenberg-Kohn theorem, Phys. Rev. A. 59 (1999) 3359.

[19] T.L. Gilbert, Hohenberg-Kohn theorem for nonlocal external potentials, Phys. Rev. B. 12 (1975) 2111.

[20] J. Riess, W. Münch, The theorem of Hohenberg and Kohn for subdomains of a quantum system, Theor. Chim. Acta. 58 (1981) 295–300.

[21] R.M. Dreizler, E.K.U. Gross, Density Functional Theory, (1990).

[22] R.M. Dreizler, Providência, Density Functional Methods In Physics, (1985).

[23] R. M. Martin, Electronic Structure: Basic Theory and Practical Methods. Cambridge University Press, 2004.

[24] S. Cottenier, Density Functional Theory and the Family of (L)APW-methods: A Step-bystep Introduction, 2002-2013 (2nd edition), ISBN 978-90-807215-1-7, freely available at

[25] W. Kohn and L. J. Sham Physical Review, vol. 140, p. A1133, 1965.

[26] U. von Barth and L. Hedin Journal of Physics C: Solid State Physics, vol. 5, p. 1629, 1972.

[27] L. Hedin and B. Lundqvist Journal of Physics C: Solid State Physics, vol. 4, p. 2064, 1971.

[28] J. P. Perdew and K. Burke International Journal of Quantum Chemistry, vol. 57, p. 309, 1996.

[29] A. D. Becke Physical Review A, vol. 38, p. 3098, 1988.

[30] J. P. Perdew and Y. Wang Physical Review B, vol. 45, p. 13244, 1992.

[31] J. P. Perdew, K. Burke, and M. Ernzerhof Physical Review Letters, vol. 77, p. 3865, 1996.

[32] A. V. Krukau, O. A. Vydrov, A. F. Izmaylov, and G. E. Scuseria The Journal of Chemical Physics, vol. 125, p. 224106, 2006.

[33] J. Heyd and G. E. Scuseria ., The Journal of Chemical Physics, vol. 121, p. 1187, 2004.

[34] Kohn, W., Sham, L.J., Self-Consistent Equations Including Exchange and Correlation Effects, Phys. Rev. 140 4A (1965) A1133.

[35] Dirac, P.A.M., Note on Exchange Phenomena in the Thomas Atom, Math. Proc. Camb. Philos. Soc. 26 3 (1930) 376.

[36] D.M. Ceperley, B.J. Alder, Ground State of the Electron Gas by a Stochastic Method, Physical Review Letters. 45 (1980) 566–569.

[37] Perdew, J.P., Density functional theory and the band gap problem, Int. J. Quantum Chem. 28 S19 (1985) 497.

[38] D.R. Hamann, Semiconductor Charge Densities with Hard-Core and Soft-Core Pseudopotentials, Phys. Rev. Lett. 42 (1979) 662–665.

[39] M. Weinert, Solution of Poisson's equation: Beyond Ewald-type methods, J. Math. Phys. 22 (1981) 2433–2439.

[40] Fabien Tran, Peter Blaha And Karlheinz Schwarz, Band gap calculations with Becke-Johnson exchange potential, J. Phys. Condens. Matter 19 19 (2007) 196208.

[41] G.K.H. Madsen, P. Novák, Charge order in magnetite. An LDA+ U study, EPL Europhys. Lett. 69 (2005) 777.

[42] J. Heyd, G. E. Scuseria, and M. Ernzerhof The Journal of Chemical Physics, vol. 118,p. 8207, 2003.

[43] J. Heyd, G. E. Scuseria, and M. Ernzerhof The Journal of Chemical Physics, vol. 124,p. 219906, 2006.

[44] D. J. Tozer and N. C. Handy The Journal of Chemical Physics, vol. 108, p. 2545, 1998.

[45] F. A. Hamprecht, A. J. Cohen, D. J. Tozer, and N. C. Handy The Journal of Chemical Physics, vol. 109, p. 6264, 1998.

[46] T. Grabo and E. K. Gross Chemical Physics Letters, vol. 240, p. 141, 1995.

[47] A. J. Cohen, P. Mori-Sánchez, and W. Yang The Journal of Chemical Physics, vol. 126, p. 191109, 2007.

[48] Slater, J.C., A Simplification of the Hartree-Fock Method, Phys. Rev. 813 (1951) 385.

[49] Gáspár, R., The Hellmann-Feynman theorem and the correlation energy, Acta Phys. Acad. Sci. Hung. 162 (1963) 169.

[50] Ceperley, D.M., Alder, B.J., Ground State of the Electron Gas by a Stochastic Method, Phys. Rev. Lett. 45 7 (1980) 566.

[51] Perdew, J.P., Zunger, A., Self-interaction correction to density-functional approximations for many-electron systems, Phys. Rev. B 23 10 (1981) 5048.

[52] Hedin, L., Lundqvist, B.I., Explicit local exchange-correlation potentials, J. Phys. C Solid State Phys. 4 14 (1971) 2064.

[53] O.K. Andersen, T. Saha-Dasgupta, Muffin-tin orbitals of arbitrary order, Phys. Rev. B. 62 (2000) R16219.

[54] D D Koelling and G O Arbman, Use of energy derivative of the radial solution in an augmented plane wave method: application to copper, J. Phys. F Met. Phys. 5 (1975) 2041.

[55] Andersen, O.K., Linear methods in band theory, Phys. Rev. B 12 8 (1975) 3060.

[56] O.K. Andersen, Linear methods in band theory, Phys. Rev. B. 12 (1975) 3060–3083.

[57] M. Petersen, F. Wagner, L. Hufnagel, M. Scheffler, P. Blaha, K. Schwarz, Improving the efficiency of FP-LAPW calculations, Comput. Phys. Commun. 126 (2000) 294–309.

[58] Hamann, D.R., Semiconductor Charge Densities with Hard-Core and Soft-Core Pseudopotentials, Phys. Rev. Lett. 42 10 (1979) 662.

[59] Weinert, M., Solution of Poisson's equation: Beyond Ewald-type methods, J. Math. Phys. 22 11 (1981) 2433.

[60] Singh, D., Krakauer, H., H-point phonon in molybdenum: Superlinearized augmentedplane-wave calculations, Phys. Rev. B 43 2 (1991) 1441.

[61] Sjöstedt, E., Nordström, L., Singh, D.J., An alternative way of linearizing the augmented plane-wave method, Solid State Commun. 114 1 (2000) 15.

[62] P. Blaha, K. Schwarz, G. Madsen, D. Kvasnicka, J. Luitz, Wien2k, (2001).

[63] A. Kokalj, XCrySDen—a new program for displaying crystalline structures and electron densities, J. Mol. Graph. Model. 17 (1999) 176–179.

[65] G.K. Madsen, D.J. Singh, BoltzTraP. A code for calculating band-structure dependent quantities, Comput. Phys. Commun. 175 (2006) 67–71.

[64] A. Otero-de-la-Roza, D. Abbasi-Pérez, V. Luaña, Gibbs2: A new version of the quasiharmonic model code. II. Models for solid-state thermodynamics, features and implementation, Comput. Phys. Commun. 182 (2011) 2232–2248.

[65] A. Otero-de-la-Roza, V. Luaña, Gibbs2: A new version of the quasi-harmonic model code. I. Robust treatment of the static data, Comput. Phys. Commun. 182 (2011) 1708–1720.

[66] P. Debye, Einige Bemerkungen zur Magnetisierung bei tiefer Temperatur, Ann. Phys. 386 (1926) 1154–1160.

[67] Liu Y, Sun Y, Rockett A. A new simulation software of solar cells–*wx*AMPS. Sol Energ Mater Sol C. 2012;98: 124.

[68] Yiming Liu , Daniel Heinzel, Angus Rockett : «A REVISED VERSION OF THE AMPS SIMULATION CODE», Bourses d'Etat, Université de Nankai, à Tianjin, Chine et l'Université de l'Illinois, Urbana, Etats-Unis.

[69] Omer BM, Pivrikas A, Mohamed AK. AMPS-1D modeling of P3HT/PCBM bulk heterojunction solar cell. 37th IEEE Conference Photovoltaic Specialists Conference, Seattle (Washington) USA, 2011, 2: 734.

CHAPTER III

Results and Discussions

Summary

The aim of this chapter is to provide a detailed of our computational study of the structural and optoelectronic properties of $CuYX_2$ ternary compounds (X = S, Se and Te), within the TB-mBJ approximation. Then we revealed the results of thermodynamic studies and phase stability and that the structure of chalcogenide is the preferred phase for these materials at zero temperature and pressure. Finally, we presented some principles about the thermoelectric properties before presenting all the results obtained in this work. We also compared all obtained results with other results of experimental and theoretical studies available in previously published works.

1. Introduction

The current state of materials research chalcogenide (Ch = S, Se, Te) semiconductors has been examined in this chapter, suggesting that this is a key area for continuing and future study. Therefore, we have studied and calculated the linear structural, electronic, optical, thermodynamic and thermoelectric properties at equilibrium of the ternary compounds chalcogenides $CuYZ_2$ (Z= S, Se and Te).

2. Simulation details

In this work, the WIEN2k code[1] is used to predict the structural, optoelectronic, thermodynamic and thermoelectric properties of $CuYS_2$, $CuYSe_2$, and $CuYTe_2$ using the Full Potential-Linearized Augmented Plane Wave (FP-LAPW) approach based on density functional theory (DFT).

For structural properties, we used both Perdew and Wang's local density approximation (LDA)[2] and the revised Perdew-Burke-Ernzerhof (PBESol) parameterization of the generalized gradient approximation (GGA)[3], whereas for optoelectronic properties, we used the modified Becke-Johnson exchange potential (TB-mBJ)[4].

The initialization is presented under a series of programs which generate input files in order to define a starting density, for the determination of the potential and thus the resolution of the Schrödinger equation which gives the eigenvalues and the functions clean. As a result, a new density is generated from the calculated eigenfunctions. This cycle is repeated until convergence is reached.

Before embarking on long and expensive calculations, it is necessary to optimize the input parameters that control the initial calculation density. In general, there are two adjustments to be made:

1- The size of the base of plane waves by the choice of the cutoff Ec (Cutoff Energy) which allows a correct approximation of the eigenfunctions.

2- The quality of the sampling of the Brillouin zone (by the number of kpoints).

The unit cell is separated into muffin-tin spheres that do not overlap and an interstitial area. Wave functions are enlarged in terms of plane waves in the interstitial area, with a cut-off of RMT*KMAX = 8, where RMT is the minimum muffin-tin radius and KMAX is the amplitude of the maximum K vector wave in the Brillouin zone. The optimal value of the cut-off parameter

RMT*Kmax was chosen with the help of a convergence test where we calculated the total energy of the crystalline for different values of RMT*kmax (between 5 and 9.5), then we plotted the curve of the variation of total energy as a function of RMT*kmax, and we observed that The convergence condition is satisfied from the value of RMT*Kmax = 8 (The difference between the two values of the total energy for both states of RMT*Kmax = 8 and 8.5 is less than the value of the convergence condition).

Whereas, a spherical harmonic expansion has used inside the spheres with an angular momentum up to $l_{max} = 10$. The chosen values of the muffin-tin radius R_{MT} for Cu, Y, S, Se and Te atoms are 2.15, 2.4, 1.75, 2.35 and 2.4 (a.u) respectively. For the Brillouin zone (BZ) integration, **162** special k-points have been used for $CuYS_2$ and **100** special k-points have been used for both $CuYSe_2$ and $CuYTe_2$ in the irreducible wedge, the electronic configurations for valence electrons are for Cu ($3d^{10}$ $4s^1$), Y ($4d^1$ $5s^2$), S($3s^2$ $3p^4$) Se ($3d^{10}$ $4s^2$ $4p^4$) and Te ($4d^{10}$ $5s^2$ $5p^4$).To separate between the valence and core states -6 eV was used as separating energy. Both energy (10^{-5} Ry) and charge (10^{-3} e) values were used as criteria for convergence during the calculation.

To appear pressure and temperature effects on different thermal properties, we employed the quasi-harmonic model implemented in the GIBBS2 code [5,6]. To estimate the thermoelectric properties, we have used the semi-local Boltzmann transport theory implemented in BoltzTraP code[7].

3. Structural properties

Ternary chalcogenides with copper-based can be crystallized in several types of structures, which directly affect many properties, especially electronic and optical. For this reason, we studied $CuYS_2$ compound in orthorhombic phase structure with *Pnma* space group (62) and $CuYSe_2$, $CuYTe_2$ in hexagonal phase with *P-3m1* space group (164).

The choice of these symmetry groups was done based on the experimental work done $CuYS_2$ [8], $CuYSe_2$ [9] and $CuYTe_2$ [10].

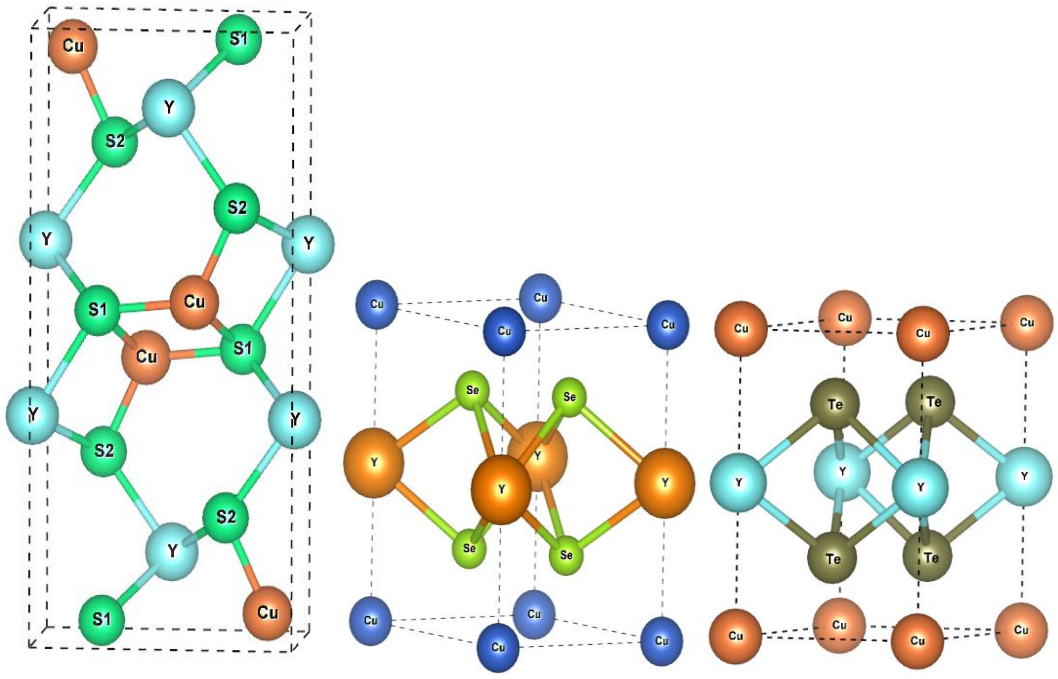

Figure. III.1. Crystal structure of: (a) $CuYS_2$ (orthorhombic), (b) $CuYSe_2$ and (c) $CuYTe_2$.

Before calculating lattice constants, bulk modulus and the cohesive energy, we should determine the atoms positions formed these compounds, through full geometry optimizations, the internal atomic positions are relaxed by using the total energy and force minimization scheme basing on Broyden's method [11,12] in which a good relaxed structure can be achieved if the force applied to each atom was smaller than 0.5 Ry/au.

The optimized positions of the atoms for each compound by using GGA and LDA approximations are presented in Table.1 and compared to other experimental or theoretical results.

Table. III.1. Calculated atomic positions using GGA and LDA approximations of $CuYZ_2$ (Z= S, Se and Te) compounds.

		GGA			LDA			Other works		
Materials	**Atoms**	**x**	**y**	**z**	**x**	**y**	**z**	**x**	**y**	**z**
	Cu	0.4561	0.2500	0.3758	0.4589	0.2500	0.3768	0.4465	0.2500	0.3919[8]
$CuYS_2$	Y	0.1335	0.2500	0.5016	0.1336	0.2500	0.5013	0.1348	0.2500	0.4925[8]
(Pnma # 62)	S	0.4602	0.2500	0.7534	0.4621	0.2500	0.7514	0.4623	0.2500	0.7597[8]
	S	0.2965	0.2500	0.2418	0.3002	0.2500	0.2440	0.2934	0.2500	0.2310[8]
	Cu	0.0000	0.0000	0.0000	0.0000	0.0000	0.0000	-	-	-
$CuYSe_2$	Y	0.0000	0.0000	0.5000	0.0000	0.0000	0.5000	-	-	-
(P-3m1 # 164)	Se	0.3333	0.6666	0.2323	0.3333	0.6666	0.2325	-	-	-
	Se	0.6666	0.3333	0.7676	0.6666	0.3333	0.7675	-	-	-
	Cu	0.0000	0.0000	0.0000	0.0000	0.0000	0.0000	-	-	-
$CuYTe_2$	Y	0.0000	0.0000	0.5000	0.0000	0.0000	0.5000	-	-	-
(P-3m1 # 164)	Te	0.3333	0.6666	0.2245	0.3333	0.6666	0.2246	-	-	-
	Te	0.6666	0.3333	0.7754	0.6666	0.3333	0.7753	-	-	-

Computing the lattice parameter "a" of each unit cell is performed by calculating the total energy at different volumes, and then, we use the Murnaghan equation of state [13] to determine the equilibrium volume that correspond to the lowest energy (see Fig.2).

$$E(V) = E_0 + \frac{B}{B'(B'-1)}\left[V\left(\frac{V_0}{V}\right)^{B'} - V_0\right] + \frac{B}{B'}(V - V_0) \qquad \text{(III.1)}$$

Where E_0, V_0, B *and* B' are respectively: the total energy, the volume at equilibrium, and the compressibility modulus and its derivative.

The compressibility modulus is given by:

$$B = -V\frac{\partial P}{\partial V} = V\frac{\partial^2 E}{\partial V^2} \qquad \text{(III.2)}$$

The volume at equilibrium is given by the minimum of the curve E (V).

Thereafter, the total energy for different values of c/a ratio for the hexagonal as well as c/a and then b/a for the orthorhombic structure at a fixed volume is computed to measure the lattice

constant "c" for both $CuYSe_2$ and $CuYTe_2$ in the hexagonal phase, as well as "b" and "c" constants in the orthorhombic phase for $CuYS_2$.

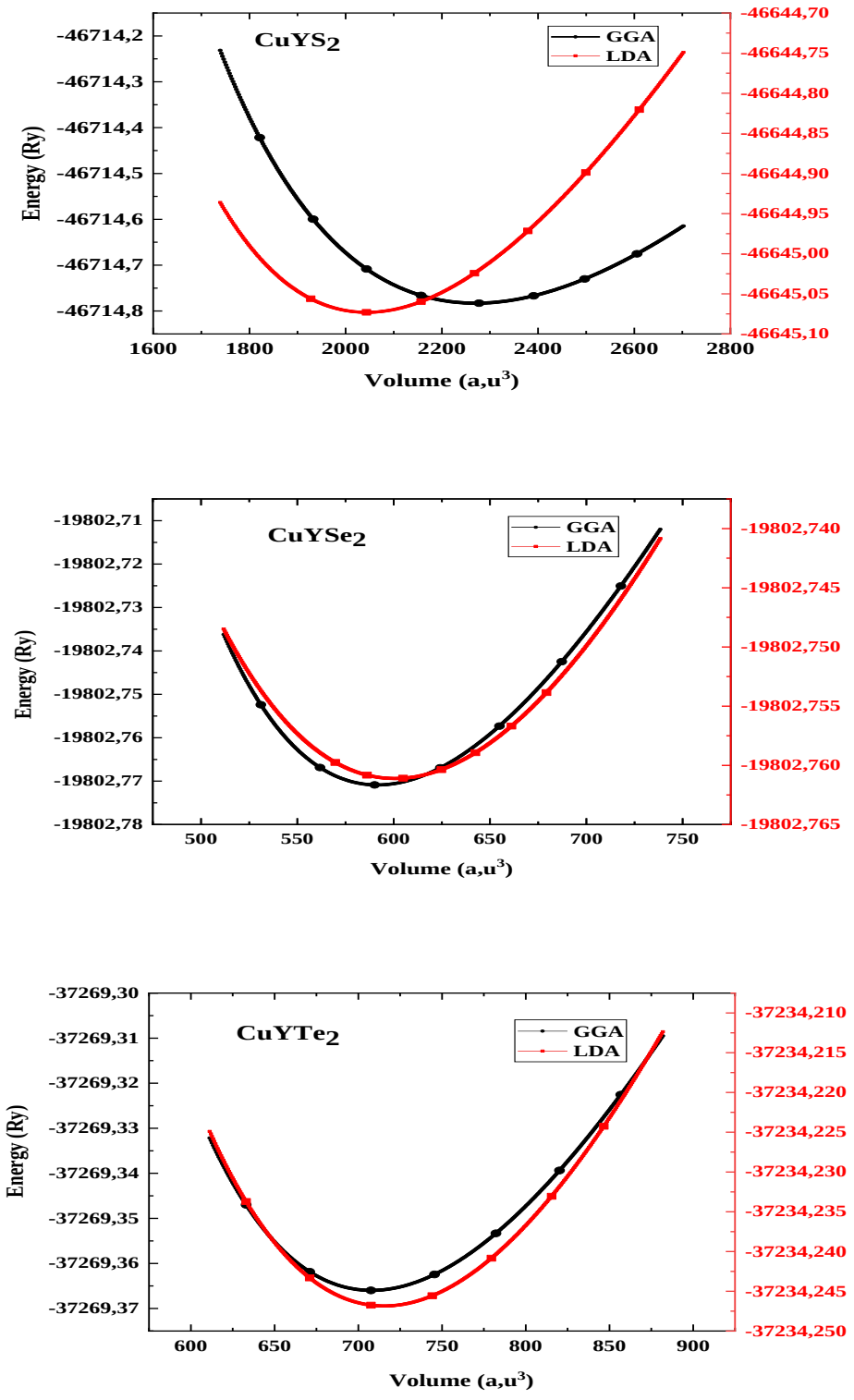

Figure. III.2. Energy-Volume optimization curves for (a) $CuYS_2$ (b) $CuYSe_2$ (c) $CuYTe_2$ compounds.

The equilibrium lattice constants, bulk modulus, and cohesive energy are calculated and denoted summarized in Table III.2 and compared with the other available results, from this table we can see that the finding lattice parameters obtained using GGA approximation for $CuYS_2$ and $CuYTe_2$ compounds are in good agreement with the other experimental results, whereas the nearest parameters of the experiment results for the $CuYSe_2$ compound are obtained using LDA approximation. The bulk modulus *B*(GPa) describes the material's resistance to any deformation caused by applying external hydrostatic pressure. Therefore, the bulk modulus values reveal that the $CuYS_2$ compound is more resistant against regular external pressure compared to $CuYSe_2$ and $CuYTe_2$ where this distinction is attributed to a disparity in the number of bonds, the strength of these bonds between atoms and the difference in structure type between $CuYS_2$ and the remaining compounds. We can confirm this result by calculating the cohesive energy of these compounds according to the following formula:

$$E_{coh} = \frac{(\mathrm{E}_{atom}^{Cu} + \mathrm{E}_{atom}^{Y} + 2\mathrm{E}_{atom}^{Z}) - \mathrm{E}_{atom}^{CuYZ_2}}{N_{Cu}+N_Y+N_Z} \qquad \text{(III.3)}$$

Where N_{Cu}, N_Y and N_Z are the numbers of Cu, Y and Z atoms, respectively, in the unit cell of the $CuYZ_2$ compound and E_{atom}^{Cu}, E_{atom}^{Y} and E_{atom}^{Z} are isolated atoms energies of the Cu, Y and Z atoms, respectively, $E_{tot}^{CuYZ_2}$ is the total energy of bulk $CuYZ_2$ compound. Comparing the cohesive energy of these compounds leads to finding that the $CuYS_2$ is more cohesive because it has higher energy and is, therefore, the most structurally stable.

Table. III.2. The Calculated equilibrium lattice constants, bulk modulus, and cohesive energy for $CuYZ_2$ (Z= S, Se and Te) using both GGA and LDA approximations.

		a (Å)	b (Å)	c(Å)	B(GPa)	B'	E_{coh} (eV/atom)
$CuYS_2$	GGA	13.446	3.979	6.287	80.594	4.1782	4.868
	Other cal [14]	13.758	4.013	6.351	73.48		-
	LDA	13.154	3.892	6.151	97.195	4.680	6.251
	Other cal [14]	13.196	3.858	6.111	84.37		-
	Exp [8]	13.453	3.981	6.290	-		-
$CuYSe_2$	GGA	3.995		6.339	71.180	4.7404	4.305
	Other cal [14]	3.994		6.372	-		-
	LDA	4.037		6.405	66.999		6.556
	Exp[9]	4.068		6.454	-		-
$CuYTe_2$	GGA	4.223		6.748	57.119	4.5038	3.874
	Other cal [10]	4.317		6.918	-		-
	LDA	4.107		6.587	73.457	5.1288	5.267
	Exp [10]	4.297		6.908	-		-

4. Electronic Properties

Knowing the electronic behavior of materials has great importance in technology because it allows us to decide the appropriate domain for their use. Band structures, state densities and electronic charge density were chosen as analysis tools. In the study of graphs of band structures and from the value of the energy gap of the forbidden band, we can specify whether the solid is insulating, semiconductor, semi-metallic or metallic. The comparison between the curves of the band structures with the densities of states and the density of electronic charge makes it possible to know the orbitals contributing to the construction of these energy bands and to understand how the bonds between the atoms of this material are formed.

4.1 The band structure

In an isolated atom the electrons orbit around the nucleus and occupy discrete energy levels, when a large number of atoms come together and interact with each other to form a crystalline

solid, the quantified energy levels rise. Hybridize and divide into different levels due to the reciprocal interaction between atoms, these levels are very close to each other so that they ultimately form a continuous energy band. The highest energy band (filled with electrons) is called the valence band; the lowest energy band (unfilled) is called the conduction band. The distance between the top of the valence band and the minimum of the conduction band is called the gap. Then the energy bands give the possible energies of an electron as a function of the wave vector k and using the dispersion equation E(k) we can plot the graph of the band structure. Note that the bands are therefore represented in reciprocal space and only the directions of highest symmetries in the first Brillouin zone are processed.

The majority of chalcogenide compounds have semiconductor behavior, as proven in several studies [15]. Due to this character, these compounds are high demand, especially in the spintronic and solar cells fields. The band structure using the TB-mBJ approach are plotted in Figure III.3.

Table III.3. Calculation of energy gaps Eg at point Γ for the chalcogenide compounds $CuYS_2$, $CuYSe_2$ and $CuYTe_2$ compared with other theoretical and experimental values.

Material	Band gap (eV)	
	This work	**Exp**
$CuYS_2$	**2.01**	**1.389[8]**
$CuYSe_2$	**1.31**	**1.53[16]**
$CuYTe_2$	**0.64**	**0.58[10]**

Band structures curves of the studied compounds indicates the presence of two bands (conduction above Fermi level and valence below) separated from each other by an indirect gap, where the value of the gaps estimated using TB-mBJ approximation are 2.01, 1.31 and 0.64 eV for $CuYS_2$, $CuYSe_2$ and $CuYTe_2$ respectively, and therefore we can say that these three compounds have semiconductor behavior. We notice that our results are in good agreement with the other experiment work [10,14,16].

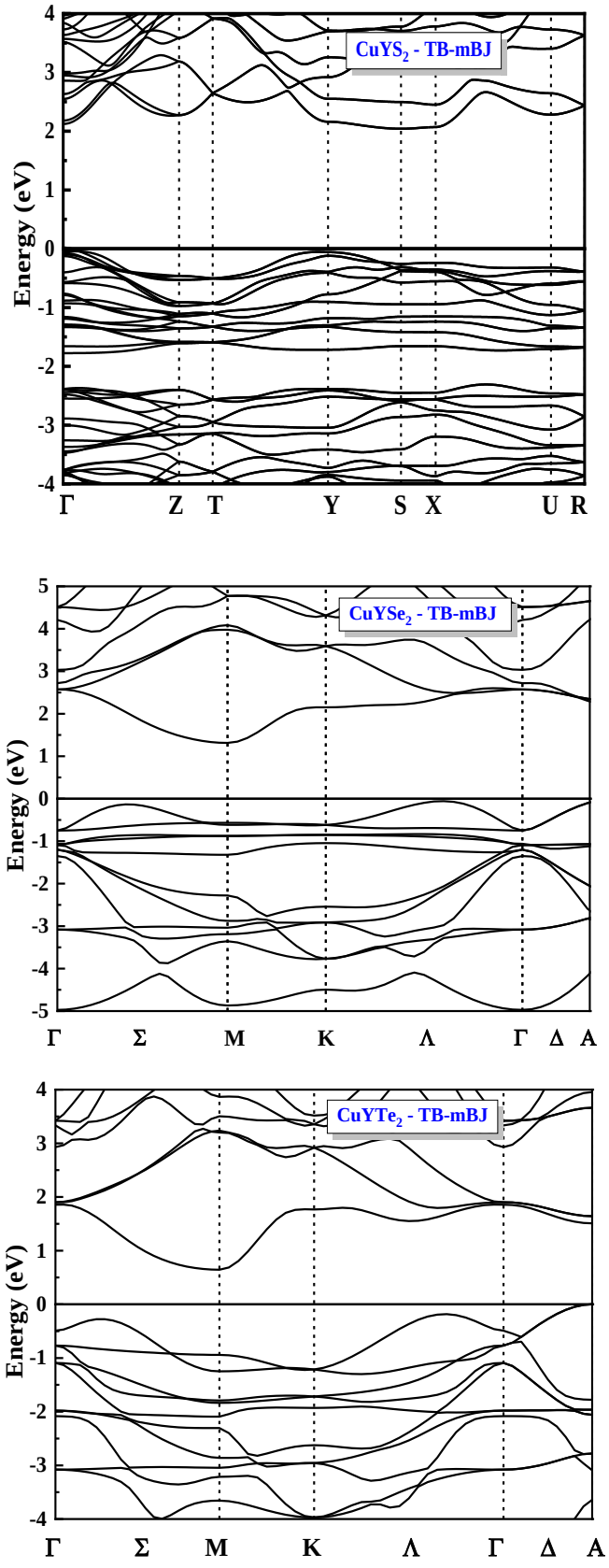

Figure. III.3. Calculated band structure for $CuYZ_2$ (Z = S, Se and Te) within the TB-mBJ approximation.

4.2 Electronic state density

In solid-state physics, the density of states (DOS) of a system describes the number of electronic states with a given energy. Unlike isolated systems, such as atoms or molecules in the gas phase, density distributions are not discrete like spectral density but continuous. A high DOS at a specific energy level means that many states having that energy and a DOS of zero means that at that energy level no states can be found. We can also use the DOS parameter as a complementary tool to interpret the formation of certain band structures, and to know the type of hybridization and the states responsible for the binding, so we are talking about the density of total and partial states.

For energies in the interval ε + dε, the density of states (DOS) is defined such that $g(\varepsilon)d\varepsilon$ is the number of energy states in the given range per unit volume, then the DOS is given by a sum over all states with the energy in the interval [ε, ε + dε]. However, since the wave vector k is used to characterize the energy states, we need to add up the total number of states having energy in the interval of interest. By taking into account the spin 2 degeneration factor and normalizing by the volume Ω of the solid, the density of states (DOS) is given by the following expression [14].

$$g(\varepsilon)d\varepsilon = \frac{1}{\Omega}\sum_{k,\varepsilon_k \in [\varepsilon,\varepsilon+d\varepsilon]} 2 = \frac{2}{(2\pi)^3}\int_{\varepsilon_k \in [\varepsilon,\varepsilon+d\varepsilon]} dk \qquad \text{(III.4)}$$

Since the energy in the free electron model does not depend on the angular orientation of the wave vector, i.e.

$$\varepsilon_k = \frac{\hbar^2|k|^2}{2m_e} \Rightarrow kdk = \frac{2m_e}{\hbar^2}\,d\varepsilon\,, k = \left(\frac{2m_e\,\varepsilon}{\hbar^2}\right)^{\frac{1}{2}} \qquad \text{(III.5)}$$

For the energy value $\varepsilon_k \in$ [ε, ε + dε] the last two equations give the density of state in a simple spherical symmetry of the form:

$$g(\varepsilon) = \frac{1}{2\pi^2}\left(\frac{2m_e\,\varepsilon}{\hbar^2}\right)^{\frac{3}{2}}\sqrt{\varepsilon} \qquad \text{(III.6)}$$

In the crystal, we can express the density of states by an explicit relation between the DOS and the band structure ε_i (k) which can be given by the following formula:

$$g(\varepsilon) = \frac{1}{\Omega}\sum_i 2\sum_k \delta\left(\varepsilon - \varepsilon_{i,k}\right) = \sum_i 2\int \frac{dk}{(2\pi)^3}\,\delta\left(\varepsilon - \varepsilon_{i,k}\right) \qquad \text{(III.7)}$$

The computation of the density of states (DOS) in the spin-polarized case is easy so that by using $\varepsilon_{i,k}^{\sigma}$ instead of $\varepsilon_{i,k}$ and $g^{\sigma}(\varepsilon)$ instead of $g(\varepsilon)$ (by replacing the factor 2 by 1) in equation (IV.8) and at the end, we obtain the DOS for each spin state which is written in the form:

$$g^{\sigma}(\varepsilon) = \frac{1}{\Omega} \sum_i 2 \sum_k \delta\left(\varepsilon - \varepsilon_{i,k}^{\sigma}\right) = \sum_i 2 \int \frac{dk}{(2\pi)^3} \delta\left(\varepsilon - \varepsilon_{i,k}^{\sigma}\right) \quad \text{(III.8)}$$

We can go further and rewrite the expression for TDOS from equation (III.8) [15]:

$$g(\varepsilon) = \frac{1}{\Omega} \sum_i 2 \sum_k \langle \varphi_{i,k} | \varphi_{i,k} \rangle \delta\left(\varepsilon - \varepsilon_{i,k}\right) \quad \text{(III.9)}$$

Where $|\varphi_{i,k}\rangle$ are the eigenstates of KS corresponding to the eigenvalues $\varepsilon_{i,k}$.

We can calculate the partial (projected) density of states (PDOS) $n_i\ (\varepsilon)$ after calculating the polarized spin, we choose to project the TDOS on the atomic orbitals (e.g., s, p and d) to get the contribution partial of each atomic orbital [14]:

$$n_i\ (\varepsilon) = \sum_n \delta\ (\varepsilon - \varepsilon_n) |P_{ni}^{a}|^2 \quad \text{(III.10)}$$

To understand the formation of each band in band structure spectra, we analyze the total and the partial density of the atomic orbitals states that shown in Figure III.3. According to this figure, we notice that there is no density of the state around the Fermi level, which confirms the semiconductor behavior of these compounds. Also, for $CuYS_2$ in its orthorhombic phase structure, it is clear that the conduction band is formed mainly by the dominant contribution of the "d" orbitals of the Yttrium atom, with the presence of weak contribution from "s" and "p" orbitals of Cu and Y atoms while the "d" and "p" orbitals of the Cu and S atoms respectively which they exhibit a strong hybridization in the range of -5 eV to 0 eV, on the other hand, the contribution of "s" orbital of "S" atom was located around -12 eV. Partial density of states (PDOS) curves of $CuYSe_2$ and $CuYTe_2$ compounds have appeared that the valence band below Fermi level was formed due to "s" orbital of Se and Te atoms contribution near to -12 eV energy value, while "p" orbital of Se and Te atoms has contributed in the range [-5 ; 0 eV] and hybridized with "d" orbital of Cu atoms. For the conduction band, the partial density curves for both $CuYSe_2$ and $CuYTe_2$, appears a dominant contribution of "d" orbital of Y atoms. Through total partial density of states analysis, our obtained results are similar to the previous studies [14,16].

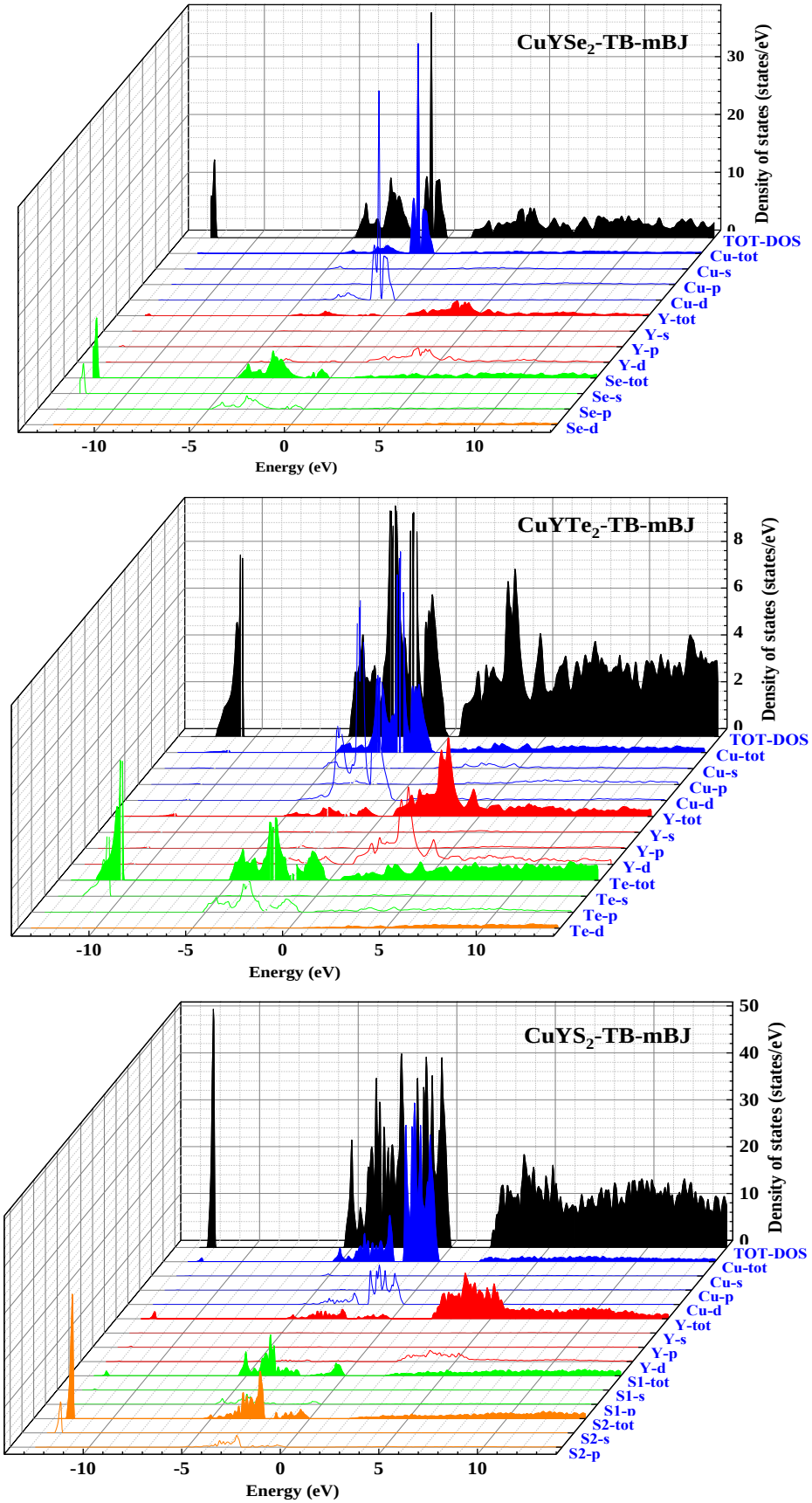

Figure. III.4. Calculated total and partial density of states for $CuYZ_2$ (Z = S, Se and Te) within the TB-mBJ approximation.

5. Optical properties

The effect of incident light on solid materials differs depending on their electronic behavior (conductor, insulator, or semiconductor), electronic density, and the gap separating the valence bands from the conduction, and the number and the nature of bonds between their atoms. For semiconductor materials, this difference is mainly due to the value of the energy carried by the electromagnetic waves, the photon-electron interaction and valence band electrons, where the electric field of the electromagnetic waves interacts with electrons and polarizes them in its same direction. As a result of this polarization, the light energy can be absorbed through the excitation of the valence electrons, in which this polarization gives sufficient energy to the electrons that allows them to move from the valence band to the conduction band in the so-called interband transition, where the excited electrons, the energy range in which the interband transition occurs, and the atomic orbital to which they transform to/or from can be inferred and determined depending on the electronic state density analysis. These phenomena can be depicted in terms of time-dependent perturbations of the ground-state electronic states. As another result of the polarization, the velocity of these electromagnetic waves can be reduced when across the material, where the refraction of the light occurs and its path changes. Absorption, reflection, refractive index, and energy loss coefficients are among the main characteristics that indicate usability of material in a specific application, whether as optical filters, optical detectors, sensors, or anti-reflection coatings.

Knowledge of the different ways and forms of the interaction of light with matter in solid-state physics is of great importance. For example absorption, transmission, reflection, scattering and emission. The study of the optical properties of solids is an important tool in understanding the electronic properties of materials. In some particular structures, the energy dependence of the properties, mentioned above, on the band structure is very important. Crucial information on the eigenvalues as well as the eigenfunctions is necessary to calculate the frequency/energy dependent on the optical properties [17].

The optical properties were studied using the dielectric complex function $\varepsilon(\omega)$ as a function of real ($\varepsilon_1(\omega)$) and imaginary ($\varepsilon_2(\omega)$) parts given by the formula [17–20]:

$$\varepsilon(\omega) = \varepsilon_1(\omega) + i\,\varepsilon_2(\omega) \qquad \text{(III.11)}$$

The real part of the dielectric function $\varepsilon_1(\omega)$ present the dispersion of the incident photons by the substance's [20] and it gives us more information about the electronic polarization state of the material[21] while the imaginary part of the dielectric function $\varepsilon_2(\omega)$ means the energy absorbed by

the material. The Imaginary part $\varepsilon_2(\omega)$ is estimated using the electronic band structure by relating the momentum matrix elements between the occupied and unoccupied electronic states [22] whereas the real part can be obtained from the Imaginary part $\varepsilon_2(\omega)$ using the Kramers–Kronig transformation [23].

The real and imaginary parts of the dielectric functions of the studied compounds are calculated using TB-mBJ approximation along each x, y, and z directions and presented in Figures III.6. Through this figures, we can see that the values of the real part $\varepsilon_1(\omega)$ at zero frequency present the static dielectric constant which are calculated and summarized in Table III.3 where we can see reveals that $CuYTe_2$ has a higher value compared to the other compounds. Also, we can observe that the spectra of $\varepsilon_1(\omega)$ increase sharply from the static dielectric constant $\varepsilon_1(0)$ and reaches its maximum value at energies equal to 10.5, 9.0 and 7.0 eV for $CuYS_2$, $CuYSe_2$ and $CuYTe_2$ respectively, since then gradually decreases to take negative values in the range [8 ; 18eV] for all the studied compounds where their behavior in this region they transform from metallic to dielectric and therefore the dispersion is unavailable in this range, unlike to the absorption coefficient, which has a greater value in this range.

Regarding the spectra of the imaginary part $\varepsilon_2(\omega)$ plotted in figures (III.5 and III.6), we can see that the optical band gaps obtained from the imaginary part of the dielectric function calculated using TB-mBJ approximation are 2.01, 1.31 and 0.56 eV for $CuYS_2$, $CuYSe_2$ and $CuYTe_2$ respectively. The $\varepsilon_2(\omega)$ spectra express the absorption that can occur as a result of electronic excitation from the valence states below the Fermi level to the conduction states where through this spectra we can observe that this absorption can only occur if the energy value of the incident photons is greater than the energy gap.

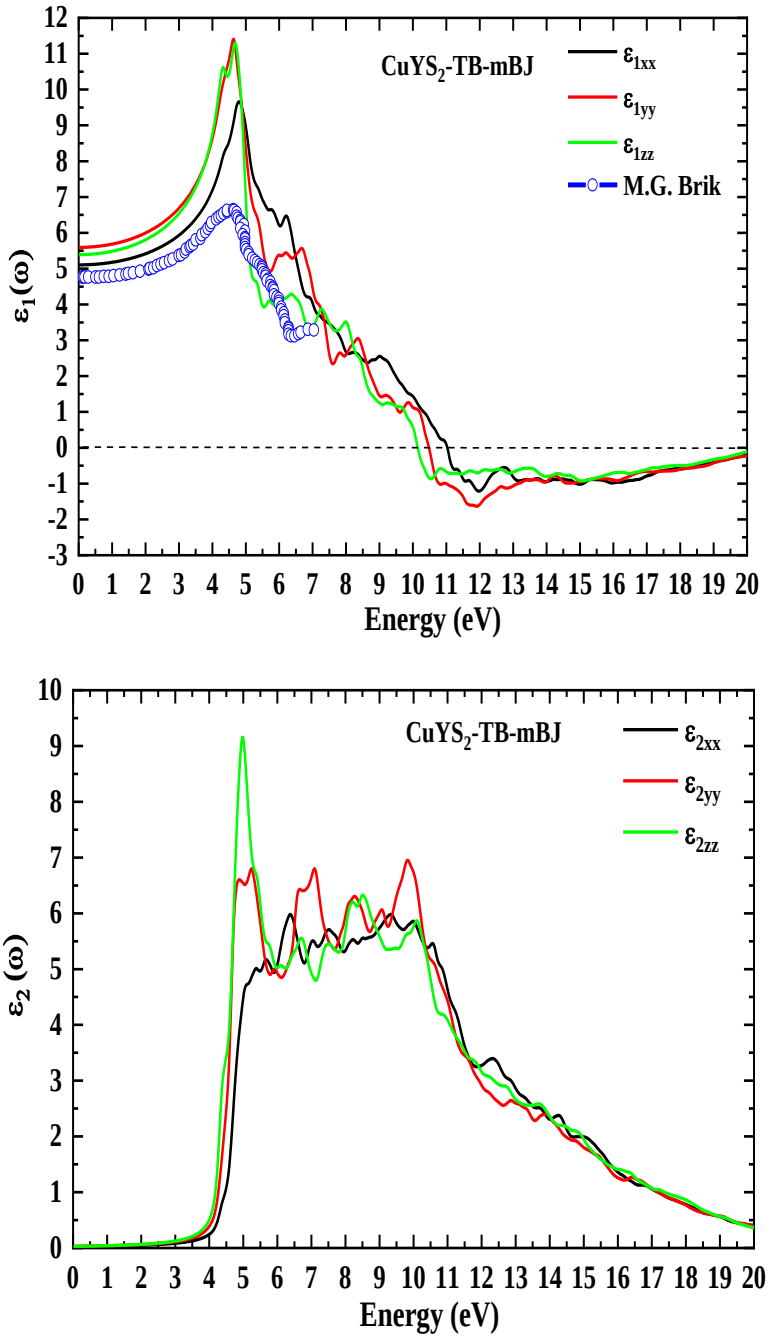

Figure. III.5. Real and imaginary part of the dielectric function for $CuYS_2$ within TB-mBJ approximation compared the real one with other computational work.

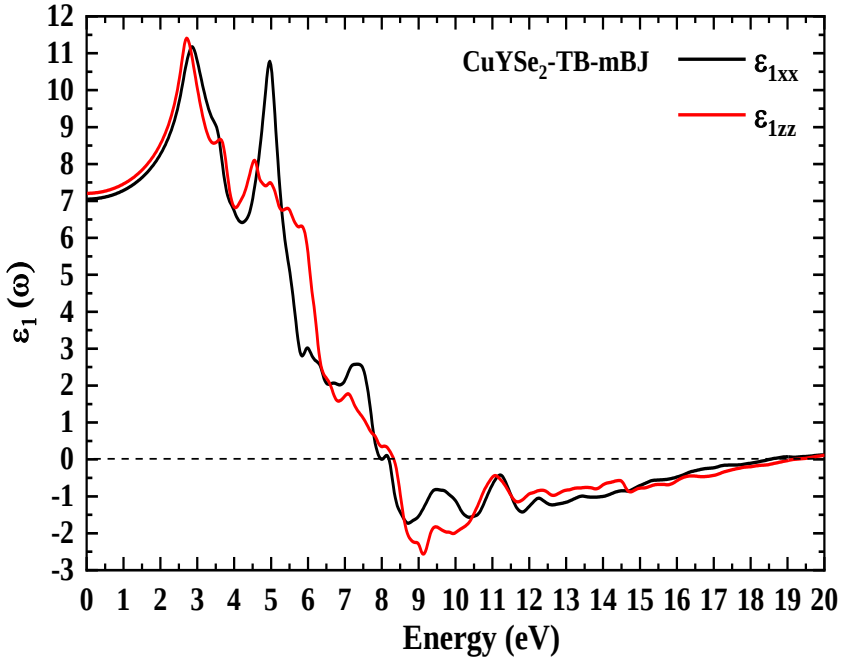
CuYSe2-TB-mBJ
ε1xx
ε1zz
ε1 (ω)
Energy (eV)

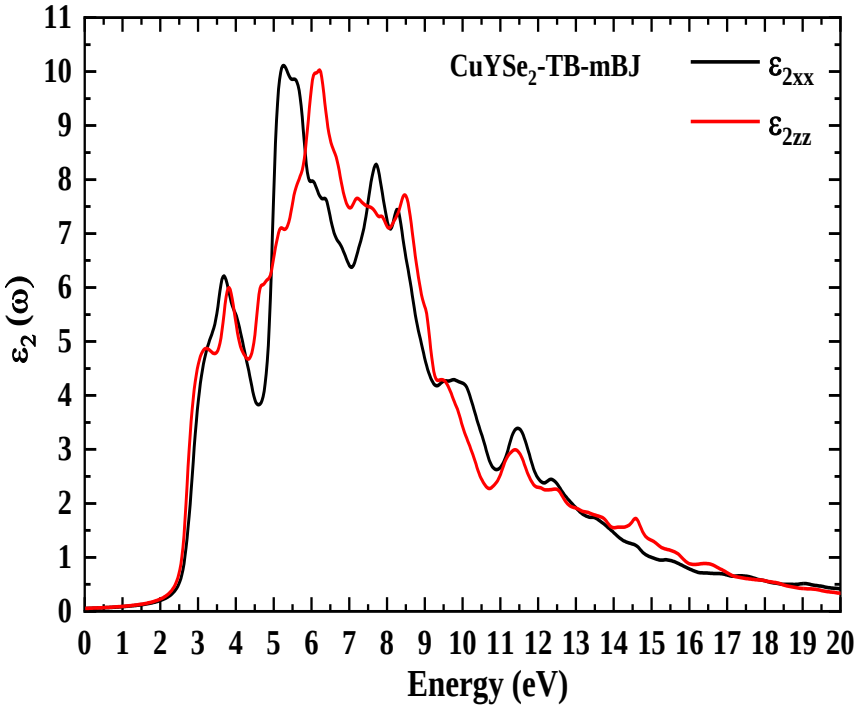
CuYSe2-TB-mBJ
ε2xx
ε2zz
ε2 (ω)
Energy (eV)

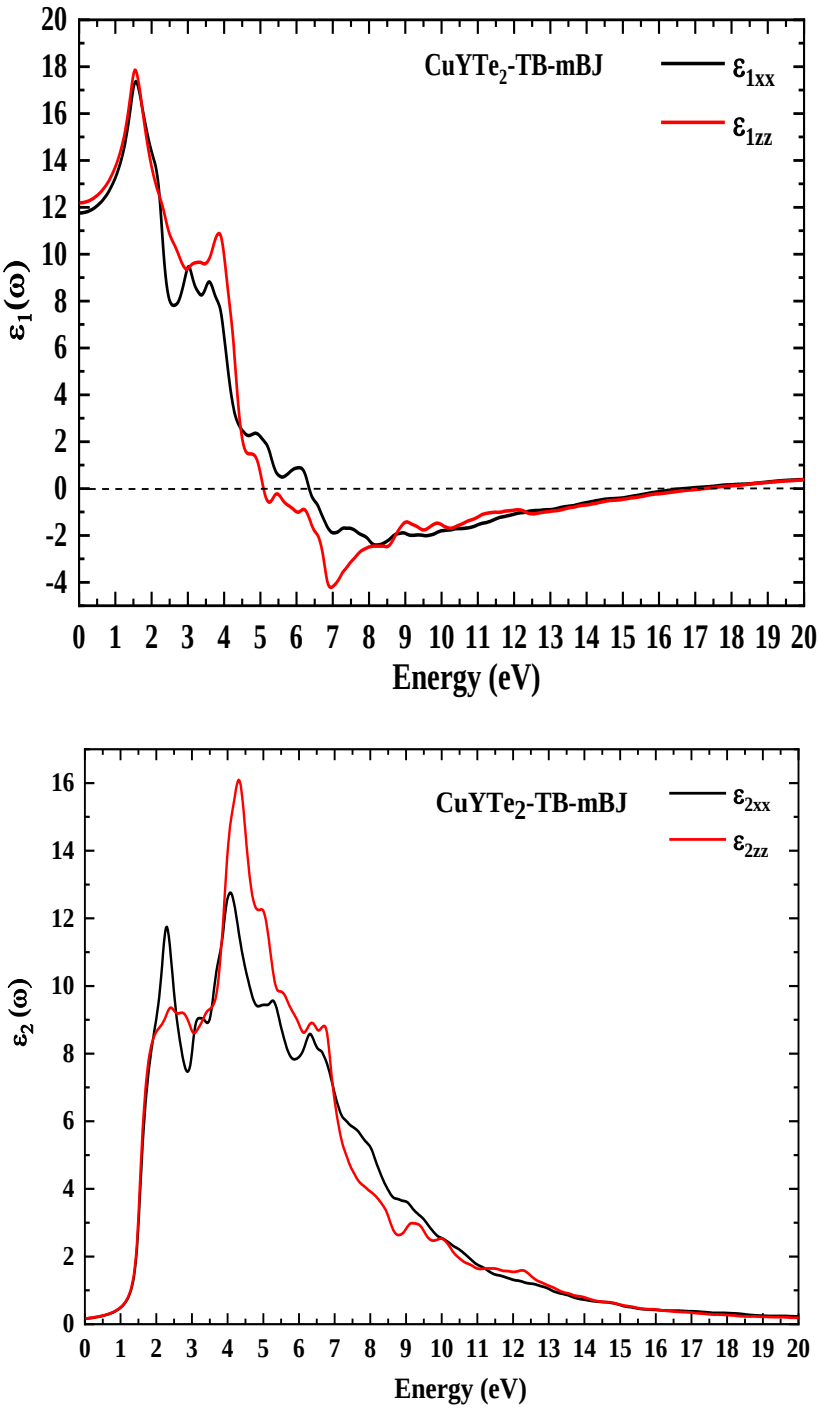

Figure. III.6. The computed real and imaginary part of the dielectric function for $CuYSe_2$ and $CuYTe_2$ within TB-mBJ approximation.

Table. III.4. The values of the refractive index and the static dielectric constant.

		$\varepsilon_1(0)$	$n(0)$	$R(0)$
$CuYS_2$	mBJ-GGA	4.942	2.22	0.144
	mBJ-LDA	5.105	2.26	0.149
$CuYSe_2$	mBJ-GGA	7.632	2.76	0.219
	mBJ-LDA	7.048	2.65	0.205
$CuYTe_2$	mBJ-GGA	11.754	3.42	0.301
	mBJ-LDA	13.200	3.63	0.323

The light incidence as an electromagnetic waves on the material causes electrons in the valence band to absorb the energy and raising its energy level [25]. The absorption coefficient α(ω) is connected to the extinction coefficient k(ω), by the following formula [24]:

$$\alpha(\omega) = \frac{4\pi}{\lambda} K(\omega) \tag{III.12}$$

Where λ is the wavelength of light in vacuum. Also the absorption coefficient α(ω) can be calculated using another formula [24]:

$$\alpha(\omega) = \frac{2\pi\omega}{c} \sqrt{\frac{-R_e(\varepsilon(\omega)|\varepsilon(\omega)|)}{2}} \tag{III.13}$$

According to Figure.III.7, the absorption edge is located at around 2.04eV for $CuYS_2$, 1.31eV for $CuYSe_2$ and 0.56eV for $CuYTe_2$ where all the studied compounds have a good response in the range of 11.3 to 47eV for $CuYS_2$, 6.25 to 47eV for $CuYSe_2$ and 5.7 to 47eV for $CuYTe_2$ to incident photons.

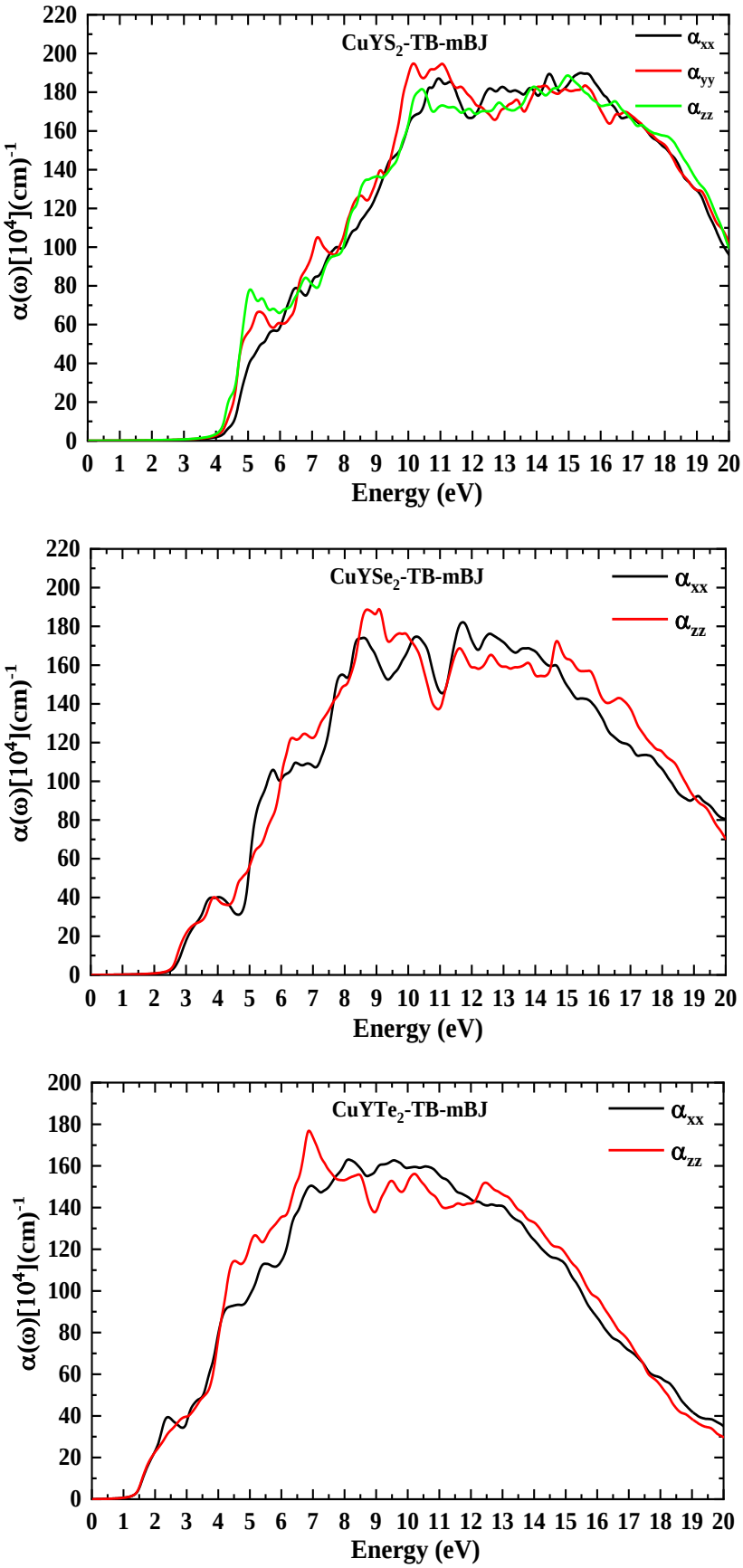

Figure. III.7. Absorption coefficient of $CuYZ_2$ (Z= S, Se and Te) within TB-mBJ approach.

The optical refractive index, conductivity and the reflectivity are presented in Figures (III.8 - III.10). We have determined the refractive index given by using the real and imaginary parts of the dielectric function [24]:

$$n(\omega) = \frac{1}{\sqrt{2}}\left[\sqrt{\varepsilon_1(\omega)^2 + \varepsilon_2(\omega)^2} + \varepsilon_1(\omega)\right]^{\frac{1}{2}} \quad \text{(III.14)}$$

The refractive index n_0 at zero frequencies and the maximum values are shown in table III.4 At zero-frequency, the refractive index is 1.91 for $CuYS_2$, 1.88 for $CuYSe_2$ and 1.98 for $CuYTe_2$ with maximum values of 2.80 at 6.59 eV for $CuYS_2$, 2.92 at 7.90eV and 3.12 at 6.81eV for $CuYSe_2$ and $CuYTe_2$ respectively.

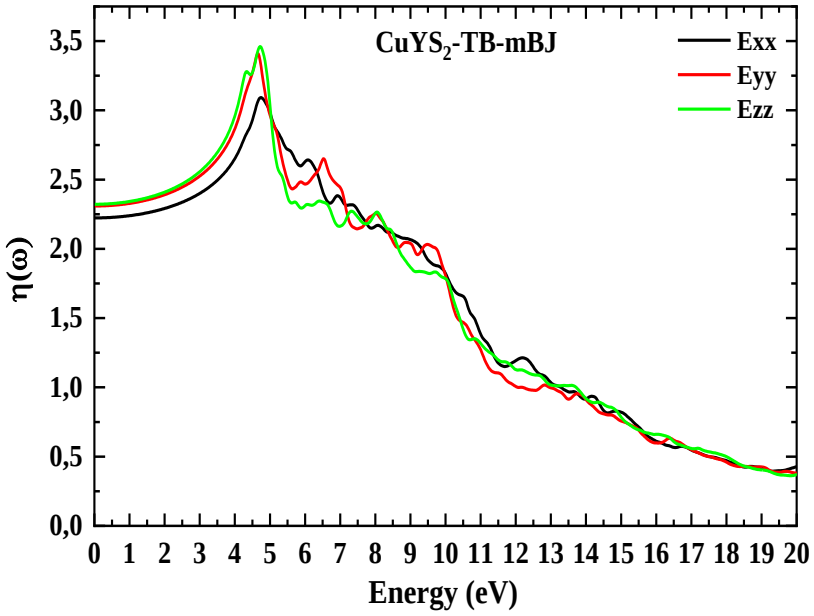

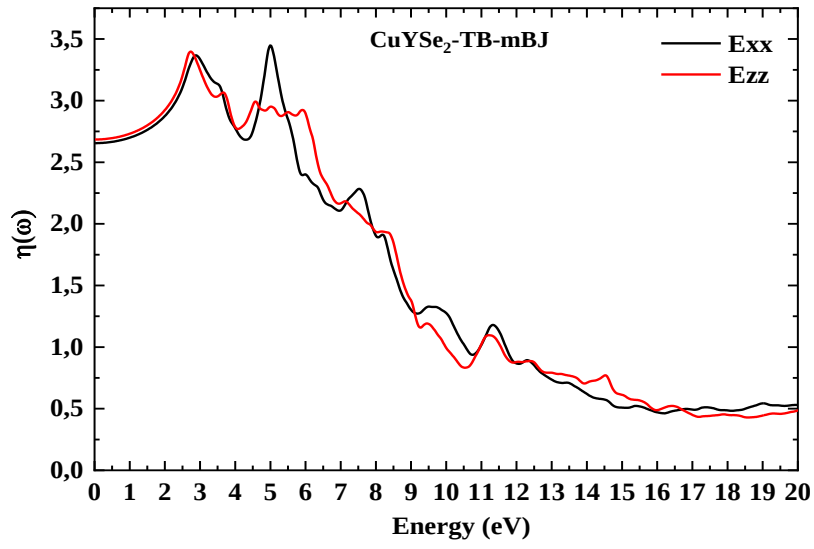

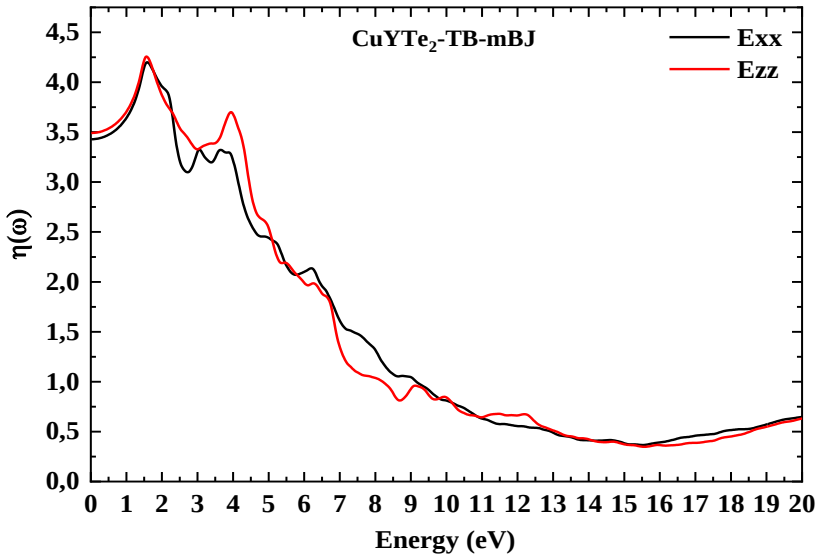

Figure. III.8. Optical refractive index of $CuYTe_2$ with (Z = S, Se and Te) within TB-mBJ approach.

We define another parameter, which is the reflectivity coefficient R(ω). This parameter characterizes the part of the reflected energy from the solid surface and can be derived by the refractive index [24] as follows :

$$R(\omega) = \left|\frac{(n(\omega)-1)^2+k^2(\omega)}{(n(\omega)+1)^2+k^2(\omega)}\right| \qquad \text{(III.15)}$$

In the Figure III.9, the optical reflectivity of $CuYZ_2$ (Z = S, Se and Te) was plotted as function of the light energy where the zero-frequency reflectivity limit of $CuYZ_2$ is found to be 0.14 for $CuYS_2$, 0.21 for $CuYSe_2$ and 0.30 for $CuYTe_2$. We can see also that the high reflectivity peaks are observed at energies 15.76eV, 9.03eV and 11.16eV for $CuYS_2$, $CuYSe_2$ and $CuYTe_2$ respectively.

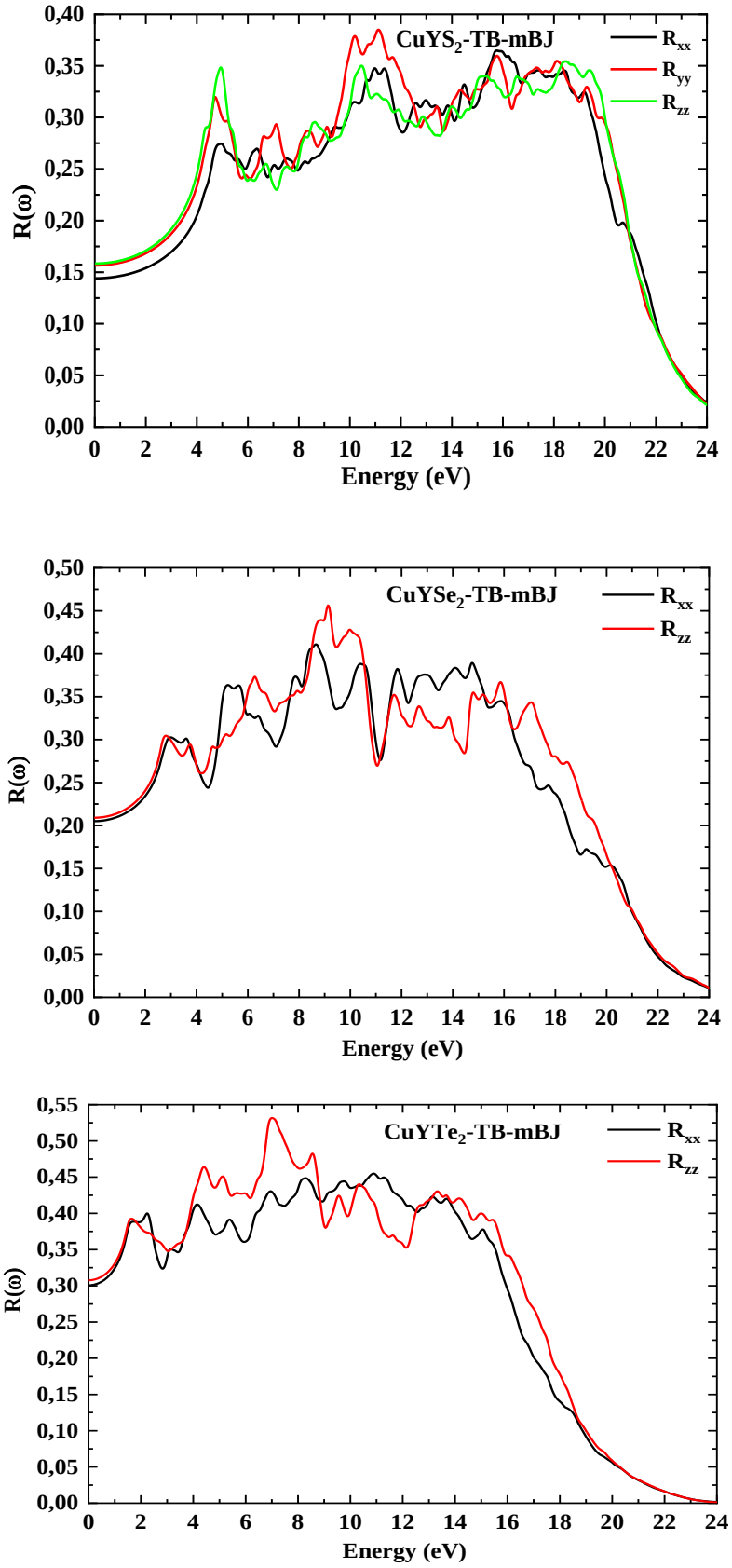

Figure. III.9. Optical reflectivity of $CuYZ_2$ with (Z = S, Se and Te) using TB-mBJ approach.

Optical conductivity is a complex quantity defined by the following formula [26]:

$$\sigma(\omega) = -\frac{i\omega}{4\pi}\varepsilon(\omega) \qquad \text{(III.16)}$$

Figure III.10 shows that the optical conductivity starting from 2.04eV, 1.31eV and 0.56eV to $CuYS_2$, $CuYSe_2$ and $CuYTe_2$ respectively. As remark, the maximum of optical conductivity of the compounds is at 10.57eV for $CuYS_2$, 8.28eV for $CuYSe_2$ and 6.62eV for $CuYTe_2$.

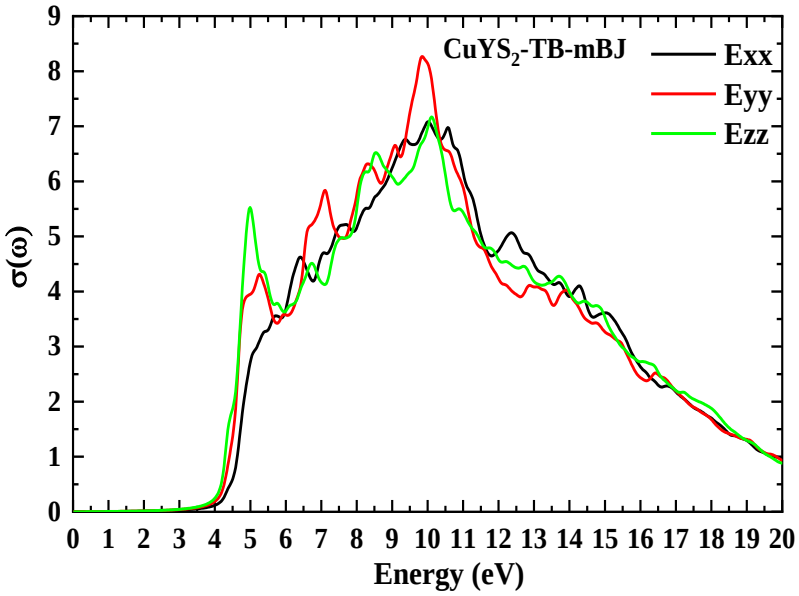

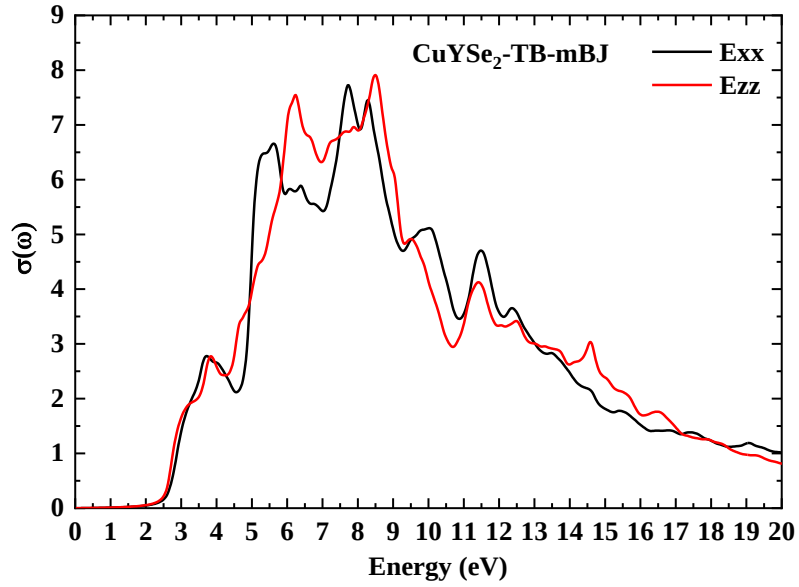

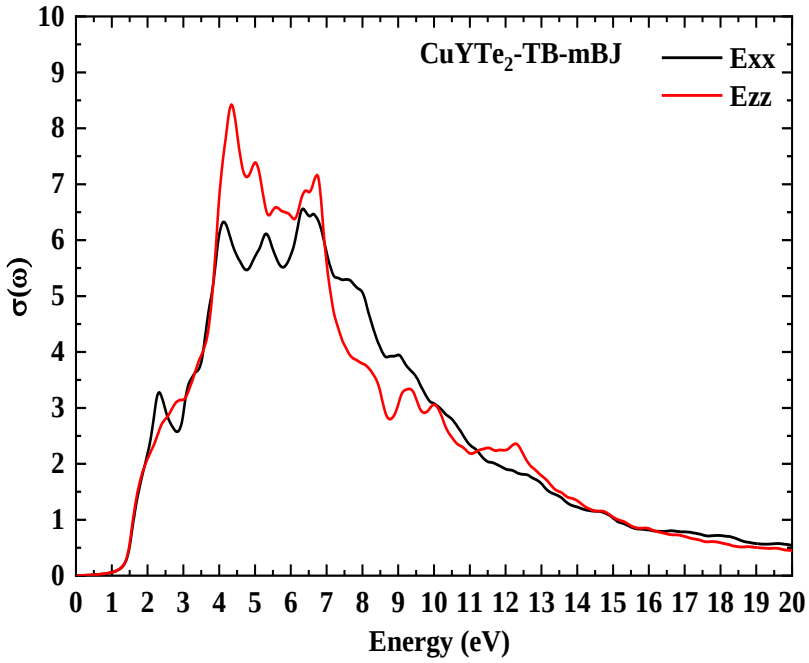

Figure. III.10. Optical conductivity of $CuYZ_2$ (Z= S, Se and Te) using TB-mBJ approach.

6. Thermodynamic properties

Getting high efficiency for materials that used in solar energy systems requires the full knowledge of their properties such as the various changes occurred to their properties when under temperature and pressure effects. The most important characteristics that we studied included the changes in their energy absorption ability, their thermal expansion coefficient, and the resistance to deformation and other properties.

All these properties were theoretically investigated in a temperature range of up to 1000 K and under the pressure influence up to 30 GPa. It calculation was performed using the quasi-harmonic Debye model [26] applied in the GIBBS2 code [27, 28].

To study the thermodynamic properties variation of a solid matter under the influence of temperature and pressure, we use the Gibbs free energy given by:

$$G^*(x, V; P, T) = E_{stat}(x, V) + PV + A^*_{vib}(x, V; T) + F^*_{el}(x, V; T) \quad \text{(III.17)}$$

Where E_{stat} is the total energy, PV corresponds to the hydrostatic condition.

A^*_{vib} and F^*_{el} are the non-equilibrium vibrational Helmholtz free energy and electronic free energies respectively.

Using Debye's model allows to express the non-equilibrium vibrational Helmholtz free energy A^*_{vib} in terms of the density of phonon states (the vibrational density of states) g(ω):

$$A^*_{vib} = \int_0^{\infty} \left[\frac{\omega}{2} + k_B T \, Ln\,(1 - e^{-\frac{\omega}{k_B T}})\right] g(\omega) d\omega \quad \text{(III.18)}$$

$$F^*(x, V; T) = E_{sta}(x, V) + A^*_{vib}(x, V; T) \quad \text{(III.19)}$$

Where n represents the atoms number per unit volume, and D (θ/T) indicates the Debye integral, which is written as:

$$D(x) = \frac{3}{x^3} \int_0^x \frac{y^3 e^{-y}}{1 - e^{-y}} \, dy \quad \text{(III.20)}$$

To get the equilibrium state, we minimize Gibbs free energy G^* with respect to volume at constant pressure and temperature:

$$\left(\frac{\partial G^*(V,P,T)}{\partial V}\right)_{P,T} = 0 \quad \text{(III.21)}$$

Solving the last equation enable us to find formulas of various thermal quantities, such as:

Entropy (S), the heat capacity at constant volume (C_v), and the thermal expansion coefficient (α) which are given by:

$$S = -3nk_B \ln\left(1 - e^{-\Theta_D/T}\right) + 4nk_B D(\Theta_D/T) \quad \text{(III.22)}$$

$$C_v = 12nk_B D(\Theta_D/T) - \frac{9nk_B \Theta_D/T}{e^{\Theta_D/T} - 1} \quad \text{(III.23)}$$

$$\alpha = -\frac{1}{V}\left(\frac{\partial V}{\partial T}\right)_P = \frac{\gamma C_v}{V B_T} \quad \text{(III.24)}$$

Heat capacity at volume constant C_v that is expressed by the formula (III.23) depicts how much energy can be absorbed by 1 mole of compound when temperature increases by 1 K and is the result of vibrations of the atoms of lattice [28]. We plotted in Figure III.11 the variation of heat capacity of $CuYZ_2$ (Z= S, Se and Te) as a function of volume and pressure.

6.1 Heat capacity at constant volume C_V

The heat capacity of a solid is given by a relation deduced from the vibratory movements of the crystal lattice, and experimentally it expresses the amount of heat necessary to change its temperature by one degree (has one unit of energy per degree). The heat capacity of metals is very important because it expresses the ability of a substance to absorb energy. This ability logically

increases with increasing number of degrees of freedom of a particle. The thermal capacities C_V and C_P increase with the pressure (The closer the particles come together, the greater the inter-particle forces. Part of the heat supplied is stored in the form of potential energy).

Figure III.11-a shown that at low temperature (smaller than 200k) C_v increases with temperature and proportions to T^3, whereas it set up (100 j/mol.k) at a temperature equal or greater than 450K which is in accordance to Petit Dulong law [29]. At ambient temperature (300k), all studied compounds have high heat capacity values, where the greatest value was for $CuTe_2$ (96.47 j/mol.k) and the smallest value for $CuYS_2$ (91.89 j/mol.k). On the other hand, pressure affects the heat capacity C_v, where the curves C_v-P in figure III.11-b appears a linear decrease of the heat capacities values with pressure increasing of all compounds.

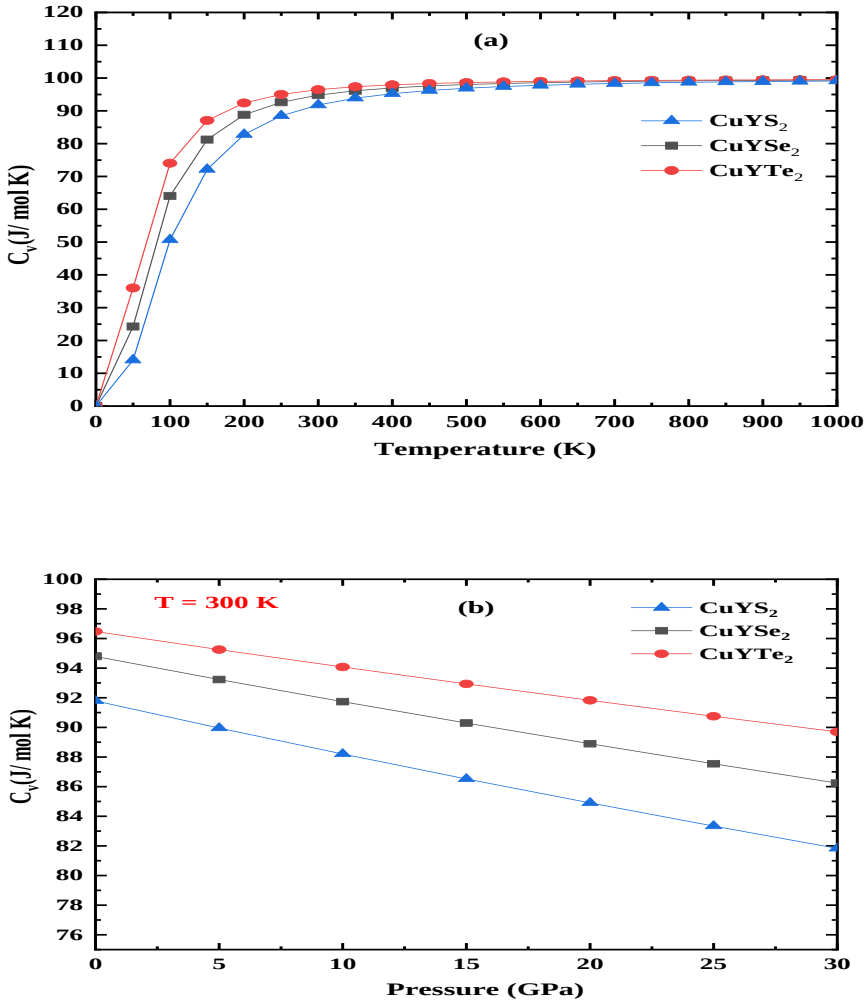

Figure. III.11. Pressure and temperature dependence of heat capacity "C_v" on $CuYZ_2$ (Z= S, Se and Te) compounds.

6.2 The entropy of the system S

On a microscopic scale, entropy can be defined as a measure of the disorder of a system, and it is viewed as a measure of the number of possible configurations. When the temperature increases the atoms start to vibrate then new configurations become possible (the higher the entropy of the system, the less ordered its constituent elements). The increase in the value of entropy causes a certain change at the microscopic level of the substance and among these changes, we quote the vibrations of the atoms, which move away from their equilibrium positions, the electrons pass from an electronic level to another higher or change in spin state and random occupation of crystallographic sites in disordered alloys.

At the macroscopic scale, the entropy of the system is the amount of internal energy of the substance, which is not convertible into useful work, it can be considered as the energy unusable to obtain a work per unit temperature.

We plotted in figure III.12 the pressure and temperature effects on entropy thermal quantity and this latter means the unconvertible energy in system. According to figure III.12-a, $CuYTe_2$ has higher entropy compared to the other compounds, also, the three curves of entropy change with increasing pressure and temperature and show a quasi-linear increase in entropy with increasing temperature and pressure for each of them separately. We can explain this observation as follow: the increase of temperature leads to a growth in the vibration modes and consequently the number of configurations possible while increasing pressure affects the atoms movement and therefore decreases the numbers vibrations atoms.

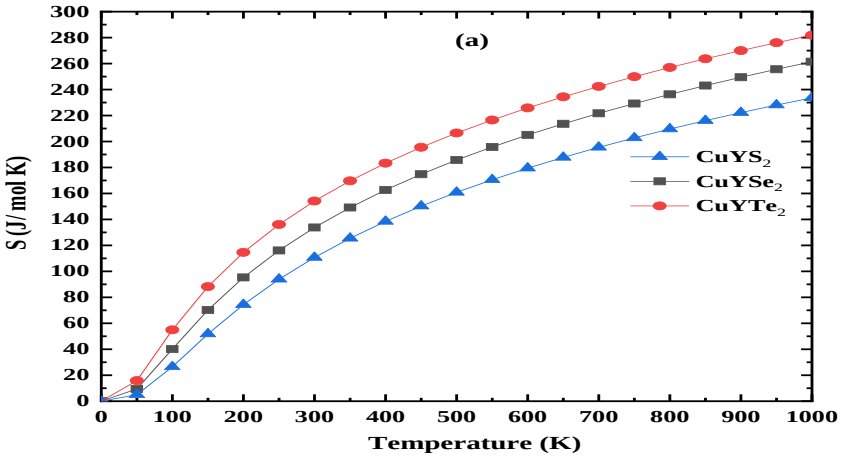

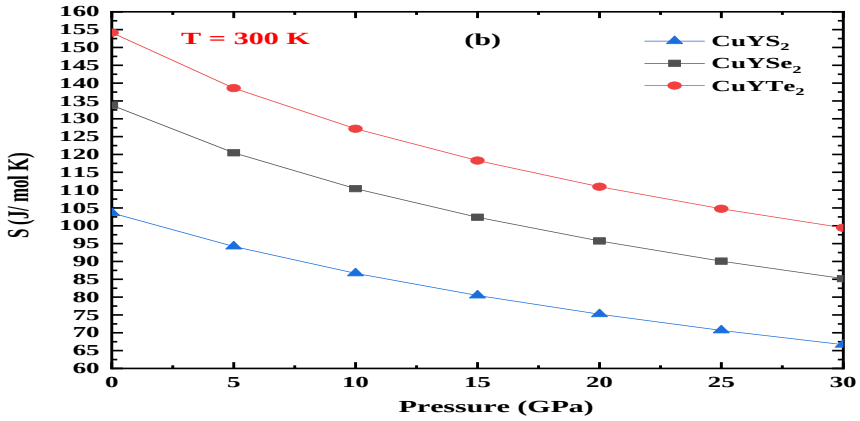

Figure. III.12. Pressure and temperature dependence of entropy "S" of $CuYZ_2$ (Z= S, Se and Te) compounds.

Thermal expansion expresses the proportion of change in dimension per unit degree temperature change at constant pressure when the temperature changes. Higher temperature leads to rise in the movement of the atoms that make up the substance and this leads to a change in its volume. Vibrations of the constituent atoms of the substance always play an important role and affected by external heat and their inter-atomic distances [30].

The coefficient of thermal expansion is related to several factors [31] such as the nature of its constituent atoms, the number of bonds, and the type of its structure.

Figure III.13-a shows the variation of the coefficient of thermal expansion as a function of temperature. According to this figure, we can see that the thermal expansion of all studied compounds increases rapidly for temperatures less than 200K and slowly for higher than 200K. Also, we can notice that at temperatures less than 350K, $CuYTe_2$ compound has the greatest thermal expansion coefficient, while at temperatures higher than 350K the $CuYSe_2$ thermal expansion value become upper than the other.

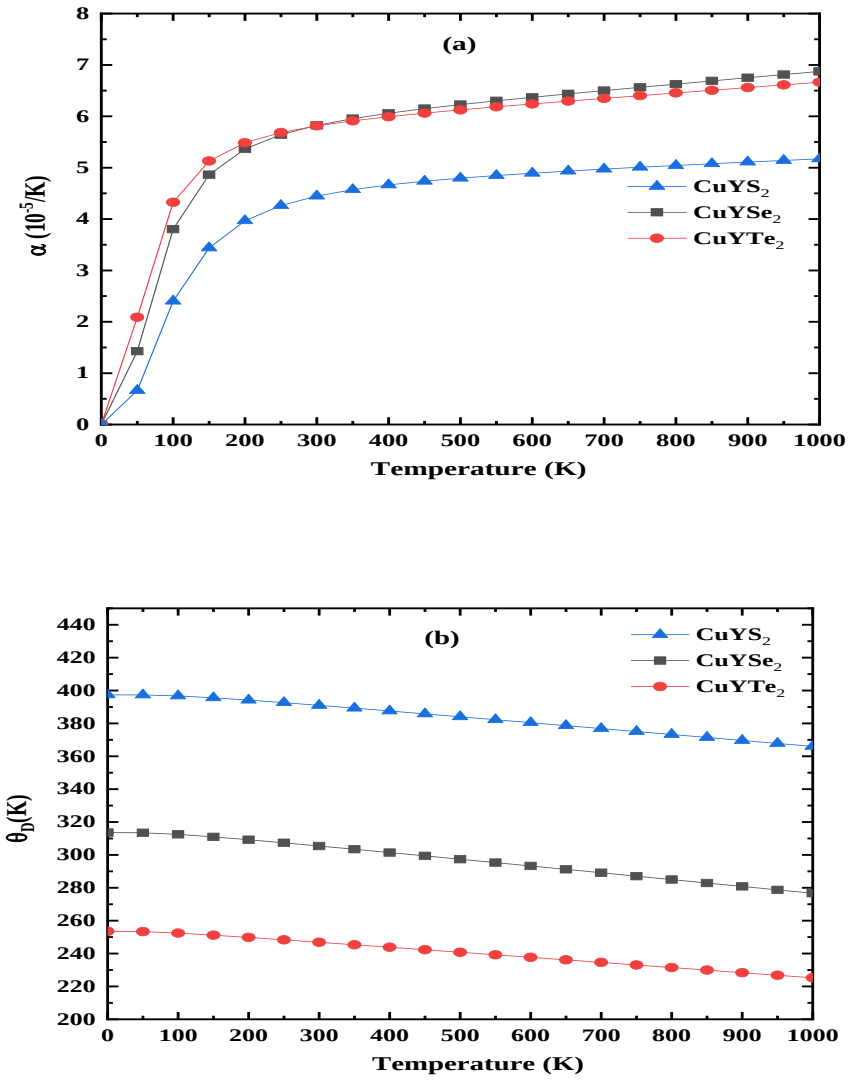

Figure. III.13. Temperature dependence of entropy "S" of $CuYZ_2$ (Z= S, Se and Te) compounds.

The most important thermal property is the Debye temperature. It is associated with many mechanical and elastic properties, and it represents the temperature that caused the greatest number of vibration modes, Also, Debye temperature θ_D is associated to sound velocity due to the reason that vibrations of solid are considered as elastic waves [28,32]. The obtained results of the temperature dependence of Debye temperature for all compounds $CuYZ_2$ (Z= S, Se and Te) are plotted in figure III.13-b. Curves of θ_D-T exhibit a linear decreasing of Debye's temperature with increasing temperature where $CuYS_2$ has the highest value compared to $CuYTe_2$ and $CuYSe_2$ compounds.

7. Thermoelectric properties

To estimate Seebeck coefficient, electrical conductivity (σ/τ), the thermal conductivity (κ/τ) and electronic specific heat capacity (c) of $CuYZ_2$ compounds (Z= S, Se and Te) for different temperature (300, 500 and 700K) in the first step where the positive value of chemical potential (μ) reveals that the doping is n-type whereas the negative value indicates the p-type doping [33], and at Fermi level for each $CuYZ_2$ (Z = S,Se and Te) compound at room temperature equal to 300K we depend on the semi-classical Boltzmann transport theory implemented in BoltzTraP code [7].

The intrinsic Seebeck coefficient is the ratio of the voltage created between the ends of a material when its ends are exposed to a thermal gradient. This thermal gradient causes the moving charge carriers (electrons or holes) [34] and induced an electrical current.

We plotted in Figure (III.14-a) the variation of Seebeck coefficient along the relative chemical potential μ to the Fermi level μ_0 for all $CuYZ_2$ (Z= S , Se and Te) compounds at three temperatures values (300, 500 and 700K). According to the obtained results, we can see at a temperature of 300K that the Seebeck coefficient is as great as possible for the three materials studied. We can also see that the $CuYS_2$ compound has a significantly higher Seebeck coefficient than the other two compounds, with a maximum value set up 2.7mV/K at 300K and decreasing to 1.6mV/K if the temperature increases to 700K. Figure (III.14-b) shows the temperature variations of the Seebeck coefficient computed exactly at the Fermi level. The Seebeck coefficient rises to its maximum value at temperatures 650, 350, and 500K for $CuYS_2$, $CuYSe_2$, and $CuYTe_2$ respectively, whereas the coefficient of Seebeck for the $CuYSe_2$ compound at room temperature is greater than for the remaining compounds.

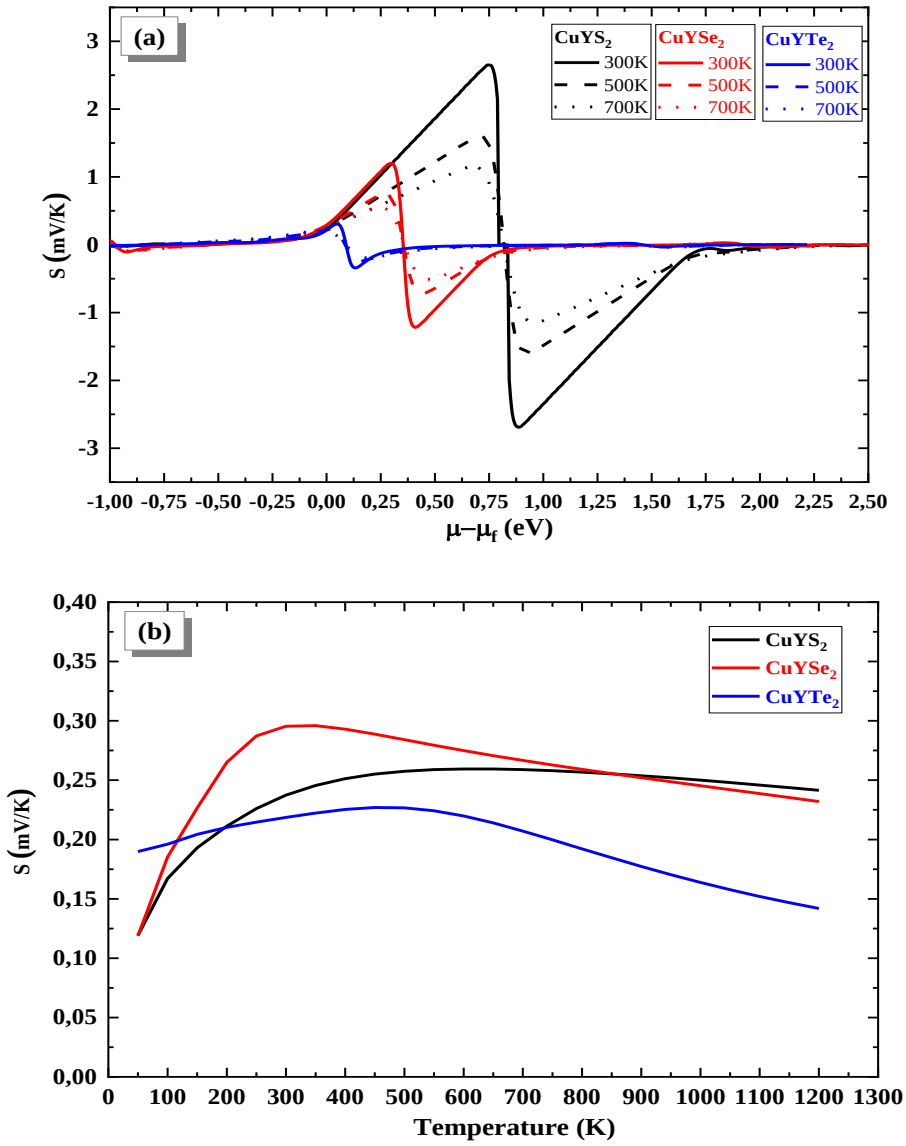

Figure. III. 14. Variation of Seebeck coefficient for $CuYZ_2$ (Z= S, Se and Te) as function of: (a) the relative chemical potential for different temperature values (300, 500 and 700K). (b) as function temperature at Fermi level.

The other three important parameters in the study of thermoelectric phenomena are the electrical conductivity (σ/τ), electronic thermal conductivity (κ/τ) and electronic specific heat (c) of the free electrons in material where these factors expresses the contribution of the movement of electrons to the conductivity of electric current, its contribution to thermal conductivity and its contribution to the heat capacity of the material, respectively. In Figures III.15-17, we have plotted the variation of the electrical conductivity (σ/τ) coefficient, the electronic thermal conductivity (κ/τ) and electronic specific heat (c) of $CuYZ_2$ in terms of chemical potential in different temperatures (300, 500 and 700K) and as function of temperature at Fermi level.

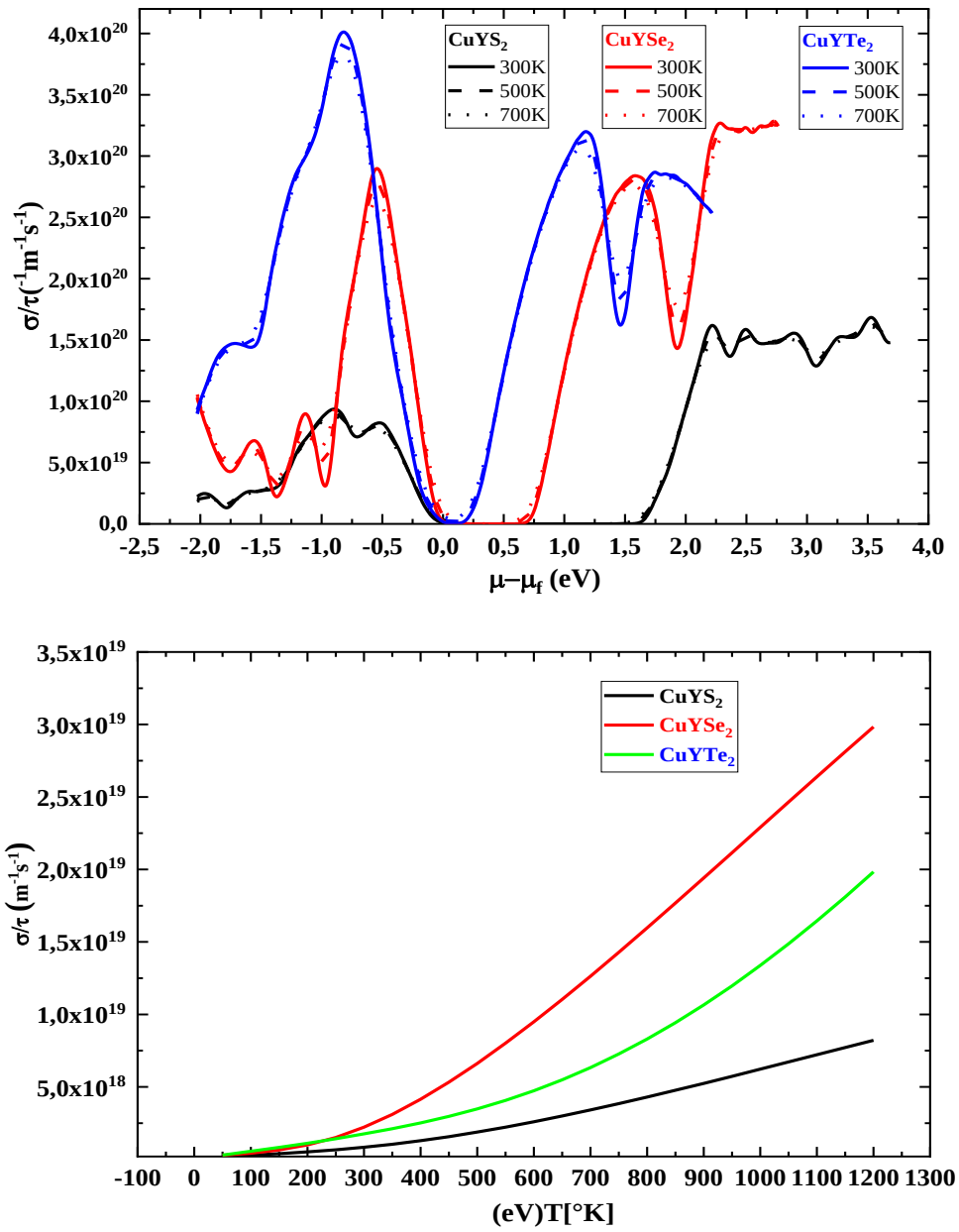

Figure. III.15. Variation of electrical conductivity (σ/τ) for $CuYZ_2$ (Z= S, Se and Te) as function of: (a) the relative chemical potential for different temperature values (300, 500 and 700K). (b) Temperature at Fermi level.

The electrical conductivity, which is a measure of free charge-carrier flow of the material [35]. The electrical conductivity directly depends upon the carrier concentration (n) and mobility (μ) through the relation (σ = neμ) [33]. According to the results obtained about the changes of electrical conductivity in terms of the relative chemical potential at different temperatures (300, 500, 700K) shown in the figure III.15-a. we note that the $CuYTe_2$ compound has higher electrical conductivity than the rest of the compounds, where its maximum value was at the relative chemical potential in

the range -1, -0.5 eV, also it can also be noted that the electrical conductivity has the highest value at the temperature of 300k and decreased slightly with increasing temperature for the all studied compounds whereas the electrical conductivity of the $CuYS_2$ compound is large when the relative chemical potential is greater than 1.5eV. Figure III.15-b characterizes the electrical conductivity variation in terms of temperature for the three compounds at the Fermi level for each compound. The results indicate that electrical conductivity is non-existent at low temperatures and then goes up with increasing temperature, with the $CuYSe_2$ compound having a higher electrical conductivity coefficient than the other compounds.

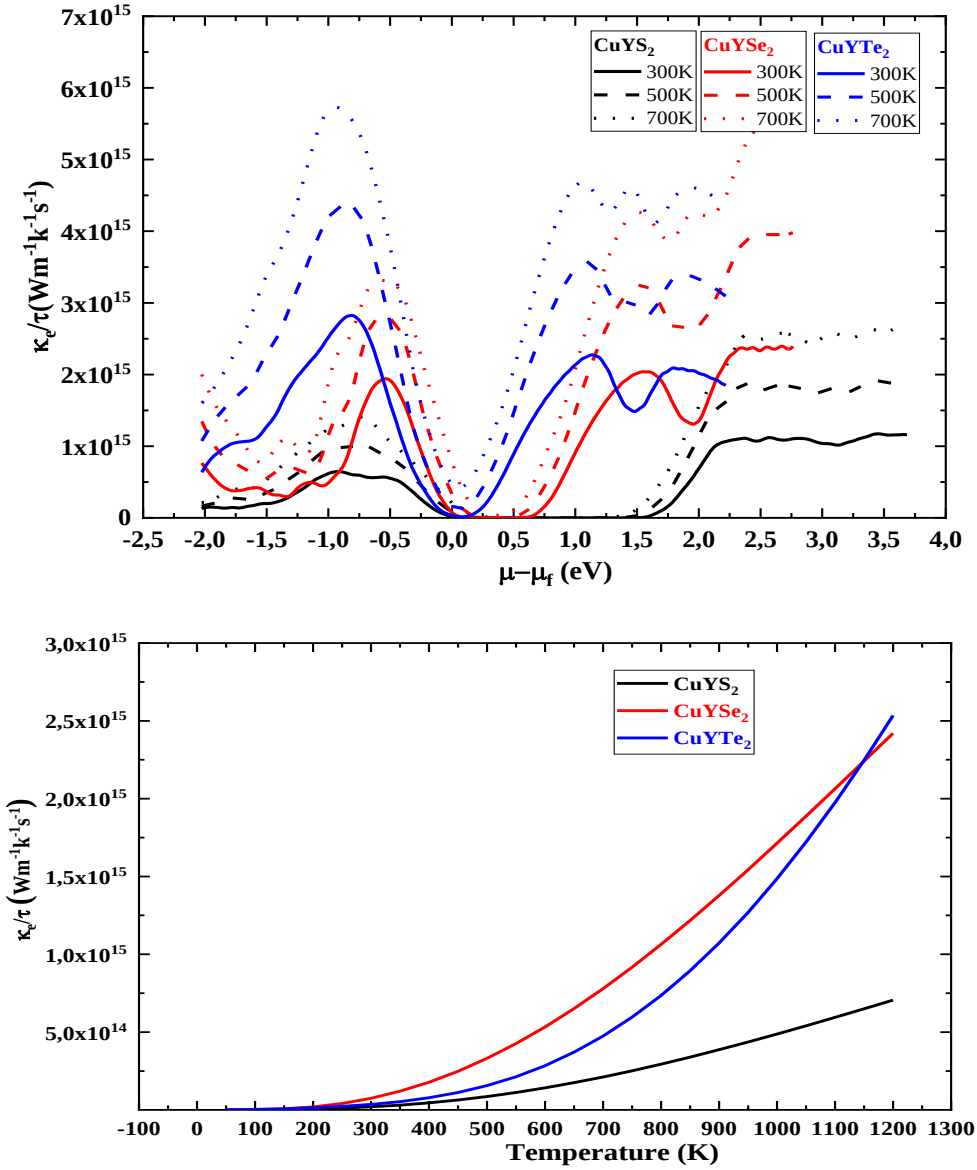

Figure. III.16. Variation of electronic thermal conductivity (κ/τ) for $CuYZ_2$ (Z= S, Se and Te) as function of: (a) the relative chemical potential for different temperature values (300, 500 and 700 K), (b) temperature at Fermi level.

It is usually known that the contributions of electrons to thermal and electrical conductivity are exactly proportional and related to each other by relation of Wiedemann–Franz law $\kappa = L\,\sigma\,T$ (L: Lorentz constant), so we can see similar shapes of curves for the electrical conductivity (σ/τ) and the electronic thermal conductivity (κ/τ) (see figure III.16 (a and b)) where the increase of the electronic thermal conductivity is related to the electron-phonon interaction due to random transport carries [50].

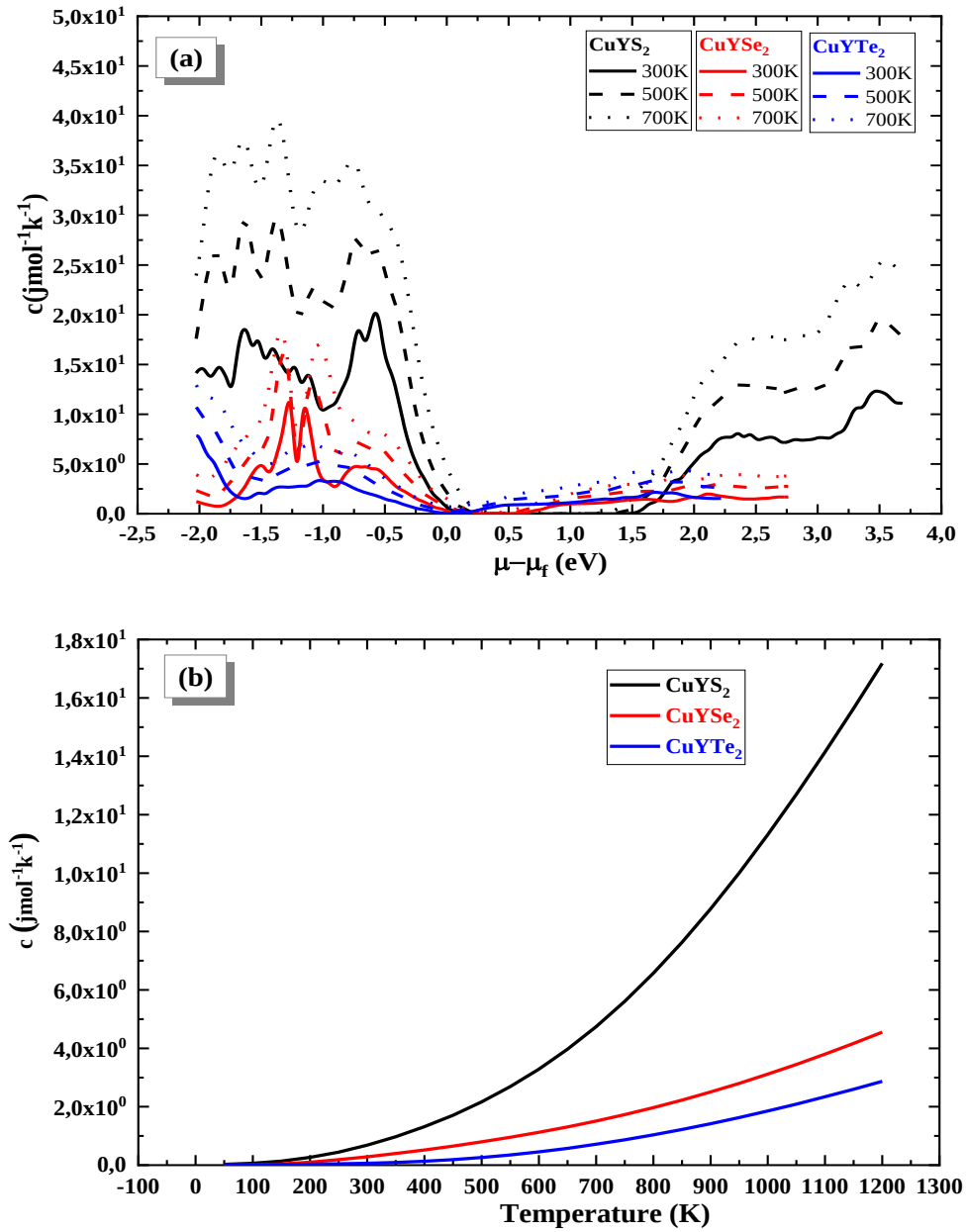

Figure. III.17. Variation of electronic heat capacity (c) for $CuYZ_2$ (Z= S, Se and Te) as function of: (a) the relative chemical potential for different temperature values (300, 500 and 700K). (b) Temperature at Fermi level.

The electronic heat capacity (c) is independent of system size and yields a degree of temperature change per unit of the substance by absorbing heat [35]. The variation of the electronic heat capacity (c) as function of the relative chemical potential at different temperatures (300, 500 and 700K) in both is shown in figure III.17-a. The results indicated that the value of electronic heat capacity (c) takes higher values in the relative chemical potential range of -2eV to 0eV for the three studied compounds, and the value of the capacity increases with rising temperature for the three compounds. The plotted curves also reveal that the $CuYS_2$ compound has a higher electronic heat capacity (c) than the other compounds unlike to $CuYTe_2$ compound that having the lowest values. Concerning the variations in electronic heat capacity (c) as a function of temperature computed at the Fermi level (see figure III.17-b), we found that the electronic heat capacity (c) has zero values at temperatures below 150 K, whereas the electronic heat capacity (c) starts to rise as temperature increases and it increases more in $CuYS_2$ than $CuYTe_2$ and $CuYSe_2$.

Figure III.18-a and b display the variation of ZT factor as a function of chemical potential at different temperatures and as function of temperature at Fermi level for each compound. This parameter is used to express the qualification of materials to transfer heat into useful electric energy.

As previously mentioned, the efficiency of materials in converting heat into electricity varies from one material to another, as can be predicted theoretically by estimating the ratio of merit, this letter is related to the many other thermoelectric properties of the material such as the contribution of electrons to thermal conductivity ,electrical conductivity in addition to Seebeck coefficient. To obtain a high merit ZT ratio, the material must have high Seebeck factor, high electricity fans and low thermal conductivity, which are significantly contributing to the transfer the heat energy to electricity instead of storing or transported as a heat. According to Figure 18-a shown to the ZT variation in term of the chemical potential at different temperatures, we note that both $CuYS_2$ and $CuYSe_2$ compounds have high ZT factor, unlike to $CuYTe_2$ compound. For the variations of ZT coefficient in terms of temperature at the Fermi level (see Figure III.18-b) we note that the value of the coefficient for the $CuYTe_2$ compound reaches a maximum at a temperature of 300 K and then decreases with increasing temperature, in contrast to $CuYS_2$ and $CuYSe_2$ compounds, where the value of the coefficient remains high and nearly constant at temperatures greater than 300 K.

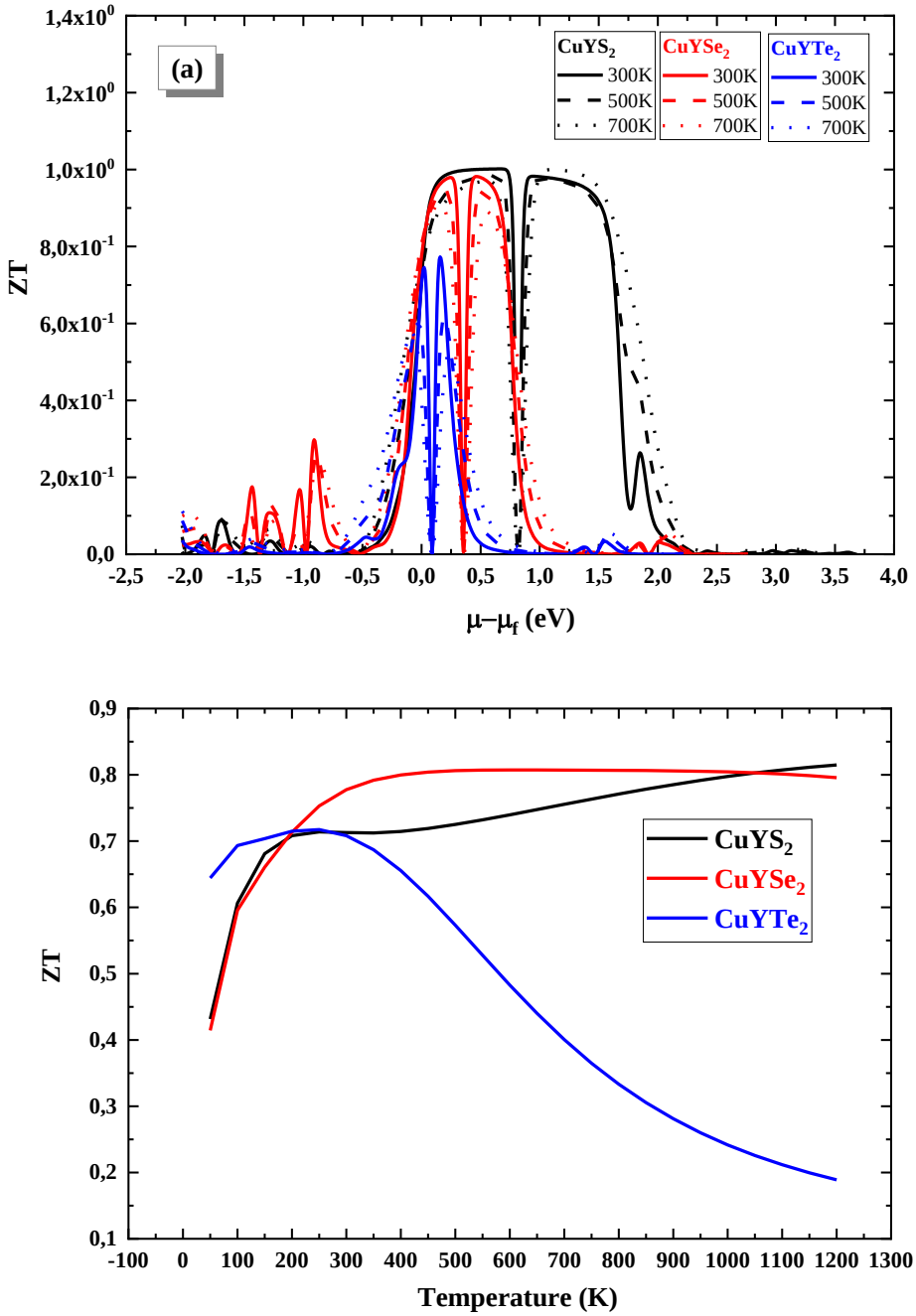

Figure. III.18. Variation of (a) the merit figure (ZT) for $CuYZ_2$ (Z= S, Se and Te) as function of: (a) the relative chemical potential for different temperature values (300, 500 and 700K). (b) Temperature at Fermi level.

8. PHOTOVALTAIC APPLICATION

Before manufacturing a solar cell, it is useful to know beforehand the order of magnitude of the electrical and optical parameters of the different layers constituting it, for which the best performance can be obtained, that is to say, a maximum conversion of energy. Simulation has been widely used in the photovoltaic field to determine the most important parameters for the operation of solar cells, to minimize losses and to optimize the physical and geometric parameters of the cell in order to obtain maximum yield. The major difficulty lies in the large number of parameters that influence performance.

The main goal in this section is to study and simulate a chalcostibites-based thin-film solar cell (ZnO/CdS/CuSb(S,Se)$_2$) by using the simulation software (wxAMPS-1D). The simulated PV structure being a multilayer system, this is why it is then essential to make an investigation of each layer and to analyze the effect of variation of the optical and electrical parameters on the cell, in order to make a comparison with the results of the simulations on chalcogenide based materials thin film solar cells. Today, there are many different types of absorbers. The reason why the best material has not been found yet is that device based on the material is expected to be not only highly efficient but also environmentally friendly and of low cost. It requires not only that the growth, manufacturing process, and recycling cost of the solar device shall be cheaper, but also that the device shall have a longer operating lifetime. Moreover, the raw materials shall be abundant and non-toxic. In this section, two main absorber materials are discussed $CuSbS_2$ and $CuSbSe_2$.

8.1 Potential copper-based chalcogenides

CIGS is already a commercialized absorber material and CZTSSe is under development [36]. However, finding alternative absorber materials is an ongoing research. $Cu_2Sn_{1-x}GexS_3$ (CTGS) and $Cu_2Sn_{1-x}Si_xS_3$ (CTSS) are potential solar cell materials [37]. Despite a few studies of Cu_2SnS_3, Cu_2GeS_3, and Cu_2SiS_3 [38–41], only few groups reported the investigations of the corresponding alloys [41,42]. The conversion efficiencies of 4.63% and 4.29%, using Cu_2SnS_3, were achieved by Nakashima et al. [43] and Kanai et al., [44], respectively. Cell efficiency of 6.0% was obtained for $Cu_2Sn_{0.83}Ge_{0.17}S_3$ by Umehara et al. [42]. Another type of potential candidate materials are Cu(Sb/Bi)(S/Se)$_2$ due to higher absorption coefficients. Solar cells based on $CuSbS_2$ and Septina et al.,[45] and Welch et al. have fabricated CuSbSe2 with conversion efficiency of ~3% [46].

8.2 Copper antimony and bismuth chalcogenides

The compounds in this study are indirect band gap semiconductors with predicted band gap energies ranging between 1.0 and 1.6 eV. The difference in band gap energy between direct and indirect band gaps is only 0.2–0.3 eV [47]. $Cu(Sb/Bi)(S/Se)_2$ has a greater absorption coefficient than CIGS and CZTS, allowing solar cells made using these absorber materials to be thinner and hence less expensive. These findings are in line with those of other researchers [48–51].

An overview of the fundamental properties of $CuBiS_2$ and $CuSbSe_2$ is presented in Table III.5.

Table.III.5. Fundamental properties of $CuBiS_2$ and $CuSbSe_2$.

Properties	***Orthorombic $CuBiS_2$***	***Orthorombic $CuSbSe_2$***
Space group	D_{2h}^{16} *Pnma, N°.62* [52]	D_{2h}^{16} *Pnma, N°.62* [58]
Lattice constant (A°)	a= 6.16 (6.14), b= 3.88 (3.92) and c= 14.20 (14.52) [53]	a= 6.31 (6.40), b= 3.97 (3.95) and c= 14.65 (15.33) [59]
Wycoff position	Cu: 4c, Bi: 4c S(1): 4c, S(2): 4c [54]	Cu: 4c, Sb: 4c Se(1): 4c, Se(2): 4c [54]
Band group energy (eV)	E_g=1.30, 1.65 [55]	E_g=1.21, 1.05 [60]
Effective mass at r (m_0)	No data	Holes (heavy):0.9 [61]
Main intrinsic defect	No data	*n*-type: Cu_i [62] *p*-type: V_{Cu} [62]
Dielectric constant ε_0	No data	13 [63]
Melting temperature (K)	793 [56]	753 [59]
Thermal conductivity (W/cm.K)	0.0005 [57]	0.002 [64]

Only a few investigations on solar cells based on $Cu(Sb/Bi)(S/Se)_2$ have been published to date [65]. Despite the fact that the compounds are indirect gap materials, they are unique PV absorber materials that are particularly attractive for ultra-thin film solar cells due to their higher absorption coefficients. Solar devices are currently only made of $CuSbSe_2$ and $CuSbS_2$, and they are quite simple to manufacture [65]. To boost efficiency, however, device engineering is required. By alloying the anion with Te ($CuSb(Se_{1-x}Te_x)_2$), the band gap energy can be optimized. Other research indicate that $CuSb(Se_{1-x}Te_x)_2$ may have slightly higher absorption coefficients than $Cu(Sb/Bi)(S/Se)_2$ [65].

8.3 Device structure

The classical thin film solar cell is a heterojunction device, meaning it comprises six layers with diverse functional characteristics [66–68]. Figure III.19 depicts a schematic of the studied structure. A comparable device construction, but a different absorber layer material, is used for solar cells based on other Cu-based materials such as CZTSSe, CTGS, $CuSbS_2$, and $CuSbSe_2$, because it is easier to apply information from CIGS cells to the relatively new solar cells.

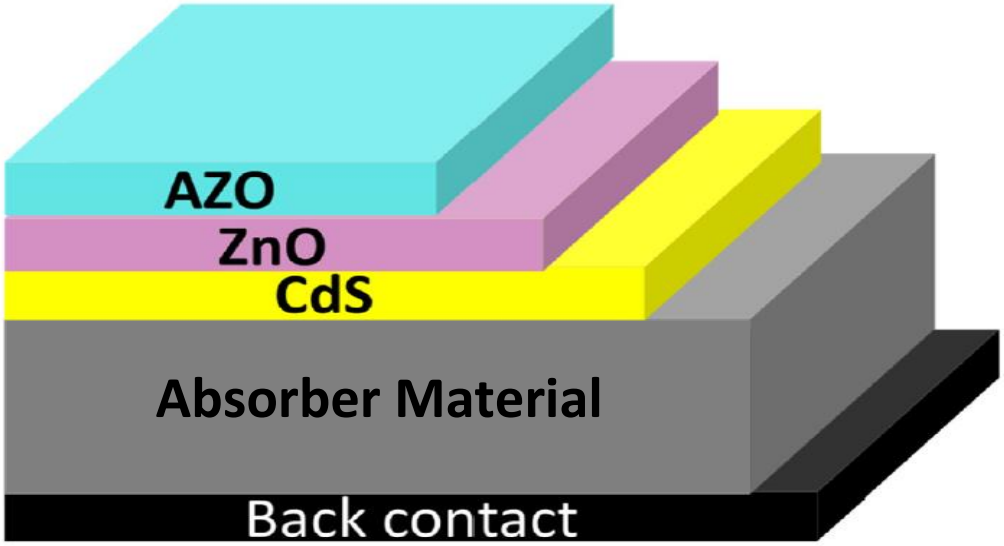

Figure III.19. Schematic structure of ZnO:Al/ZnO/CdS/Absorber material/Mo solar cell.

The substrate is on the bottom, and it comes in three varieties: soda-lime glass (SLG), metal, and polyimide. Soda-lime glass containing sodium (Na) with a thickness of 1 to 3 mm is the most typical substrate. Na can improve solar cells' efficiency and reliability, as well as process tolerance [69]. Because of its low resistivity and stability, molybdenum (Mo) with a thickness of 500nm is used as a back contact. During CIGS development, an intermediate layer $MoSe_2$ serves as an ohmic contact. The p-type absorber layer (CIGS), which has intrinsic flaws and has a thickness of 1000-2000 nm [70], is the most significant portion of the device.

The upper layer on the CIGS is a thin n-type buffer layer CdS with a thickness of ≈50 nm [71]. The front contact is made up of intrinsic zinc oxide (i-ZnO), n-type ZnO layers, and transparent conducting oxides (TCO) [72]. When depositing the ZnO:Al window layer, the i-ZnO is employed to avoid sputtering damage to the absorber materials and CdS, as well as current leakage due to inhomogeneities [73]. Aluminum (Al) is doped into n-type ZnO to increase conductivity [74,75]. In order to improve performance, the top of the cell is usually coated with an anti-reflective coating [76]. The ZnO/CdS/CIGS/Mo structure has been developed to improve the performance of solar cells [77].

8.4 Optimization of device structure

The simulations within wxAMPS-1D of the ZnO/Cds/CuSb(S/Se)$_2$ (Figure III.6) solar cells take into account previous experimental and theoretical works [78] on absorber material, CdS and ZnO devices.

Table III.6. Set of parameters of absorber material solar cell used in the simulations.

Code		ZnO[78]	CdS[78]	**$CuSbS_2$**[78]	**$CuSbSe_2$**[78]
$\boldsymbol{Thickness, [\mu m]}$		**0.08**	**0.05**	**2.5**	**2.5**
$\boldsymbol{\varepsilon}$	Relative dielectric constant.	**9**	**9**	**12**	**15**
$\boldsymbol{E_g(eV)}$	The width of the forbidden band.	**2.4**	**3.4**	**1.45**	**1.08**
$\boldsymbol{\chi_e(eV)}$	Electron affinity.	**4.5**	**4.1**	**4.05**	**4.11**
$\boldsymbol{N_C(cm^{-3})}$	Effective density of state of electrons in the conduction band.	**2.2×10^{18}**	**1.8×10^{19}**	**1.23×10^{19}**	**9.9×10^{19}**
$\boldsymbol{N_V(cm^{-3})}$	Effective state density of holes in the valence band.	**1.8×10^{19}**	**2.4×10^{18}**	**1.78×10^{20}**	**9.9×10^{19}**
$\boldsymbol{\mu_n(\frac{cm^2}{V.s})}$	Concentration of acceptors.	**100**	**100**	**4**	**10**
$\boldsymbol{\mu_p(\frac{cm^2}{V.s})}$	Concentration of donors.	**25**	**25**	**4**	**10**
$\boldsymbol{N_d(cm^{-3})}$		**10^{18}**	**10^{18}**	**0**	**0**
$\boldsymbol{N_a(cm^{-3})}$		**0**	**0**	**$1x10^{20}$**	**$1x10^{20}$**

8.5 Results of simulation

In our work, we have used the simulation tool (wxAMPS-1D) to study our structures (ZnO/CdS/CuSb(S/Se)$_2$) (figure III.19) based on the physical parameters obtained from table (III.6). To obtain the best simulation results, we have optimized the impact of materials properties such as thickness, carrier concentration of absorber and buffer layer, charge carrier mobility and lifetime, interface recombination speed, the band offset at the interface of buffer, and absorber layers to understand the better insights for the device performance.

Using the optimal thickness values of the structure (ZnO/CdS/CuSb(S/Se)$_2$) and the effect of cell performance of CuSb(S/Se)$_2$ doping concentration within the range (10^{15}-10^{20} cm^{-3}) is analyzed After starting the simulation and choosing the optimal doping concentration for this cells (10^{20} cm^{-3}) obtained from the simulation the PV parameters obtained are shown in table III.7.

The table III.7 represent the parameters of the CIGS, CZTS, and CdTe photovoltaic cells compared with the results obtained.

Table.III.7. The obtained electrical parameters of the optimized thin-film solar cells.

	Thickness (um)				PV Parameters			
	ZnO	**CdS**	**$CuSbS_2$**	**$CuSbSe_2$**	**η (%)**	**FF(%)**	**Jsc(mA/cm^2)**	**V_{oc}[V]**
ZnO/CdS/$CuSbS_2$	0.01	0.01	1	-	18.84	88.87	20.87	1.01
ZnO/CdS/$CuSbSe_2$	0.01	0.01	-	0.5	14.19	84.85	25.29	0.66
ZnO/CdS/CIGS					23.40[79]			
ZnO/CdS/CZTSSe					13.00[79]			

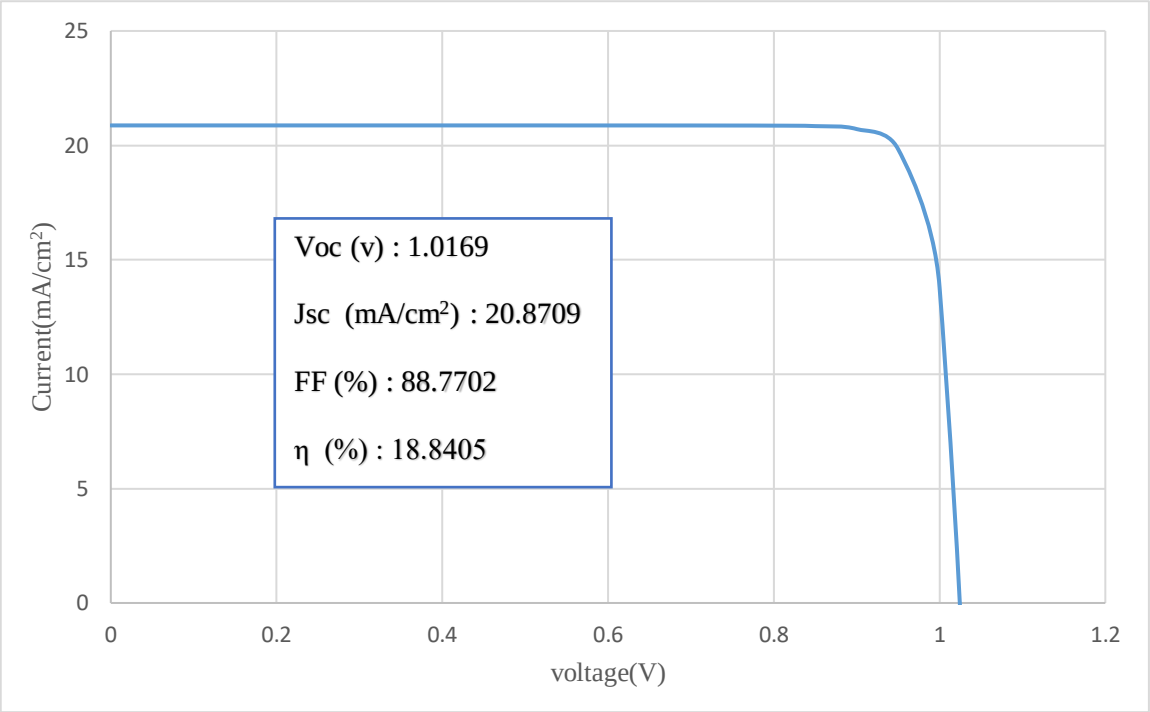

Figure.III.20. The current-voltage (J-V) characteristic of the $CuSbS_2$ solar cell.

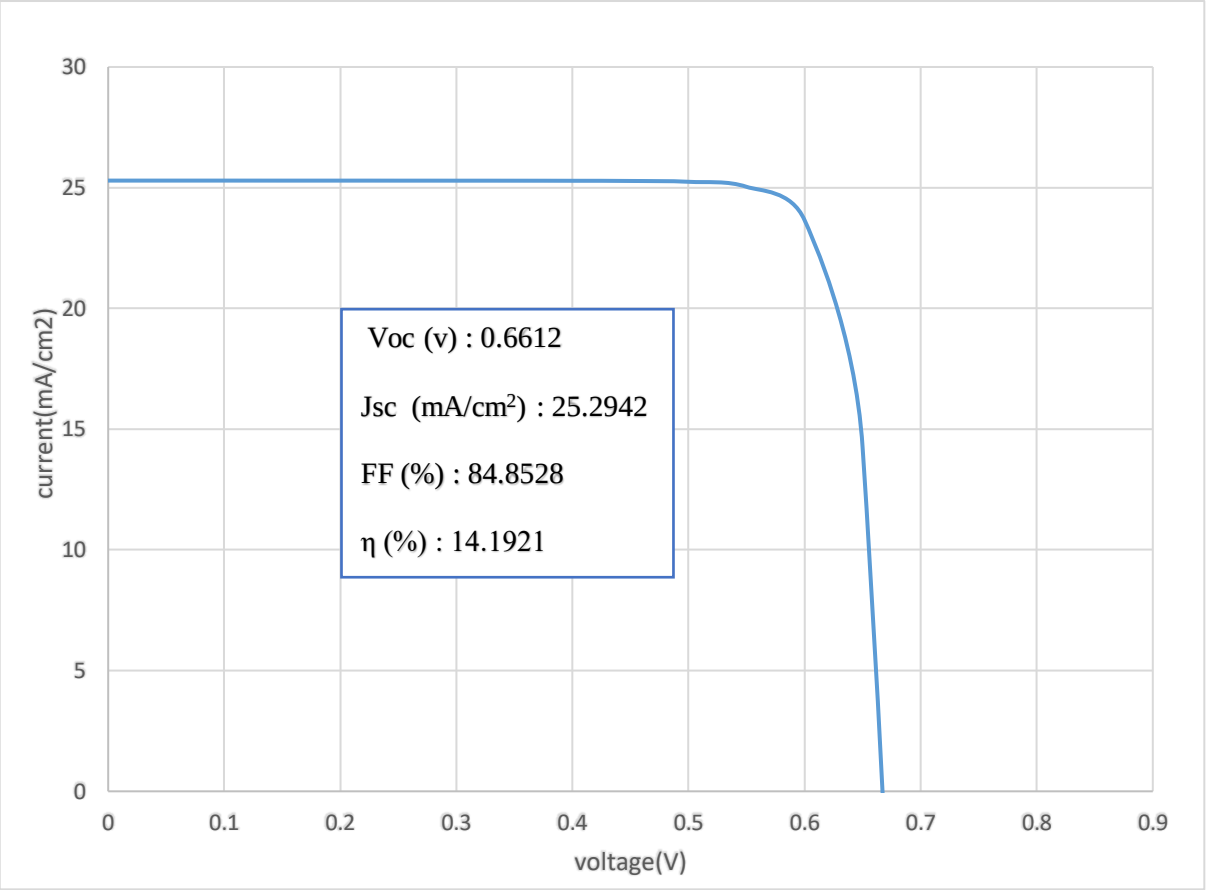

Figure.III.21. The current-voltage (J-V) characteristic of the $CuSbSe_2$ solar cell.

In this section, we have been performed a simulation for $CuSbSe_2$ and $CuSbS_2$ based thin-film solar cells using wxAMPS-1D package. The efficiency of the solar cells has been optimized by varying the thickness and doping concentrations of TCO layers, buffer layers, and absorber layers. Moreover, the obtained maximum efficiencies are approximately 14.19% and approximately 18.84%, for $CuSbSe_2$ and $CuSbS_2$ based solar cell, respectively.

9. Conclusion

Our study presents new results concerning the electronic, optical, thermodynamic and thermoelectric properties of the ternary chalcogenide compounds $CuYS_2$, $CuYSe_2$ and $CuYTe_2$. These results are obtained using the FP-LAPW method with the TB-mBJ approximation and also with the help of other approximations. The three compounds have the same electronic behavior, as they are semiconductors with different energy gaps. These compounds are considered to have good cohesive energies, especially $CuYS_2$ compound. They have good optical properties, in particular, $CuYS_2$ compound, which has a high absorption coefficient compared to the rest of the compounds. The $CuYS_2$ has a less ability to absorb energy at ambient temperatures compared to the rest of the compounds as well as other thermal properties under the influence of pressure and heat, which they are promising, compounds to use them in electro-optical fields and its applications. The $CuYS_2$ is a good candidate thermoelectric device due to their high Seebeck coefficient reaching to 3.0 mV/K and low thermal conductivity value at ambient temperature. Which makes them candidate materials to use in photovoltaic applications.

Finally in this chapter, we optimize the physical and electrical parameters such as the thicknesses for each layer of the cell in order to see their influences on the electrical characteristic of the $ZnO/CdS/CuSb(S/Se)_2$ structures. Thus, it is hoped that this study will help the novices, scientists, researchers and manufacturers to understand the behavior of $CuSbSe_2$ and $CuSbS_2$ thin film solar cells and to fabricate non-toxic, earth-abundant less complex and high-efficiency thin film solar cells in the near future.

10. References

[1] P. Blaha, K. Schwarz, G.K. Madsen, D. Kvasnicka, J. Luitz, wien2k, Augment. Plane Wave Local Orbitals Program Calc. Cryst. Prop. (2001).

[2] W. Kohn, L.J. Sham, Self-consistent equations including exchange and correlation effects, Phys. Rev. 140 (1965) A1133.

[3] J.P. Perdew, K. Burke, M. Ernzerhof, Generalized gradient approximation made simple, Phys. Rev. Lett. 77 (1996) 3865–3868.

[4] A.D. Becke, E.R. Johnson, A simple effective potential for exchange, American Institute of Physics, 2006.

[5] V.L. A. Otero-de-la-Roza, D. Abbasi-Pérez, Gibbs2: A new version of the quasiharmonic model code. II. Models for solid-state thermodynamics, features and implementation, Comput. Phys. Commun. 182(10) (2011) 2232–2248.

[6] V.L. A. Otero-de-la-Roza, Gibbs2: A new version of the quasi-harmonic model code. I. Robust treatment of the static data, Comput. Phys. Commun. 182(8) (2011) 1708–1720.

[7] G.K. Madsen, D.J. Singh, BoltzTraP. A code for calculating band-structure dependent quantities, Comput. Phys. Commun. 175 (2006) 67–71.

[8] P. Lauxmann, T. Schleid, $CuYS_2$: Ein ternäres Kupfer (I)-Yttrium (III)-Sulfid mit Ketten $^1{}_\infty\{[Cu(S1)_{3/3}(S2)_{1/1}]^{3-}\}$ cis-kantenverknüpfter $[CuS_4]^{7-}$-Tetraeder, Z. Für Anorg. Allg. Chem. 626 (2000) 1608–1612.

[9] P. Villars, H. Okamoto, Springer-Verlag Berlin Heidelberg & Material Phases Data System (MPDS), Switz. Natl. Inst. Mater. Sci. NIMS Jpn. (n.d.).

[10] U. Aydemir, J.-H. Pöhls, H. Zhu, G. Hautier, S. Bajaj, Z.M. Gibbs, W. Chen, G. Li, S. Ohno, D. Broberg, $YCuTe_2$: a member of a new class of thermoelectric materials with $CuTe_4$-based layered structure, J. Mater. Chem. A. 4 (2016) 2461–2472.

[11] C.G. Broyden, The convergence of a class of double-rank minimization algorithms: 1. general considerations, IMA J. Appl. Math. 6 (1970) 76–90.

[12] C.G. Broyden, The convergence of a class of double-rank minimization algorithms: 2. The new algorithm, IMA J. Appl. Math. 6 (1970) 222–231.

[13] F.D. Murnaghan, The compressibility of media under extreme pressures, Proc. Natl.Acad. Sci. U.S.A. 30 (1944) 244.

[14] M.G. Brik, First-principles calculations of the structural, electronic, optical and elastic properties of the $CuYS_2$ semiconductor, J. Phys. Condens. Matter. 25 (2013) 345802.

[15] M.D. Heinemann, F. Ruske, D. Greiner, A.R. Jeong, M. Rusu, B. Rech, R. Schlatmann, C.A. Kaufmann, Advantageous light management in Cu(In, Ga)Se_2 superstrate solar cells, Sol. Energy Mater. Sol. Cells. 150 (2016) 76–81.

[16] J. Jiang, W. Zhou, Y. Xue, H. Ning, X. Liang, W. Zhou, J. Guo, D. Huang, Intermediate band insertion by group-IIIA elements alloying in a low cost solar cell absorber $CuYSe_2$: A first-principles study, Phys. Lett. A. 383 (2019) 1972–1976.

[17] M.A. Khan, A. Kashyap, A.K. Solanki, T. Nautiyal, S. Auluck, Interband optical properties of Ni 3 Al, Phys. Rev. B. 48 (1993) 16974.

[18] Optical Properties of Materials and Their Applications, 2nd Edition | Wiley, Wiley.Com. (n.d.). (accessed February 4, 2021).

[19] C. Ambrosch-Draxl, J.O. Sofo, Linear optical properties of solids within the full-potential linearized augmented planewave method, Comput. Phys. Commun. 175 (2006) 1–14.

[20] M. Gajdoš, K. Hummer, G. Kresse, J. Furthmüller, F. Bechstedt, Linear optical properties in the projector-augmented wave methodology, Phys. Rev. B. 73 (2006) 045112.

[21] B.U. Haq, S. AlFaify, A.S. Jbara, R. Ahmed, F.K. Butt, A. Laref, A.R. Chaudhry, Z.A. Shah, Optoelectronic properties of three PbSe polymorphs, Ceram. Int. 46 (2020) 22181–22188.

[22] A.S. Jbara, Z. Othaman, H.A. Aliabad, M.A. Saeed, Electronic and Optical Properties of γ-and-Alumina by First Principle Calculations, Adv. Sci. Eng. Med. 9 (2017) 287–293.

[23] A.S. Jbara, J. Munir, B.U. Haq, M.A. Saeed, Density functional theory study of mixed halide influence on structures and optoelectronic attributes of $CsPb(I/Br)_3$, Appl. Opt. 59 (2020) 3751–3759.

[24] H. Tributsch, Solar energy-assisted electrochemical splitting of water. Some energetical, kinetical and catalytical considerations verified on MoS_2 layer crystal surfaces, Z. Für Naturforschung A. 32 (1977) 972–985.

[25] T. Kaur, B. Kaur, B.H. Bhat, S. Kumar, A.K. Srivastava, Effect of calcination temperature on microstructure, dielectric, magnetic and optical properties of $Ba_{0.7}La_{0.3}Fe_{11.7}Co_{0.3}O_{19}$ hexaferrites, Phys. B Condens. Matter. 456 (2015) 206–212.

[26] C. Ambrosch-Draxl, J.O. Sofo, Linear optical properties of solids within the fullpotential linearized augmented planewave method, Comput. Phys. Commun. 175 (2006) 1–14.

[27] M.A. Khan, A. Kashyap, A.K. Solanki, T. Nautiyal, S. Auluck, Interband optical properties of Ni_3Al, Phys. Rev. B 48 (1993) 16974.

[28] V. Srivastava, N. Kaur, X. Wang, M. Mushtaq, S.A. Dar, First-principles study on structural, electronic, magnetic, elastic, mechanical and thermodynamic properties of Mn_2PtCo Heusler alloy, Int. J. Energy Res. 45 (2021) 11305–11319.

[29] P.L. Dulong, A.-T. Petit, Recherches sur quelques points importans de la theorie de la Chaleur, 1819.

[30] V. Srivastava, N. Kaur, R. Khenata, S.A. Dar, Investigation of the electronic, magnetic, elastic, thermodynamic and thermoelectric properties of Mn_2CoCr Heusler compound: A DFT-based simulation, J. Magn. Magn. Mater. 513 (2020) 167107.

[31] I. Jum'h, H. Baaziz, Z. Charifi, A. Telfah, Electronic and Magnetic Structure and Elastic and Thermal Properties of Mn 2-Based Full Heusler Alloys, J. Supercond. Nov. Magn. 32 (2019) 3915–3926.

[32] S.S. Essaoud, A.S. Jbara, First-principles calculation of magnetic, structural, dynamic, electronic, elastic, thermodynamic and thermoelectric properties of Co_2ZrZ (Z= Al, Si) Heusler alloys, J. Magn. Magn. Mater. (2021) 167984.

[33] J. Singh, K. Kaur, S.A. Khandy, S. Dhiman, M. Goyal, S.S. Verma, Structural, electronic, mechanical, and thermoelectric properties of LiTiCoX(X= Si, Ge) compounds, Int. J. Energy Res. (2021).

[34] A. Telfah, S.S. Essaoud, H. Baaziz, Z. Charifi, A.M. Alsaad, M.J.A. Ahmad, R. Hergenr¨oder, R. Sabirianov, DFT investigation of physical properties of KCrZ (Z=S, Se, Te) half-heusler alloys. Phys. Status Solidi B n/a (n.d.).

[35] S.A. Khandy, D.C. Gupta, Structural, elastic and thermo-electronic properties of paramagnetic perovskite PbTaO3, RSC Adv. 6 (2016) 48009–48015.

[36] P. Fernandes, P. Salomé, and A. Da Cunha Journal of Physics D: Applied Physics, vol. 43,p. 215403, 2010.

[37] D. M. Berg, R. Djemour, L. Gütay, S. Siebentritt, P. J. Dale, X. Fontane, V. Izquierdo-Roca, and A. Pérez-Rodriguez Applied Physics Letters, vol. 100, p. 192103, 2012.

[38] Y.-T. Zhai, S. Chen, J.-H. Yang, H.-J. Xiang, X.-G. Gong, A. Walsh, J. Kang, and S.-H.Wei Physical Review B, vol. 84, p. 075213, 2011.

[39] A. Shigemi, T. Maeda, and T. Wada Physica Status Solidi (B), vol. 252, p. 1230, 2015.

[40] A. Aruga and Y. Okamoto Japanese Journal of Applied Physics, vol. 45, p. 4616, 2006.

[41] K. Toyonaga and H. Araki Physica Status Solidi (C), vol. 12, p. 753, 2015.

[42] M. Umehara, Y. Takeda, T. Motohiro, T. Sakai, H. Awano, and R. Maekawa Applied Physics Express, vol. 6, p. 045501, 2013.

[43] M. Nakashima, J. Fujimoto, T. Yamaguchi, and M. Izaki Applied Physics Express, vol. 8,p. 042303, 2015.

[44] A. Kanai, K. Toyonaga, K. Chino, H. Katagiri, and H. Araki Japanese Journal of Applied Physics, vol. 54, p. 08KC06, 2015.

[45] W. Septina, S. Ikeda, Y. Iga, T. Harada, and M. Matsumura Thin Solid Films, vol. 550,p. 700, 2014.

[46] A. W. Welch, L. L. Baranowski, P. Zawadzki, S. Lany, C. A. Wolden, and A. Zakutayev Applied Physics Express, vol. 8, p. 082301, 2015.

[47] Y. Rodrıguez-Lazcano, M. Nair, and P. Nair Journal of Crystal Growth, vol. 223, p. 399,2001.

[48] M. Kumar and C. Persson Applied Physics Letters, vol. 102, p. 062109, 2013.

[49] A. B. Kehoe, D. J. Temple, G. W. Watson, and D. O. Scanlon Physical Chemistry Chemical Physics, vol. 15, p. 15477, 2013.

[50] V. Estrella, M. Nair, and P. Nair Semiconductor Science and Technology, vol. 18, p. 190,2003.

[51] J. T. Dufton, A. Walsh, P. M. Panchmatia, L. M. Peter, D. Colombara, and M. S. Islam Physical Chemistry Chemical Physics, vol. 14, p. 7229, 2012.

[52] D. J. Temple, A. B. Kehoe, J. P. Allen, G. W. Watson, and D. O. Scanlon The Journal of Physical Chemistry C, vol. 116, p. 7334, 2012.

[53] J. C. Portheine and W. Nowacki Zeitschrift für Kristallographie-Crystalline Materials, vol. 141, p. 387, 1975.

[54] M. Kumar and C. Persson Energy Procedia, vol. 44, p. 176, 2014.

[55] S. Pawar, A. Pawar, and P. Bhosale Bulletin of Materials Science, vol. 8, p. 423, 1986.

[56] M. Razmara, C. Henderson, R. Pattrick, A. Bell, and J. Charnock Mineralogical Magazine,vol. 61, p. 79, 1997.

[57] D. Spitzer Journal of Physics and Chemistry of Solids, vol. 31, p. 19, 1970.

[58] O. Madelung, Semiconductors: Data Handbook. Springer, 2004.

[59] J. Zhou, G.-Q. Bian, Q.-Y. Zhu, Y. Zhang, C.-Y. Li, and J. Dai Journal of Solid State Chemistry, vol. 182, p. 259, 2009.

[60] D. Zhang, J. Yang, Q. Jiang, L. Fu, Y. Xiao, Y. Luo, and Z. Zhou Journal of Materials Chemistry A, vol. 4, p. 4188, 2016.

[61] D.-J. Xue, B. Yang, Z.-K. Yuan, G. Wang, X. Liu, Y. Zhou, L. Hu, D. Pan, S. Chen, and J. Tang Advanced Energy Materials, vol. 5, 2015.

[62] A. W. Welch, L. L. Baranowski, P. Zawadzki, S. Lany, C. A. Wolden, and A. Zakutayev Applied Physics Express, vol. 8, p. 082301, 2015.

[63] D. Li and X. Qin Journal of Applied Physics, vol. 100, p. 3713, 2006.

[64] A. W. Welch, L. L. Baranowski, P. Zawadzki, S. Lany, C. A. Wolden, and A. Zakutayev Applied Physics Express, vol. 8, p. 082301, 2015.

[65] O. Lundberg, M. Edo_, and L. Stolt Thin Solid Films, vol. 480, p. 520, 2005.

[66] O. Lundberg, J. Lu, A. Rockett, M. Edo_, and L. Stolt Journal of Physics and Chemistry of Solids, vol. 64, p. 1499, 2003.

[67] K. Ramanathan, M. A. Contreras, C. L. Perkins, S. Asher, F. S. Hasoon, J. Keane, D. Young, M. Romero, W. Metzger, R. Noufi, J. Ward, and A. Duda Progress in Photovoltaics:Research and Applications, vol. 11, p. 225, 2003.

[68] R. Scheer, R. Klenk, J. Klaer, and I. Luck Solar Energy, vol. 77, p. 777, 2004.

[69] D. Rudmann, D. Bremaud, H. Zogg, and A. Tiwari Journal of Applied Physics, vol. 97, p. 084903, 2005.

[70] T. Feurer, P. Reinhard, E. Avancini, B. Bissig, J. Löckinger, P. Fuchs, R. Carron, T. P. Weiss, J. Perrenoud, S. Stutterheim, S. Buecheler, and A. N. Tiwari Progress in Photovoltaics: Research and Applications, 2016.

[71] K. Matsubara, P. Fons, K. Iwata, A. Yamada, K. Sakurai, H. Tampo, and S. Niki Thin Solid Films, vol. 431, p. 369, 2003.

[72] U. Rau, P. Grabitz, and J. Werner Applied Physics Letters, vol. 85, p. 6010, 2004.

[73] K. H. Kim, K. C. Park, and D. Y. Ma Journal of Applied Physics, vol. 81, p. 7764, 1997.

[74] T. Minami, H. Nanto, and S. Takata Japanese Journal of Applied Physics, vol. 23, p. L280,1984.

[75] S. Niki, M. Contreras, I. Repins, M. Powalla, K. Kushiya, S. Ishizuka, and K. Matsubara Progress in Photovoltaics: Research and Applications, vol. 18, p. 453, 2010.

[76] J. Kessler, M. Bodegard, J. Hedström, and L. Stolt Solar Energy Materials and Solar Cells, vol. 67, p. 67, 2001.

[77] Liu Y, Sun Y, Rockett A. A new simulation software of solar cells–*wx*AMPS. Sol Energ Mater Sol C. 2012;98: 124.

[78] Gupta GK, Dixit A.Simulation studies on photovoltaic response of ultrathin $CuSb(S/Se)_2$ ternary compound semiconductors absorber-based single junctionsolar cells. Int J Energy Res. 2020;1–13.

[79] National Renewable Energy Laboratory, Best Research-Cell Efficiencies. United States of America: National Renewable Energy Laboratory, 2021.

General conclusion

Chalcogenide have a bright future and they are consistently finding applications in various sectors. We are putting here few of the challenges which are dealing in current research for a future prospectus. From the synthesis and processing point of view, these materials should have cheap manufacturing process. These materials enlarge an excellent challenge for their function and implementation in sensor devices due to their good sensor-specific advantages.

The first principle calculation based on DFT theory was used to estimate structural, electrical, and optical properties of copper-based chalcogenides: $CuYS_2$, $CuYSe_2$, and $CuYTe_2$ in orthorhombic and hexagonal structural phases. The results revealed that the three compounds have the same electrical behavior, despite the fact that they are semiconductors with different energy gaps. Furthermore, these compounds, particularly $CuYS_2$, are thought to have high cohesive energies. The optical properties of the three compounds show that they have good optical properties, especially $CuYS_2$, which has a high absorption coefficient compared to the other compounds. As a result, they are good candidates for photovoltaic applications. In terms of the temperature and pressure effects on the thermodynamic properties of the three compounds, we discovered that the $CuYZ_2$ with the sulfur atom (S) has a lower ability to absorb energy at ambient temperatures compared to the other compounds, as well as other thermal properties under the influence of pressure and heat. As a result of our research, $CuYZ_2$ (Z= S, Se, and Te) appear to be promising compounds for use in electro-optical fields and applications. The ability of both $CuYS_2$ and $CuYSe_2$ to be used as thermoelectric materials due to their specific thermodynamic and electronic features can be validated by estimating thermoelectric properties based on the semi-classical Boltzmann theory, such as thermal conductivity, Seebeck coefficient, and electronic conductivity. $CuYS_2$ is a promising candidate thermoelectric device, according to the thermoelectric findings, because of its high Seebeck coefficient of 3.0 mV/K and low thermal conductivity value at ambient temperature.

Under AM 1.5G light, the performance of two separate solar cell installations was optimized By using the wxAMPS-1D simulation program and compared in terms of doping, thickness of dielectric layers, and absorption. The $CuYS_2$ buffer layer had the best performance characteristics (η = 18.84%, FF=84.85%, Jsc=25.29 mA/cm^2 and Voc = 0.66 V).

As a result, in CIGS thin-film solar cells, alloy could be a potential better alternative to the traditional CdS dielectric layer. We observed that the band alignment at $CuSb(S/Se)_2$ and CdS interface is less critical as compared with other absorbers. Overall, the findings are critical for future technical advancements in experimental work.

The present work clearly demonstrates the current state of semiconductors (Ch = S, Se, Te) in materials research, indicating that this is a key area of ongoing and future study. The work provided a brief overview of materials, sustainability issues, and some of the new development approaches facing the field of thin-film photovoltaic technologies for the challenging and exciting years ahead.

Finally, by evaluating, classifying, and discussing potential possibilities in chalcogenides, this study aims to encourage further research on this growing class of semiconductors, thus enabling future developments in optoelectronic devices and some new development approaches that challenge the field of thin-film photovoltaic technologies in the coming years.

Résumé

En raison de leurs propriétés physiques utiles, les matériaux chalcogenides à base de cuivre sont depuis peu prometteurs pour de nombreux domaines technologiques émergents. Dans le domaine du photovoltaïque, la découverte et la conception de matériaux appropriés pour les cellules solaires constituent un défi technique majeur. Les propriétés structurelles, électriques, optiques et thermoélectriques de $CuYSe_2$ et $CuYTe_2$ dans la phase hexagonale, ainsi que de $CuYS_2$ dans la phase orthorhombique, ont été étudiées à l'aide d'une technique numérique Full Potential-Linearized Augmented Plane Wave (FP-LAPW) basée sur la théorie de la fonction de densité (DFT). Pour calculer les propriétés structurelles, l'approximation de la densité locale (LDA) et l'approximation du gradient généralisé (PBE-GGA) ont été utilisées comme potentiels d'échange-corrélation. D'autre part, la méthode de Becke-Johnson modifiée (mBJ) a été utilisée pour calculer les propriétés optoélectroniques avec un degré de précision plus élevé. Nos calculs ont révélé que ces trois composés ont des bandes interdites indirectes dans la gamme de 0,6 eV à 2,1eV. De plus, de nombreuses qualités thermoélectriques des composés étudiés ont été estimées en fonction de l'énergie chimique à différentes températures en utilisant la théorie du transport de Boltzmann semi local. Les résultats montrent un coefficient Seebeck plus élevé pour $CuYS_2$ par rapport à $CuYZ_2$ (Z = Se et Te) jusqu'à 2,7 mV/K pour $CuYS_2$ à 300 K, avec des valeurs acceptables de conductivité thermique et électronique. Le modèle quasi-harmonique est utilisé pour examiner les propriétés thermodynamiques telles que la capacité thermique à pression et volume constants, l'entropie, la température de Debye et le coefficient d'expansion thermique sous l'influence de la pression et de la température. Suite à cette étude, $CuYS_2$, $CuYSe_2$ et $CuYTe_2$ sont des matériaux prometteurs pour les dispositifs optoélectroniques, notamment comme matériaux photovoltaïques dans les cellules solaires. Nous avons réalisé la simulation numérique. Nous optimisons les paramètres physiques et électriques tels que les épaisseurs pour chaque couche de la cellule afin de voir leurs influences sur la caractéristique électrique des structures $ZnO/CdS/CuSb(S/Se)_2$. L'efficacité des cellules solaires a été observée en faisant varier l'épaisseur et les concentrations de dopage des couches de TCO, des couches tampon et des couches d'absorption. De plus, les rendements maximaux obtenus sont d'environ 18,84% et d'environ 14,19%, pour les cellules solaires à base de $CuSbS_2$ et de $CuSbSe_2$, respectivement.

Mots clés : TB-mBJ, coefficient de Seebeck, coefficients de conductivité électrique et thermique, fonction diélectrique, coefficient d'absorption, réflectivité, capacité thermique, coefficient de dilatation thermique, wx-AMPS-1D.

الملخص

نظرًا لخصائصها الفيزيائية المفيدة، فقد أظهرت مواد الكالكوجينيد النحاسية مؤخرًا أنها واعدة للعديد من مجالات التكنولوجيا الناشئة. في مجال الخلايا الكهروضوئية، يعد اكتشاف وتصميم المواد المناسبة للخلايا الشمسية تحديًا تقنيًا كبيرًا. تم فحص الخواص التركيبية والكهربائية والبصرية والكهروحرارية لـ $CuYSe_2$ و $CuYTe_2$ في الطور السداسي، وكذلك $CuYS_2$ في الطور التقويمي المقوم، باستخدام التقنية العددية للموجة الخطية المعززة (FP-LAPW) ذات الإمكانات الكاملة (DFT) .

لحساب الخصائص الهيكلية، تم استخدام تقريب الكثافة المحلية (LDA) وتقريب التدرج المعمم (PBE-GGA) كإمكانية ارتباط التبادل. من ناحية أخرى، تم استخدام طريقة Becke-Johnson المعدلة (mBJ) لحساب الخصائص الإلكترونية الضوئية بدرجة أعلى من الدقة. كشفت حساباتنا أن هؤلاء الثلاثة تحتوي المركبات على فجوات نطاق غير مباشرة في النطاق من 0.6 فولت إلى 2.1 فولت. بالإضافة إلى ذلك، تم تقدير العديد من الصفات الكهروحرارية للمركبات المدروسة كدالة للطاقة الكيميائية عند درجات حرارة مختلفة باستخدام نظرية النقل شبه المحلية Boltzmann .أظهرت النتائج أن معامل سيبيك أعلى لـ$CuYS_2$ مقارنة بـ ($CuY(Se_2$ and Te_2) حتى 2.7 mV/K لـ $CuYS_2$ عند 300K، مع قيم مقبولة للتوصيل الحراري والإلكتروني. يستخدم النموذج شبه التوافقي لفحص الخصائص الديناميكية الحرارية مثل السعة الحرارية عند ضغط وحجم ثابتين، الإنتروبيا، درجة حرارة ديباي، ومعامل التمدد الحراري تحت تأثير الضغط ودرجة الحرارة. بعد هذه الدراسة، تعد $CuYS_2$ و $CuYSe_2$ و $CuYTe_2$ مواد واعدة للأجهزة الكهروضوئية ، خاصة المواد الكهروضوئية في الخلايا الشمسية. أجرينا المحاكاة العددية. نقوم بتحسين المعلمات الفيزيائية والكهربائية مثل سماكة كل طبقة من الخلايا لمعرفة تأثيرها على الخصائص الكهربائية لهياكل .$ZnO/CdS/CuSb\ (S/Se)_2$ وقد لوحظت كفاءة الخلايا الشمسية من خلال تغيير سماكة وتركيزات المنشطات لطبقات TCO والطبقات العازلة وطبقات الامتصاص. علاوة على ذلك، بلغت الكفاءات القصوى التي تم الحصول عليها حوالي 18.84٪ وحوالي 14.19٪ للخلايا الشمسية المعتمدة على$CuSbS_2$ و $CuSbSe_2$ على التوالي.

الكلمات المفتاحية: TB-mBJ، معامل سيبيك، معاملات التوصيل الكهربائي والحراري، دالة العزل، معامل الامتصاص، الانعكاسية، السعة الحرارية، معامل التمدد الحراري، wx-AMPS-1D.